Liposomes as a model system for the study of surface active peptides

Master's thesis in Chemistry

Victoria Ariel Bjørnestad

Thesis submitted for the degree of
Master in Chemistry
60 credits

Department of Chemistry
Faculty of Mathematics and Natural Sciences

UNIVERSITY OF OSLO

Spring 2018

Liposomes as a model system for the study of surface active peptides

Master's thesis in Chemistry

Victoria Ariel Bjørnestad

Liposomes as a model system for the study of surface active peptides

http://www.duo.uio.no/

Printed: Reprosentralen, University of Oslo

Abstract

The increase in occurrence of multi resistant pathogens in the world calls for alternatives to the conventional antimicrobial medicine available today. Antimicrobial peptides (AMPs) are promising agents for the development of these future antibiotics, but the lack of knowledge about their mode of action makes AMP-based drug design difficult. It is known that the peptides interact with the plasma membrane of the pathogens and that this interaction is integral for their antimicrobial activity. To study these lipid-specific interactions of AMPS we aim to use lipid vesicles, liposomes, i.e. spherical phospholipid bilayers, as mimics of the bacterial and mammalian membranes. Structural changes in the bilayer of the liposomes upon addition of AMP can then be characterised using X-ray scattering techniques. Small angle X-ray/neutron scattering (SAXS/SANS) techniques provide the optimal tool for investigating these changes at a nanoscale. Liposomes alone, however, have been found to precipitate in the presence of AMPs, and therefore some method of stabilising the liposomes that still allowed the peptide to interact with the membrane was required for their microscopic mode of action to be probed by these techniques. In this thesis, two types of conjugated poly(ethylene oxide) (PEO) polymers have been tested for their potential for stabilising liposomes in the presence of AMPs. The two stabilised liposomal systems were studied in terms of their kinetic stability, structure and microscopic interactions with the AMP Indolicidin as well as the known flocculant and transfection agent poly(ethylene imine) (PEI), which was used for comparison with the peptide. One system consisted of adding free n-alkyl-poly(ethylene oxides) (C_n-PEO) to the liposomes after they had been formed. For the other system, poly(ethylene oxide)-modified phospholipids (”PEGylated” lipids) were incorporated into the liposomal bilayer during their formation. Both methods efficiently stabilise the liposomes through steric repulsions. Although addition of n-alkyl-poly(ethylene oxide) makes the system more versatile and simpler in terms of preparation, the n-alkyl-poly(ethylene oxide) was found to interact and modify the membranes to a great extent. At 37 °C the C_n-PEO likely partially dissolved the bilayers and formed mixed micelles with the lipids. In addition, it interacted with the AMP itself forming mixed ill-defined aggregates. The multitude of interactions yields results that are difficult to interpret. This suggested that the better approach was to use the PEGylated phospholipids for stabilisation. The PEGylation stabilised the liposomes against aggregation without modifying the bilayer significantly, and the attached polymer did not prevent the interaction of AMPs with the membrane either. A great part of the work was dedicated to develop analytical quantitative scattering models to describe the detailed liposomal structure as well as the intercalation of peptide into the membrane. These models were found to fully account for the experimental data. One of the more popular assertions for AMPs is that they make the lipid membrane more permeable to water and alter pH -gradients across the bilayer. The chosen model system of PEGylated liposomes was therefore also tested for the time scale of water transport across the membrane using SANS to investigate whether it would be possible to study how the AMPs might affect this transport. SANS has the benefit over previous techniques measuring water diffusion in that it can measure the structure of the bilayer simultaneously. Interestingly, a complete exchange of water occurred faster than what could be measured for all types of liposomes tested, even without addition of peptide.

Sammendrag

Med den økende forekomsten av multiresistente patogene organismer er det et stort behov for alternativer til de konvensjonelle antimikrobielle medisinene som finnes på markedet i dag. Antimikrobielle peptider (AMPer) er lovende som utgangspunkt for å utvikle fremtidens antibiotika, men mer kunnskap om virkningsmekanismen deres er nødvendig for at dette skal være mulig. Det er kjent at peptidene interagerer med plasmamembranen til mikrobene og at denne interaksjonen er nødvendig for den antimikrobielle aktiviteten. For å undersøke disse lipidspesifikke interaksjonene til AMP ville vi bruke liposomer, sfæriske fosfolipidbilag, som etterlikner membranene til bakterier og pattedyr. Strukturelle endringer i bilaget ved tilsetning av peptid kan da karakteriseres. Lavvinkel røntgen/nøytronspredning (SAXS/SANS) er optimale teknikker for å undersøke endringene på nanoskala. Det er derimot funnet at liposomer alene feller ut i løsninger med AMPer, som gjør at det ikke er mulig å se den mikroskopiske virkningsmekanismen med disse teknikkene. Det trengtes derfor en metode for å stabilisere liposomene mot aggregering som fortsatt tillot peptidene tilgang til å påvirke membranen. I denne oppgaven har to typer polyetylenoksidderivater blitt testet for deres potensial for å stabilisere liposomer for AMP-indusert aggregering. Begge de modifiserte liposomsystemene sin kinetiske stabilitet, struktur og interaksjon ble testet, med og uten tilsatt AMP. I tillegg ble en kjent flokkulant, polyetylenimin (PEI) testet på systemet for sammenlikning med peptidet. Det ene systemet besto av å tilsette n-alkyl-polyetylenoksid (C_n-PEO) etter liposomene var blitt laget. For det andre systemet ble polyetylenoksidmodifiserte fosfolipider (”PEGylerte” lipider) inkludert i bilaget under preparasjonen. Begge metodene stabiliserte liposomene gjennom sterisk repulsjon. Selv om tilsetning av n-alkyl-polyetylenoksid gjør systemet mer fleksibelt når det kommer til tilberedning, ble det vist at C_n-PEO påvirker membranstrukturen til liposomene i stor grad. Ved 37 grader celsius løser C_n-PEO delvis opp bilager og lager blandede miceller med fosfolipidene, og de vekselvirker også med peptidene. De mange uønskede interaksjonene gir resultater som er vanskelige å analysere. De PEGylerte lipidene stabiliserte derimot liposomene uten å introdusere noen av disse uønskede effektene i systemet. Polymerne på overflaten påvirket heller ikke peptidet sin tilgang til membranen. For å kunne kvantitativt analysere data fra lavvinkelspredningen, ble analytiske spredningsmodeller utviklet både for liposomsystemet og for å beskrive innsetning av peptid i denne systemet. Disse modellene kunne beskrive de eksperimentelle dataene fullstendig. Et av de mer populære påstandene for AMPer er at de gjør membranen mer permeabel for vann og kan dermed utligne protongradienter. Det valgte modellsystemet ble derfor testet for tiden det tok for vann å utveksle over membranen ved å bruke SANS for å se om metoden kunne brukes til å studere effekten AMP har på vanntransporten. Fordelen SANS har over andre metoder som måler diffusjonen av vann er at man kan samtidig se endringer i struktur. Fullstendig utveksling av vann skjedde derimot raskere enn det som kunne måles for alle liposomene som ble testet. Dette skjedde uten tilsats av peptid som viser at lipid membraner er fullstendig permeabel for vann på eksperimentelle tidsskalaer.

Acknowledgements

The work presented in this thesis was carried out at the Department of Chemistry, University of Oslo under the supervision of Associate Professor Reidar Lund in the period from August 2016 to May 2018. Much of the data were collected at the European Synchrotron Radiation Facility in Grenoble, France and at Forschungs-Neutronenquelle Heinz Maier-Leibnitz in Münich, Germany.

I would first like to thank my supervisor Reidar Lund who has given me the opportunity to work in his group. During my master thesis I have gotten to visit large scale research facilities for X-ray and neutron science several times. These experiences have been invaluable to me and they would not have been possible without you. You have also provided excellent supervision through the entire process of experimental work, analysis and writing, and I am very grateful to have had you as my supervisor.

Secondly I want to thank Josefine Eilsø Nielsen, who has been working with me on the same project. Much of this work is the result of experiments and analytical work we have cooperated on and I do not think I would have gotten this far without you. We have spent many late nights together doing experiments at the synchrotron and research reactor, as well as at home working on the model. You have also provided me with plenty of feedback during the writing. I am therefore very happy and thankful that you were chosen for this PhD and I hope to be able to give equal support to you in the future.

I would also like to thank my co-supervisor professor Ute Krengel and Dr. Matthias Amann for their feedback on the writing which really helped to give the thesis a better structure. The other people I would like to acknowledge are: the other master students in our group, Synne Myhre and Mikkel Killingmoe Christensen that have both been of great help during experiments at the synchrotron and reactor; Dr. Vitaily Pipich, who has helped us both at the experiments but also with the model and the QtiKWS-software; Dr. Kenneth Knudsen who did measurements for us at the JEEP II-reactor at Kjeller; Dr. Lutz Willner for the synthesis and information about the polymers; and Martha Brennich for her help with the experiments at BM29.

Finally, I would like to thank my partner Ignacio Cuervo (who also gave feedback on the thesis) and my family for all their love and support throughout the all the work that I have put into this thesis.

Abbreviations and symbols

A	Scattering probability amplitude
$\mathbf{a_0}$	Equilibirum area of surfactant head group / wave amplitude
a	Area of surfactant head group / activity
AMP	Antimicrobial peptide
CAC	Critical aggregation concentration
CMC	Critical micelle concentration
Cn-PEO	n-alkyl poly(ethylene oxide)
DLS	Dynamic light scattering
DMPC	1,2-dimyristoyl-sn-glycero-3-phosphocholine
DMPE-PEG	1,2-dimyristoyl-sn-glycero-3-phosphoethanolamine-N -[methoxy(polyethylene glycol)-2000]
DMPG	1,2-dimyristoyl-sn-glycero-3-phospho-(1'-rac-glycerol)
DSC	Differential scanning calorimetry
DVLO theory	Derjaguin-Landau-Verwey-Overbeek theory
$\mathbf{F(q)}$	Form factor
γ	Interfacial free energy per unit area
$\mathbf{I(q)}$	Intensity
k_B	Boltzmann constant
MLV	Multilamellar vesicle
μ_N^o	Mean free energy per molecule in aggregate of N molecules
n-alkyl-PEO	n-alkyl-poly(ethylene oxide)
p	Packing parameter

$\mathbf{P_{agg}}$	Aggregation number
$\mathbf{P_i(z)}$	Volume probability of component i at position z
$\mathbf{P(q)}$	Form factor
PEG	poly(ethylene glycol)
PEGylation	conjugation of PEO/PEG
PEI	Poly(ethylenimine)
PEO	Poly(ethylene oxide)
POPC	1-palmitoyl-2-oleoyl-sn-glycero-3-phosphocholine
q	Momentum transfer in scattering experiment
R_g	Radius of gyration
R_H	Hydrodynamic radius
ρ	Scattering length density
SANS	Small Angle Neutron Scattering
SAS	Small Angle Scattering
SAXS	Small Angle X-ray Scattering
$\mathbf{S(q)}$	Structure factor
T	Temperature
ULV	Unilamellar vesicle
V	Volume

Contents

1 Introduction

The history of antibiotic resistance reaches as far back in time as antibiotics themselves. Penicillin resistant bacteria had been discovered even before the compound was first introduced to the public in the early 1940s. At the same time, its discoverer, Alexander Fleming, cautioned that misusing the drug would lead to resistant bacteria, a prediction that was coming true only few years after the drug's introduction with over of 14% of staphylococcus strains already having developed resistance in 1946 [1]. Today, despite the development of hundreds of different antibiotics [2], the scenario is looking much worse. Antimicrobial resistant infections already claim at least 700 000 lives worldwide every year, and if the trend continues the death toll is expected to rise dramatically. The development of new and better alternatives to our conventional antibiotics is necessary if the battle against pathogens is to be maintained at a comfortable level.

Antimicrobial peptides (AMPs) are a class of natural compounds that, similarly to compounds like Fleming's penicillin, have existed for a long time in an evolutionary perspective [3]. From the name one can already see some differences. Antimicrobial suggests a broader spectrum of toxicity than conventional antibiotics that are specific for certain bacteria. The fact that they are peptides indicates that they are biologically and chemically more complex molecules than most conventional antibiotics. What makes them the most interesting, however, is that despite their evolutionary age, widespread resistance among microbes against AMPs have not yet been reported [4]. The microbes likely have trouble developing a defence against the peptides for one simple reason: the AMPs attack the integrity of the entire cell by interfering with the life-defining cell membrane itself through multiple hydrophobic/anionic targets rather than targeting any specific biochemical pathway [4][5]. Evolution of an entirely new membrane composition is certainly more complex than the alteration or introduction of a single gene sequence, as is usually the case for resistance against conventional antimicrobials [6]. This certainly makes them an obvious candidate for future drug development, but there are also two major problems facing AMP-based drugs:

1. AMPs, being peptides, are very easily degraded in the mammalian blood stream.

2. As might be expected, they also show a certain degree of toxicity against human cells.

To develop compounds that might solve these problems, precise knowledge of the AMPs mechanism of action in the membrane is required [4]. Several mechanisms have been proposed for different peptides and some of the most popular suggestions are illustrated in Figure 1, taken from Nguyen et al. [7]. Since a lytic activity is often observed, different types of pore formation by the peptide that effectively lyses the cell have been suggested, making cell content leak out either by forming a barrel-like structure (as suggested for cyclic peptides such as Gramicidin S [8][9]) or by changing the membrane curvature to form a so called toroidal pore (as suggested for the popular AMP Magainin [10] [11]). Another possiblity is the so called "carpet model" where the peptides bind on the surface until a threshold concentration is reached and the membrane is disintegrated in a detergent-like manner [12]. The peptide might also intercalate into the membrane, disrupting the lipid packing [13]. Epand et al. suggest that the cationic AMPs might cluster the anionic lipids and in this way lead to permeabilisation by boundary defects between the different lipid phases [14] [15]. Other mechanisms, such as acting through a change in the electrochemical potential across

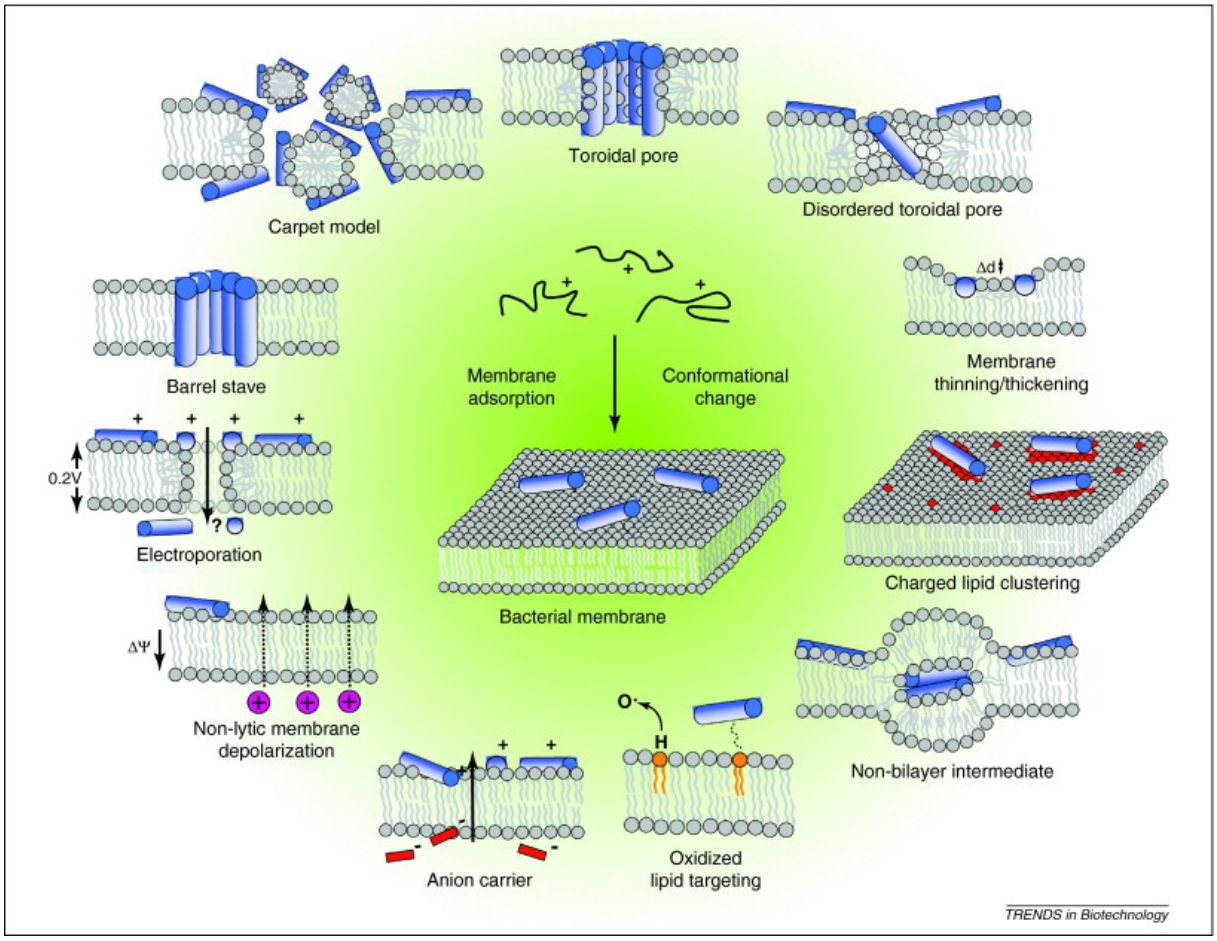

Figure 1: The most popularly suggested mechanisms of AMPs. Taken from Nguyen et al. [7].

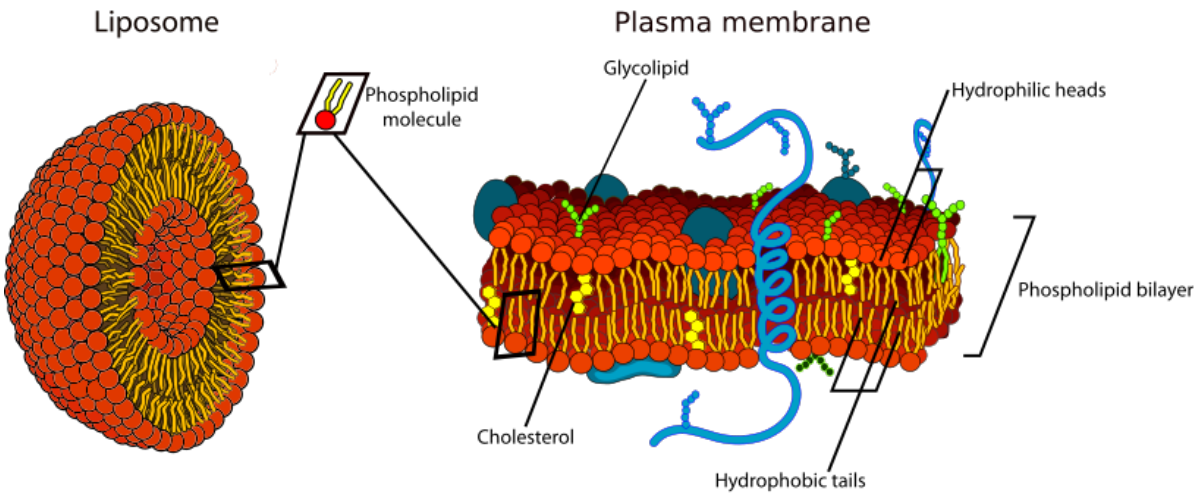

Figure 2: Comparison of liposomes with the plasma membrane of living organisms.

the membrane, have also been suggested. The possibility that antimicrobial activity of the peptides might extend further than their disruption of the membrane by interacting with intracellular targets after translocation should also be considered [16], but the interaction with the membrane is regardless a vital step in their mode of action. A review of the different mechanisms of membrane activity can be found in an article by Wimley and Hristova [17], who also point out that none of these models fully explain all of the experimental observations and that these questions must be answered before AMPs can lead to discovery or development of clinical treatments.

Small angle scattering (SAS) with X-rays or neutrons is a technique that is used for investigating structures on the nanoscale. It is popularly used for studying these kind of systems in solution. The time evolution of systems can also be followed using SAS, making it a powerful tool for obtaining structural as well as dynamical information of the system simultaneously. SAS is therefore an optimal technique for investigating the microscopic actions AMPs have in the bilayer since it probes the correct size domain and allows the interaction to be studied under realistic conditions. The interaction of the peptide would be difficult to discern in the complex living plasma membrane, however, so using bacterial membranes is not a good option for these techniques. An appropriate model system keeping only the relevant compounds of the membrane is better to fully decipher the peptide-membrane interaction.

Liposomes are self-assembled vesicles composed of a phospholipid bilayer, and therefore good candidates for a very simple model system of the basic plasma membrane of living organisms. A comparison of liposomes and a section of a plasma membrane can be seen in figure 2. They are examples of organized structures that are spontaneously formed from initial disorder due to environmental conditions, such as the hydrophobic effect. These lipids vesicles are thought to be more biologically relevant model membranes than for example supported lipid bilayers as they are topologically similar to cells having a single interior compartment [18]. The structure of the bilayer of the liposomes has been studied using SAS techniques before [19][20][18][21] [22]. Using liposomes as a model system and SAS to study it has a significant advantage over alternative techniques because it allows the structure of the bilayer to be determined in it's most natural state - in solution. This is particularly beneficial when one wants to study changes in the membrane

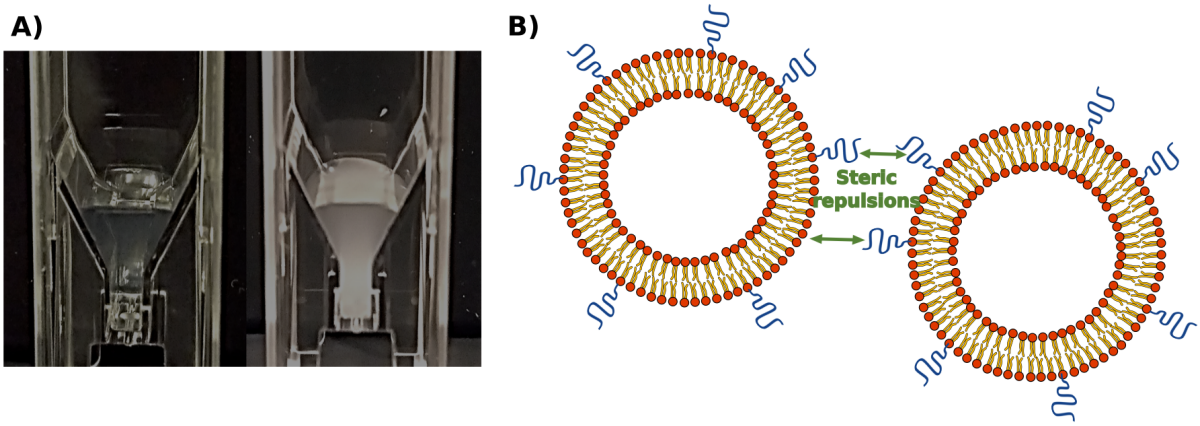

Figure 3: A) The effect of adding PEI to liposomes stabilised with C_{14}-PEO and without a steric stabiliser, showing the flocculation in the non-stabilised system. Pictures taken by Erasmus student at UiO, Philip Nickl. **B)** Illustration of liposomes sterically stabilised by polymers on the surface. The polymers cause steric repulsions that keep the liposomes from flocculating. Figure was made using the open source Inkscape software package.

due to additives since this can be done in real time and without changing the sample environment before measuring. The downside to the technique is that the the data is more difficult to interpret and requires much more analysis than the use of microscopy techniques or diffraction to determine the structure of the bilayer. If the information is properly extracted by the analysis, however, the determined structure should be a more correct representation of the actual bilayer.

By designing liposomal bilayers with a specific phospholipid-composition very crude mimics of the bacterial and eukaryotic plasma membranes can be produced. One of the main difference in the lipid composition of the bacteria and eukaryotes lies in the comparatively high amount of negatively charged phospholipids in the outer leaftlet of the bacterial membrane. These negative charges are more or less absent in the outer membranes of multicellular eukaryotes [23], where the plasma membrane primarily consists of zwitterionic phospholipids and cholesterol [24]. For bacteria, negatively charged phospholipids have been found to be integral for the viability of the organism [25]. Since many AMPs are cationic, the anionic charge of the membrane is thought to play an important role in the selectivity of AMPs towards microbes [24]; AMPs that are not cationic are less selective in their targets and more toxic against mammalian cells [16]. The presence of lipids with anionic head groups is therefore an important characteristic of the liposomal model system.

Although liposomes themselves form a stable colloidal system in salt poor solutions, initial tests showed that they aggregated and precipitated in the presence of a cationic AMP. This, although showing a clear electrostatic flocculation effect of the peptide, would of course make it difficult to study exactly how the AMPs work on the liposomal membrane. The same effect was observed when adding poly(ethylenimine) (PEI), a cationic polymer that is known to disrupt the cell membrane [26]; a depiction of this macroscopic phase separation with PEI can be seen in Figure 3. Some way of preventing the liposomes from flocculating while still allowing the peptide access to the membrane was therefore necessary.

One candidate for a stabilisation of the liposomes is the attachment of poly(ethylene oxide) (PEO) (also referred to as poly(ethylene glycol) (PEG)) to the surface of the liposomes, popularly called PEGylation. PEGylation of liposomes is a extensively used technique in the design of drug

delivery systems. Unmodified liposomes are recognized as foreign objects to the innate immune system of mammals. They are therefore cleared quickly from the bloodstream, significantly lowering their drug delivery capacity. PEGylation reduces the removal leading them to be called ”stealth” liposomes due to their ability to evade the immune system and therefore enter the tissues from the blood stream [27]. The stealth capabilities of the PEGylated liposomes are generally assumed to originate from the sterical hinderance they provide against the binding of opsonins, molecules that target foreign object for degradation in the body. It is also suggested, however, that the integral function of the PEGylation is rather their ability to prevent self-aggregation of the liposomes [28]. While many modes of introducing PEO to the surface of the liposomes have been attempted, the most effective for *in vivo* prolongivity has been the incorporation of PEGylated phospholipids in the bilayer [29]. As it is a well tested steric stabiliser of liposomes, the hypothesis was that PEGylation could also be successful in hindering AMP-induced aggregation.

The block co-polymer n-alkyl-PEO was also considered as a possible stabiliser for this project. While it might be a bad option for stealth liposomes to be used *in vivo*, it still stabilises the liposomes from a macroscopic phase separation (as seen in Figure 3). Stabilisation with n-alkyl-PEO could allow for more flexibility when designing the liposomal systems since it can be acquired in larger amounts and be added after the preparation of the liposomes. To the author's knowledge the microscopic interactions of the n-alkyl-PEO and liposomes have not before been studied. As the block co-polymer spontaneously self-assembles into micelles, but only at a relatively high concentration, it was also interesting to see how the formation of these micelles would affect the stability of the system versus the dispersed molecules, both in terms of the interaction with liposomes and peptide/PEI.

The composition of the model systems tested in this thesis are illustrated in Figure 4. The liposomes without any steric stabiliser consisted of 1,2-dimyristoyl-sn-glycero-3-phospho-(1'-rac-glycerol) (DMPG) and 1,2-dimyristoyl-sn-glycero-3-phosphocholine (DMPC) phopholipids in the molar ratio of 1:9, respectively, with DMPG providing the net negative charge to the membrane. DMPG is found in the bacterial membrane and can constitute as much as 25 % of the total lipid content and is thought to play a significant role in stabilisation of the membrane [30]. Zwitterionic phospholipids with phosphatidylcholine (PC) and phosphatidylethanolamine (PE) head groups make up the majority of the membrane phospholipids in both eukaryotes and prokaryotes. PC-lipids have been preferred in studies due to them forming vesicles with relative ease compared to PE [25]. The PC-lipid DMPC therefore also represents the zwitterionic phospholipids of the cell in our model system. Unilamellar vesicles (ULVs) of 100 nm in diameter were mainly used, as it allowed both the bilayer and the size of the liposomes to be effectively studied with small angle scattering techniques.

Indolicidin, illustrated in Figure 5, was used as a model AMP. This peptide consists of only 13 amino acids and was originally discovered in the neutrophils (a type of white blood cell) [31]. It is found to take up a structure consisting of random coil segments as well as turns in buffer solutions [32]. It has a very wide range of antimicrobial activity, but very little is known about its mode of action [33]. PEI, mentioned earlier in the introduction, was also used for testing the stabilisation and for comparison with the interaction of the peptide.

The two different systems of PEO-stabilization that were considered as candidates for the model liposome can be summed up as follows:

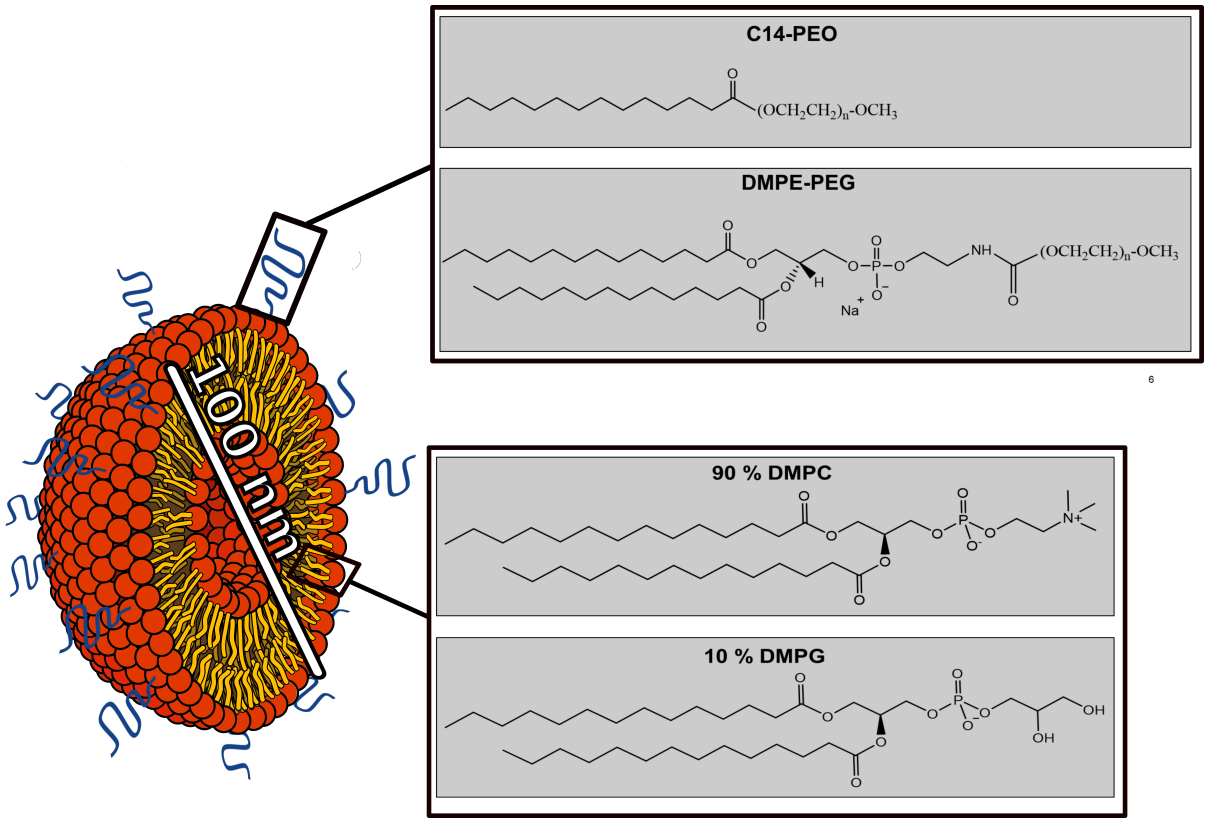

Figure 4: The composition of the liposomes used for the model system in this project. All liposomes consisted of 90 % moles of the zwitterionic DMPC and 10 % moles of negatively charged phospholipid (DMPG or in the case of PEGylated liposomes, DMPG and DMPE-PEG). For steric stabilisation, either C_{14}-PEO was added to the liposomes after preparation or 2.5 % moles DMPE-PEG was added during the liposome preparation.

- Addition of free n-alkyl-poly(ethylene oxide) (Cn-PEO) to the liposomes. In our system, C_{14}-PEO was chosen because it has the same hydrocarbon chain length as our phospholipids and was by that reasoning expected to affect the packing of the chains to a lesser degree upon insertion.
- Incorporation of PEO-modified (PEGylated) phospholipids in the making of the liposomal bilayer, in our case 1,2-dimyristoyl-sn-glycero-3-phosphoethanolamine-N- [methoxy(polyethylene glycol)-2000] (DMPE-PEG), which is a popularly used stabiliser in stealth liposomes.

For option one, three concentrations of PEO were studied; one above the critical micellar concentration (CMC), one approximately at the CMC and one below the CMC. This was done to see whether the formation of micellar structures would affect the integrity of the system. Both options were tested in terms of their effect on the liposomal structure, stability over time and their interaction with AMPs as well as with PEI using scattering techniques and calorimetric measurements. In order to monitor any changes in the size of the liposomes that would occur instantenously and over time when adding either C_{14}-PEO or, later, PEI/peptide to the stabilised system, dynamic light scattering experiments were performed. Dynamic light scattering is a technique that is used to find the radius of hydration through measuring the diffusion of particles in solution. Small angle X-ray scattering was used to see any structural changes in the membrane induced by the C_{14}-PEO or the PEI/peptide. To analyse the small angle scattering data from the liposomal structures and the effect of adding C_{14}-PEO, PEI and peptide, new analytical models were required. Part of the aim

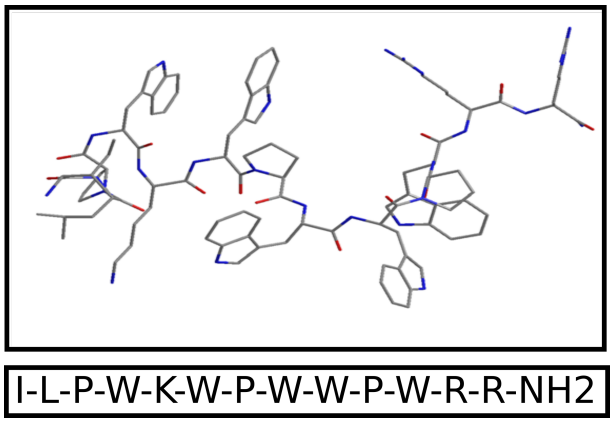

Figure 5: Illustration of the AMP Indolicidin with the amino acid sequence written below. Figure was drawn using Chem3D software from PerkinElmer Informatics.

of the study was therefore to develop these theoretical models and test them on the experimental data. Differential scanning calorimetry was used to see any change in the transition temperature of the hydrocarbon chains in the membranes due to addition of the C_{14}-PEO.

Since many of the proposed mechanisms for AMPs suggest that the bacterial cells are lysed, causing an influx of water into the microbial cell due to the osmotic pressure, it was of interest to check whether such an effect could be measured with our liposomal systems. Therefore, an experiment was designed and performed to measure the water transport across the membranes of liposomes using small angle neutron scattering (SANS). If such transport could be observed, one could then measure the difference in transport when adding peptide to the system. Although such studies on the water transport across lipid bilayers been performed before, SANS provided a chance to monitor the water transport and the structural changes in the membrane simultaneously. The experiment was attempted with different lipid compositions and liposome sizes to see if this would affect the water permeability. Therefore, in addition to the chosen model system described above, measurements were also done on liposomes made of 1-palmitoyl-2-oleoyl-sn-glycero-3-phosphocholine (POPC) and cholesterol, a possible mimick of the mammalian plasma membrane.

The three aims of the study might be summarized as follows:

- Test the different PEO-stabilised liposomal system for their applicability in studying the mechanism of AMPs.
- Develop analytical models that can describe the structure of the liposomal bilayer and the changes that occur in the structure upon peptide addition.
- Investigate whether the system can be used for studying differences in water transport across the membrane using small angle neutron scattering.

The information acquired from these investigations lays the foundations for future research using other lipid compositions and AMPs that is beyond the scope of this thesis.

2 Theoretical background

2.1 Self-assembly of amphipathic molecules

2.1.1 Principles of self-assembly

The self-assembly of molecules is one of the essential prerequisites of life: it governs the structure of the biological membrane as well as the folding of protein and DNA. There are numerous reasons why molecules would self-assemble, but perhaps the most biologically relevant one is the hydrophobic effect. Molecules that are made up of one hydrophobic part, usually a hydrocarbon, and a hydrophilic part tend to aggregate in an aqueous environment so that the hydrophobic part of the molecules are shielded by the hydrophilic part from the surrounding solvent. This is an entropic effect, as the water molecules are forced to order around the hydrophobic solute. The ordering consists of the water molecules orienting so that the least number of tetrahedral charges point toward the hydrophobic solute. This way, these charges can still participate in hydrogen bonding with other water molecules. While the water molecules may regain their hydrogen bonds by restructuring and thus have minimal increase in enthalpy, the new water structure is still more ordered than that of the bulk. When nonpolar groups come together, the surface area exposed to the water is reduced, thereby reducing also the amount of water that has to order around the structures. The hydrophobic groups themselves also have an attractive interaction that is not accounted for by mere van der Waals forces, but this hydrophobic interaction is poorly understood [34]. The hydrophobic interaction might also govern the antimicrobial activity among certain AMPs that are hydrophobic [16].

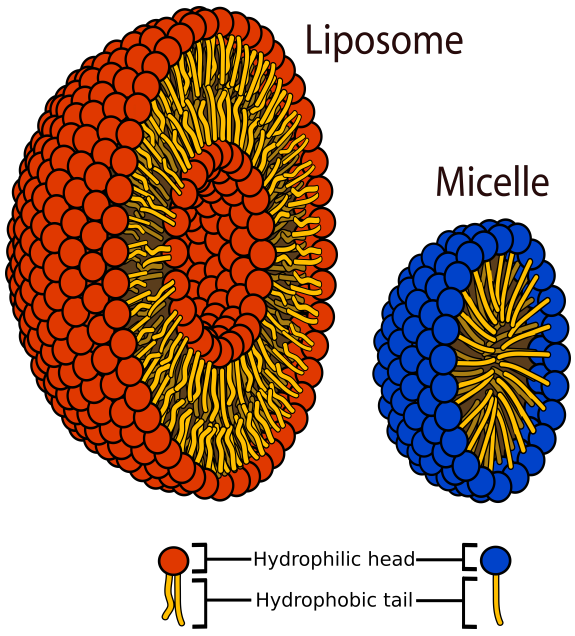

Figure 6: Examples of self-assembled structures: micelles and liposomes.

Classical examples of self-assembled structures from amphiphilic molecules are micelles and liposomes, seen in Figure 6). It is also worth noting that the same effect leads to structure formation by peptides alone, as is the case in spontaneous protein folding due to the presence of hydrophobic

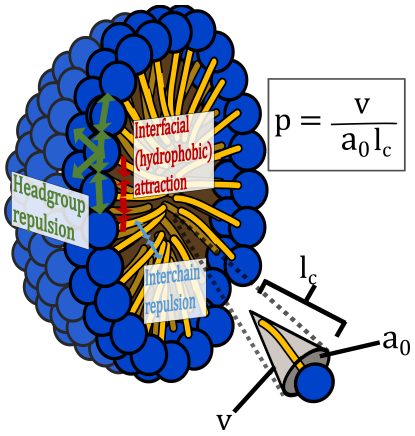

Figure 7: Illustration of the forces that governs the preferred molecular orientation of amphiphiles and the packing parameter. Inspired by Figure in [35].

side chains. The equilibrium structure is a result of a balance between the hydrophobic interaction, causing the hydrophobic chains to aggregate, and the inter-repulsion of the head groups, as illustrated in Figure 7. a_0 is the equilibrium area of the head group where the energy of the molecules in the structure is minimised. The total interfacial energy per molecule in an aggregate of N molecules μ_N^o can be written as

$$\mu_N^o(a) = \gamma a + \frac{K}{a} \tag{1}$$

where γ is a positive interfacial free energy per area due to the hydrophobic interaction (giving the attractive force), while K is a constant representing the strength of the repulsive forces. Assuming both forces act in the same plane, the minimum of this function is found to be at

$$a_0 = \sqrt{\frac{K}{\gamma}} \tag{2}$$

Inserting K from equation 2 into equation 1 and rearranging gives

$$\mu_N^o(a) = 2\gamma a_0 + \frac{\gamma}{a}(a - a_0)^2 \tag{3}$$

where the free energy is a function of the measurable parameters a_0 and the interfacial tension γ [35]. As might be seen by setting $a = a_0$, the first term in equation 3 is the minimum energy the molecules of the aggregate can have, and both a decrease and increase of a is therefore energetically unfavourable.

Structure formation is from this argument governed by the geometrical constraints that the equilibrium surface area imposes and can classically be estimated numerically through the so-called packing parameter, p:

$$p = \frac{v}{a_0 l_c} \tag{4}$$

where v is the volume of the hydrophobic chain and l_c is the length of the hydrocarbon chain [36]. Molecules with a packing parameter below $1/3$ are cone-shaped and tend to form spherical micelles, those with $1/3 < p < 1/2$ can form worm-like micelles, while those with $p > 1/2$ will form bilayers like in liposomes.

Following the law of mass action, a certain concentration of molecules is required to form aggregates. This critical aggregate concentration (CAC), or as more commonly used for micelle formation,

the critical micellar concentration (CMC) is defined as the concentration where the rate of association is equal to the rate of dissociation. The equilibrium constant for this "reaction" is given by

$$K_{\text{agg}} = e^{N(\mu_N^o - \mu_1^o)k_B T} \tag{5}$$

where k_B is the Boltzmann constant. μ_1^o here denotes the free energy of a molecule in solution (a monomer). Assuming the validity dilute solution theory [37], the law of mass action then gives the concentration of molecules in aggregates of N X_N as being:

$$K_{\text{agg}} = \frac{X_N/N}{X_1^N} \rightarrow X_N = N\left(X_1 e^{\frac{\mu_1^o - \mu_N^o}{k_B T}}\right)^N \tag{6}$$

Since $\sum_N X_N$ has to be equal to the total concentration, X_1 cannot exceed $e^{-\frac{\mu_1^o - \mu_N^o}{kT}}$, so the critical aggregation concentration can be estimated by this value:

$$\text{CMC} \approx e^{-\frac{\mu_1^o - \mu_N^o}{k_B T}} \tag{7}$$

Inserting equation 3 or an equivalent expression for the free energy of the molecules in the aggregated structure, will then give a relatively simple expression dependent only on the interaction energy [38][36]. The concentration of monomers will remain constant upon further addition after the CMC with the excess monomer forming more aggregates. Although it might seem that the CMC has a simple dependency on temperature in this expression, it is important to note that the hydrophobic effect and interaction also has a complicated dependency on temperature resulting in different values for γ and a_0 at different temperatures.

The CMC of a micelle-forming molecule is characterized by a number of changes in physiochemical properties of the solution, such as surface tension, turbidity, viscocity and many more. The CMC can therefore be found by monitoring any of these properties as one increases the concentration of the micelle-forming component [39]. With small angle scattering the scattering from the micellar structure will appear at the CMC and increase in signal strength with increasing concentration after this point.

What once aggregates have started appearing in solution? That depends highly on the structure of the formed aggregates. While for example planar bilayers might continue to aggregate into infinite structures, spherical aggregates such as micelles have an equilibrium aggregation number. Both cases will be discussed further in the next two sections.

2.1.2 Liposomes

Phospholipids have two fatty acid chains constituting the hydrocarbon chain, but only one polar head group, making v comparably large in expression 4 so that they prefer to form bilayer structures. Also, the double hydrocarbon tails provides a large hydrophobic interaction potential, which equation 7 shows will give a very low value for the CMC [35]. This means that these bilayers will form and stay thermodynamically stable even at very low concentration, a property that is obviously of great importance to biomembranes as they should remain intact even at low concentrations of solved phospholipid.

Why would a bilayer form a liposome rather than an infinite planar structure? One consideration is the entropy will favour a number of less aggregated structures over one large structure.

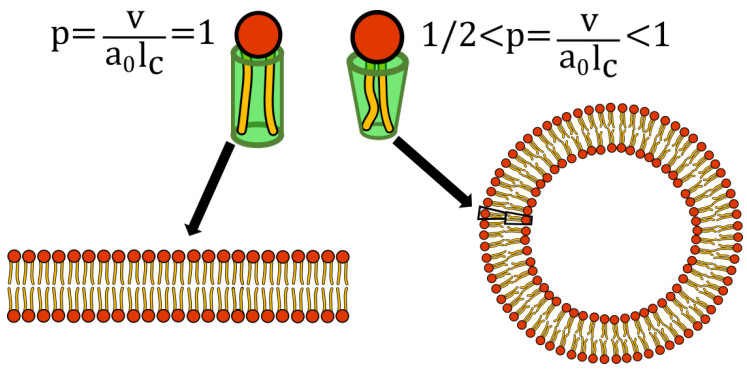

Figure 8: Packing of lipids in bilayers. Formation of a spherical vesicles requires the packing parameter to be at least slightly below 1.

Another is that the edges of the planar bilayer will have exposed hydrophobic groups, which is also entropically unfavourable in terms for the hydrophobic effect. Therefore, the favoured structure for a bilayer will be a vesicle, as long as the area a_0 can be maintained in the curved bilayer [35]. This requires the packing parameter in equation 4 to be less than 1, as illustrated in Figure 8. The thermodynamically preferred structure will then be the smallest aggregation number where the outer head group area is not forced to exceed a_0. Note that the molecules in the inner leaflet do not experience this packing restriction as their curvature will be opposite, as illustrated in Figure 8.

It is found, however, that liposomes are in general not thermodynamically stable structures, and for the most part are not formed spontaneously [40]. This is largely due to the effect of curvature on the interaction energy (equation 1). The mean energy for each amphiphile in spherical bilayer can be expressed as

$$\mu_N^o = 2\gamma a_0 \left(1 - \frac{Dt}{4R^2}\right) = \mu_\infty^o - \frac{\gamma a_0 Dt}{2R^2} \tag{8}$$

where t is the thickness of the bilayer. D is the distance at which the repulsive forces can be modelled as laterally acting - if the head group repulsion dominates, this somewhere outside where the interfacial attraction acts (positive D), while if the interchain repulsions dominate it will act below this interface (negative D). For phospholipids, D is usually negative due to the double chains, so the curvature gives an increase in energy. If $R \to \infty$, the energy goes towards that of a infinite planar bilayer, μ_∞^o. Energetically, although not entropically, the formation of large liposomes is generally favoured over small ones [35].

Liposomes are generally classified into two types: multilamellar vesicles (MLVs; liposomes in an onion-like arrangement) and unilamellar vesicles (ULVs). For the purpose of this thesis, the unilamellar are of greatest interest since they more easily will show the effect of additives such as a peptide [18]. One further distinguishes between small (<0.1 µm) and large ULVs (>0.1 µm)[41]. As discussed, the size of the liposomes are an important factor in their thermodynamic stability, but it also has implications for the data collection and modelling. While it is of interest to see the full size of the liposome using small angle scattering techniques, making them too small will also increase the curvature of the bilayer and possibly introduce a degree of asymmetry between the inner and outer leaflet of the liposomes. Although scattering models for the bilayer can account for this asymmetry, it is unwanted as it further complicates the modelling of the peptide interaction later. It is also worth noting that the typical prokaryotic cell is on the scale of 0.5 µm [42], with the

eukaryotic cell being in general 10-100 times larger, and so making the liposomes too small might also introduce artefacts that are not present in living cells.

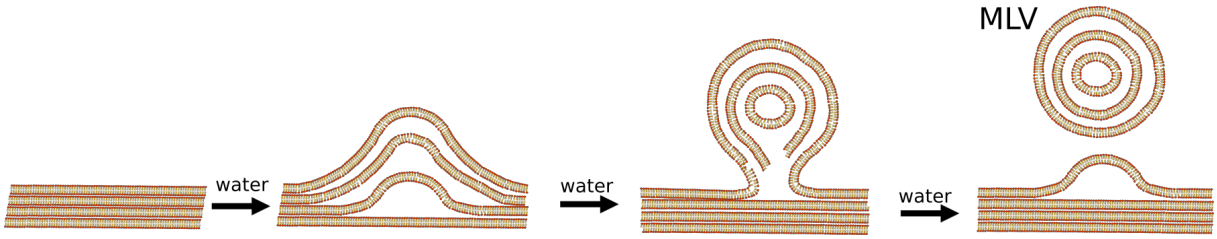

Figure 9: Mechanism of MLV formation from hydration of a dry lipid film as suggested by [43].

Originally found by their discoverer A.D. Bangham [44], multilamellar vesicles are spontaneously formed from the swelling of a dry phospholipid film in water. A suggested mechanism of this is illustrated in Figure 9. As discussed above, smaller liposomes have higher free energies, and so energy must be put into the system to make them. This can be done with mechanical forces such as extrusion or sonication. Once the smaller ULVs have been formed they can be kinetically stable and remain as small ULVs for extended periods of time under correct conditions [45], as is also demonstrated repeatedly in this thesis.

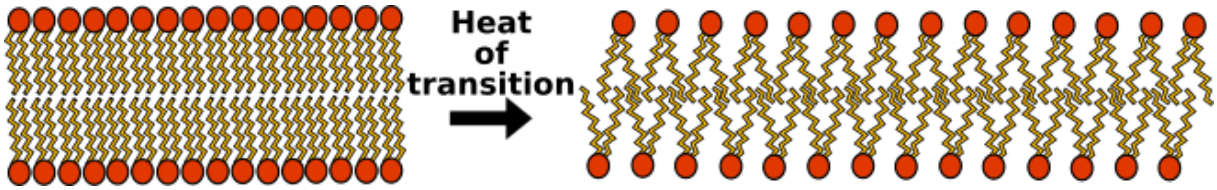

Figure 10: Illustration of the changes that occur in the transition from the lamellar gel to the lamellar liquid crystalline phase, the main phase transition of lipid bilayers.

Another important consideration for the liposomes are the different phases of the bilayer. At low temperatures the bilayer will be in a gel state, with the lipid tails closely packed and fully extended in the all-trans conformation. At higher temperatures, the lipid tails with adopt a liquid crystalline phase with the tails more randomly oriented (see Figure 10). One would therefore expect that the bilayer thickness would decrease when the temperature is above this transition temperature. The transition from the lamellar gel to the lamellar liquid crystalline phase constitutes the largest enthalpic event of the bilayers. The hydrocarbon chains gets increased rotameric freedom, the head group gets increased hydration and the intermolecular entropy increases [46]. This requires a large amount of energy input in order to increase the volume and bilayer area, both working against the attractive interfacial forces. For phospholipids bilayers not containing any cholesterol or other sterols, the transition is a reversible and cooperative process [47]. One can therefore find a specific transition temperature that is characteristic of the bilayer. It is the phospholipid content of the bilayers that determine their transition temperature; while phospholipids with long, saturated fatty acid chains are expected to promote elevated transition temperatures, unsaturated fatty acids disturb the packing of the chains and lower the melting temperature. The polar head group also affects the transition temperature, and therefore it can also depend on environmental factors such as the pH and electrolyte concentration in the solution [48] [49]. Before the main transition from gel to the liquid crystalline phase, some lipids also exhibit a so-called pre-transition where the

membrane goes from being planar to getting ”ripples” in the surface due to fluid lipid lines in the otherwise gelated bilayer causing local bending of the membrane [50] [51].

Liposomes have been extensively studied, both for their promise as a drug delivery system and for their semblance to biological membranes. Another type of system that has attracted a lot of attention is self-assembled structures of synthetic polymers. An example of such a system is the block co-polymer C_{14}-PEO used in this thesis, and their properties will therefore be described in the next section.

2.1.3 Block co-polymer micelles

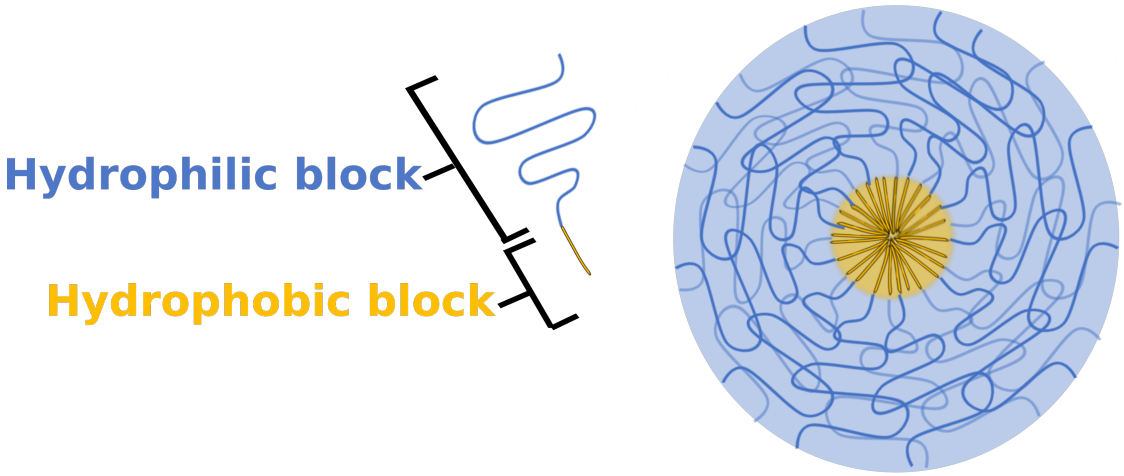

Figure 11: Illustration of a block co-polymer micelle with the usual segregation of hydrophobic core and and hydrophilic shell.

Block co-polymers are molecules that consists of two or more types of polymer covalently linked together. Such structures can act analogously to surfactants if the different blocks have different solubility, such as one hydrophobic and one hydrophilic block. An example is the diblock co-polymer alkyl-PEO, consisting of a hydrophobic alkyl polymer and the hydrophilic poly(ethylene oxide). In this a case the block co-polymers will self-assemble into defined structures as discussed in Section 2.1.1. Depending on the block ratios, different kinds of micelles can be formed. In this thesis the alkyl-PEO generally favours star-like micelles, as depicted in Figure 11.

The free energy of a block co-polymer micelle can be estimated by three terms [52]:

$$F_{\text{micelle}} = F_{\text{core}} + F_{\text{shell}} + F_{\text{interface}} \tag{9}$$

$F_{\text{interface}}$ constitutes the driving force of aggregation, and it arises from the favourable minimisation of the interface between the core and solvent that occurs due to the hydrophobic effect. It is counterbalanced the F_{core} and F_{shell} terms, which arises from the unfavourable arrangement of the core and shell molecules. While the for star-like micelles the F_{core} term is generally so small that it can be ignored, the hydrophilic polymer in the block co-polymer micelle illustrated in Figure 11 can take up a number of configurations, thereby changing the so-called ”shell” of the micelle and

thereby also F_{shell}. This problem is usually therefore tackled by mean-field theories, where rather than trying to account for the individual interactions of the polymer chains, each chain is thought of as acting independently but in a mean force field representing the mean interaction. For many systems, however, the mean field approach fails because of the strong repulsion between the polymer chains causing excluded volume effects. This prevents the polymer from folding back on itself and causes strong correlations between different segments on the chain. One way of accounting for excluded volume effects is by using scaling arguments, where the polymer is partitioned into so called blobs of non-overlapping polymers segments. The detailed description of the free energy is not of importance here, but can be found reviewed for star-like micelles in the book chapter by Lund et al. [52]. What is important to note is the difference between this system and the regular surfactant micelles: while the driving force for micellation is still the interfacial (hydrophobic) attraction, the counteracting force is now not only the repulsion in the head groups, but also the conformational entropy of the polymer head group. Long polymer chains are likely to be stretched in the micelle compared to their dissolved state, thus adopting a more ordered state. Polymer conformations are further discussed in Section 2.3.

2.2 Colloidal and steric stabilisation

The forces that govern the stability of liposomes are many. The classical Derjaguin-Landau-Verwey-Overbeek (DVLO) theory, only taking into consideration the van der Waals forces as attractive and the electrostatic forces as repulsive, in many cases fails to fully explain the stability of liposomal suspensions. One example is the undulation force, which can cause repulsion between bilayers because of the confinement of thermal ripples as the liposomes approach each other [53]. Additional attractive forces must sometimes be introduced, such as hydrophobic attraction or ion-ion correlation, to account for aggregation of liposomes [54]. The main cause of the aggregation by the cationic AMPs seems to be the depletion of the electrostatic repulsion due to charge neutralisation of the liposomes, so the DVLO theory might lead to some insight after all. Because of the complexity of the interaction forces in liposomes that are not yet fully understood [54] [55], the following section should not be seen as an attempt at describing the interaction in our case, but rather as an illustration of concepts.

In general, curvature can be ignored in DVLO theory as long as the radius of the particle is much greater than the distance of interaction. The net interaction of two planar structures separated at a distance d in DLVO theory is given as [56]:

$$\Phi_{DLVO} = V_{\text{repulsive}}(d) + V_{\text{attractive}}(d) = \approx 64 k_B T n_\infty \kappa^{-1} \Upsilon_0^2 e^{-\kappa d} - \frac{A}{12\pi} \times d^{-2} \tag{10}$$

The first term of the equation signifies the contribution from the repulsive forces, and is mainly governed by the Debye screening length, $1/\kappa$. This is a measure of the range of the repulsive interaction, and it will vary with the electrolyte concentration of the solution, n_∞. Υ_0 describes the electrical potential of the surface. The second term in equation 10 accounts for the attractive van der Waals forces between two particles, and is characterised by the Hamaker constant A. The repulsive forces have an exponential decay with distance, while the van der Waals forces decreases squarely with an increase in distance. Noticeably, the van der Waals forces thereby have a different dependency on distance between macroscopic object (as d^{-2}) than between single atoms or molecules, where they depend on d as d^{-6}. The different forces are illustrated in Figure 12 **A)**. Typically there is a local maximum in net interaction energy, where distances that are closer than this maximum will lead to irreversible aggregation of the particles. To prevent the particles from aggregating, the maximum must exceed the kinetic energy of the system. When adding the cationic AMP to the bilayers the repulsive forces between the liposomes are expected to decrease, effectively

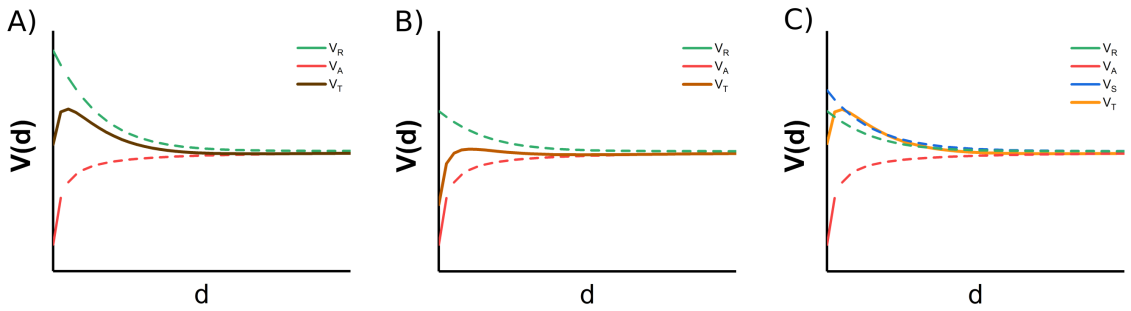

Figure 12: Steric stabilisation. (A) shows the normal case of stability in DVLO theory, with the contributions of the repulsive (V_R) and attractive forces (V_A) to the total potential (V_T). (B) shows what happens when the repulsive forces are weakened by for example adding the cationic peptide. (C) shows the effect of a steric stabiliser (V_S).

decreasing this maximum so that the liposomes can come into close contact and therefore aggregate (see Figure 12 **B)**). Increasing the electrostatic repulsion in this system would not help since any such attempt would be counteracted by the charge quenching of the AMPs. Another method of stabilization is therefore required.

Incorporating polymer chains at the surface of the liposomes creates a steric barrier for aggregation that is independent of electrostatics. This effect, termed steric stabilisation, is usually explained by one or both of the following principles [56][57][58]:

1. Volume restriction (Entropic effect): when two particles approach each other, the volume that the attached polymer chains can occupy is reduced, reducing the number of available conformations of the polymer and hence the entropy of the system.
2. Interpenetration effect (Enthalpic effect): the loss of bound solvent from the polymer chains as the particles approach each other, resulting in a positive change in enthalpy. This can also be interpreted as an increase of osmotic pressure as the two particles approach each other.

A number of factors that will affect the interaction potential of the polymer has to be considered, such as the solvent and concentrations, as well as whether the polymer is absorbed or grafted onto the particle. Grafting of polymers to the surface can be approximated to give the following contribution to the net interaction energy under certain conditions [56]:

$$\Phi_s(d) \approx 36 n_s k_B T e^{-\frac{d}{L}} \tag{11}$$

where L is the length that the polymer chain extends from the surface. This varies with a number of conditions as discussed in the next section (Section 2.3). As equation 11 shows, while the steric repulsion also has an exponential decay with distance, this decay is greatly reduced by the length of the attached polymer. This makes the steric repulsion more effective in stabilising the dispersion than sole electrostatic contributions. Steric stabilisation by grafting of polymers on the surface of the liposomes is therefore a good replacement for the weakened electrostatic repulsion term when interacting with cationic AMPs. Figure 12 **C)** illustrates the effect of adding steric stabilisation on the situation in 12 **B)**. The initial barrier against aggregation that was present in 12 **A)**) has been restored.

In contrast to the steric stabilisation provided by grafted and absorbed polymers, polymers in solution that are not attracted or repelled by the particle surface causes an destabilising attractive force between the colloids in solution. This is referred to as depletion forces, and is explained by an osmotic pressure arising from the difference in concentration of the polymer depleted region between the two surfaces and the polymer rich bulk solution. With the polymers being prevented from flowing between the surfaces to even out this difference, the two surfaces are forced together. As such, this can be interpreted as an osmotic force, but this time destabilising the colloids. The depletion force between two curved surfaces in a polymer solution can be expressed as a function of activity (effective concentration) a and radius of gyration R_g [59]:

$$F_c(d) = -\pi R R_g a k T \left(1 - \frac{d}{R_g}\right) \tag{12}$$

Equation 12 shows that the depletion force increases with increasing activity and size of the polymers. PEO has a very high activity, and are as such very good depletants [59].

2.3 Polymer conformation on interfaces

Tethering of polymers to surfaces involves attaching (grafting) the polymers to the surface by their ends. The polymer chain is therefore free to take up a number of conformations that depend on their surface coverage and the size of the polymer chain, as well as the solvent conditions. When the coverage is low compared to the polymers size ($1/n_s > R_g^2$), the chains will merely assume the same conformation as they have in their solvated form. In this case we can approximate L in expression 11 with the radius of gyration, R_g. Equation 11 then becomes [56]

$$\Phi_s(d) \approx 36 n_s k_B T e^{-\frac{d}{\alpha R_g}} \tag{13}$$

where α is an expansion coefficient that depends on the solvent conditions. $\alpha = 1$ is referred to as the theta conditions for the polymer, where the monomer-monomer interactions of the polymer are energetically equal to the monomer-solvent interaction. In such conditions, where the enthalpy of mixing is exactly zero, the polymer will have a complete random walk conformation. At $\alpha > 1$ the polymer is in good solvent conditions, meaning the interactions with the solvent are actually more favourable and the polymer will expand. $\alpha < 1$ means that the conditions are poor for the polymer and it will contract to avoid interaction with the solvent. Equation 13 thereby also shows the effect of the solvent conditions on the stabilization: the steric repulsion increases with better solvent conditions. Polymer layers with a low tethering density in a good solvent will therefore obtain a so-called mushroom conformation, while in a poor solvent the polymer chains will collapse [60] (see Figure 13 for illustration).

On the other hand, if the tethering density is high, chains will be crowded and so polymers with a long radius of gyration will tend to stretch out [61]. This means that L will be larger than R_g, and we will get an increased steric repulsion. This scenario is referred to as a brush conformation of the polymer layer (Figure 13). When going to these high tethering densities, the spacing between the polymer chains, s, is less than R_g. Given that the polymer is in a good solvent so that the chains do not easily become entangled, the thickness of the polymer layer, L, can be estimated by a scaling law based upon minimising the free energy per chain [62]:

$$L \approx \frac{(Nl)^{5/3}}{s^{2/3}} \tag{14}$$

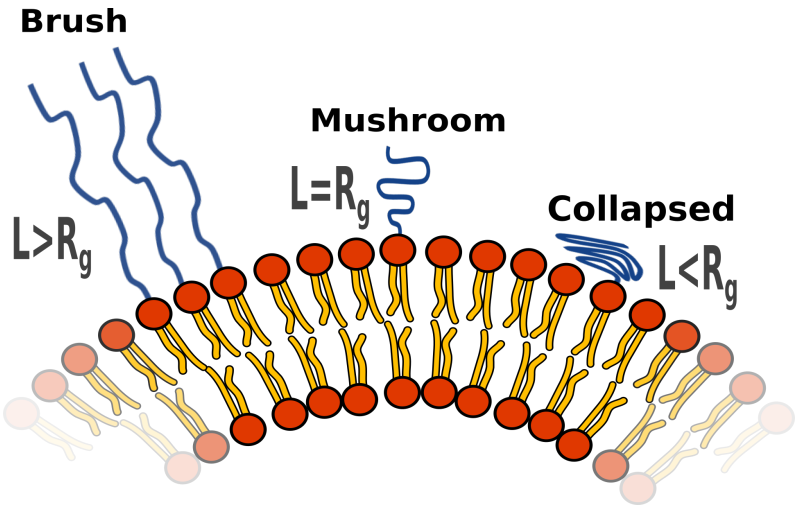

Figure 13: The different conformations of surface grafted polymers

where N is the number of monomers in the polymer and l is the length of each monomer segment (Nl then giving the full contour length of the polymer), while s is the distance between the tethered polymer chains on the surface. The equation shows that as s decreases, L will increase, making a thicker brush layer.

2.4 General scattering theory

Detailed information about scattering theory can be found in a number of textbooks [63][64][65][66][67]. In this section the most important concepts will be summarised.

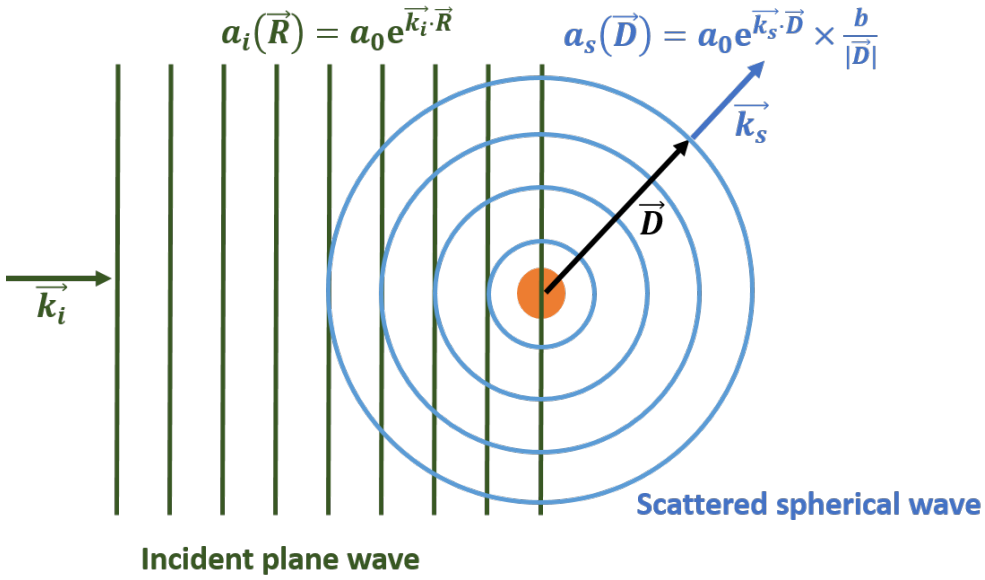

Figure 14: Depiction of a general scattering event.

A general scattering event is depicted in Figure 14. An incoming wave of some radiation interacts with a so-called scatterer which deflects the radiation from its original direction. For a scattering event to occur, the scatterer must therefore have an interaction potential with the incoming radiation. In the case of X-ray scattering, the scatterer is an electron and the interaction can be deduced from the electromagnetic interaction between the electron and photon (Thomson scattering). In neutron scattering the interaction is between the nucleus and neutrons and can be deduced from quantum mechanical considerations. Either way, if the kinetic energy of the incoming particle is much lower than this interaction potential, the potential can be seen as essentially stopping and creating an impenetrable wall for the radiation at certain distance from the scatterer. This distance is what is referred to at the scattering length, b, giving a measure of the strength of interaction between the radiation and scatterer. In classical terms it can be imagined as the radius of the scattering sphere that is seen by the incoming particle - larger b means a higher chance of scattering. With the necessary assumption as described above for a scattering length b, we can also describe a scattering cross section, σ as

$$\sigma = 4\pi b^2 \tag{15}$$

which is the area that the outgoing radiation constitutes. For electromagnetic radiation interacting with an electron the scattering length would be the classical electron radius, while for neutron radiation interacting with a nucleus the potential is caused by the nuclear force and so is determined by the characteristics of the scattering nucleus. For neutrons therefore, the scattering length can also be negative, caused by the difference in whether the potential is attractive or repulsive - this will affect how the phase of the incoming wave is shifted after scattering.

The incoming radiation is usually idealised as a monochromatic plane wave, for which the time-independent probability amplitude a_i at a position $\vec{R}$ would be described as:

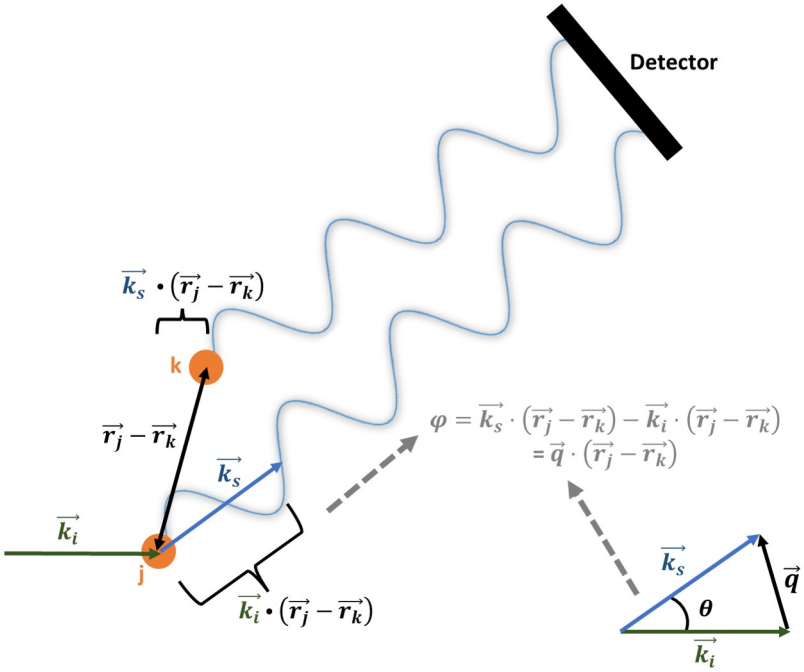

Figure 15: An illustration of the phase shift resulting from the scattering of two scatterers separated by a distance $\vec{r_j} - \vec{r_k}$.

$$a_i(\vec{R}) = a_0 e^{i\vec{k_i} \cdot \vec{R}} \tag{16}$$

where a_0 is the classical amplitude of a wave (height of the wave function), while k_i is the propagation vector of the plane wave with the magnitude

$$|\vec{k_i}| = \frac{2\pi}{\lambda} \tag{17}$$

With the above considerations, the scatterer being so small compared to the incoming wavelength that it can be considered a point-scatterer, the resulting scattering pattern will be that of a homogeneous spherical wave, so at a detector distance $\vec{D}$ the amplitude from the single scatterer can be described as:

$$a_s(\vec{D}) = a_0 e^{i\vec{k_s} \cdot \vec{D}} \times \frac{b}{|\vec{D}|} \tag{18}$$

Rather than having a single scatterer a realistic sample will always consist of many scatterers, so that the amplitude at distance D will be a sum of the amplitudes resulting from different scatterers. This means that not only the interaction between the incoming radiation and each individual scatterer have to be taken into account, but also the interaction between the scattered waves and the scatterers. Since the scattered field is usually small compared to the incident radiation, total interacting field at each scattering center can be approximated with the incident radiation field without much deviation from reality. This is called the Born approximation and is usually valid for X-rays and neutron experiments, but in light scattering only holds when the optical refractive indices of the scatterers do not differ too much from the surrounding medium [68]. For X-ray scattering, the probability that the incoming radiation will be absorbed is so much higher than the probability that it will scatter - the scattering cross-section, σ_s, is much lower than the absorption cross-section σ_a. For neutron radiation, the scattering cross-section itself is much smaller than for X-rays - figuratively, the nucleus as seen by the neutron radiation is much smaller than

the electron cloud seen by the X-rays. The approximation that each scattering event is independent of others therefore holds for these methods as long as reasonable experimental considerations are taken. This includes making sure that the path of the radiation through the sample is small enough to avoid the re-scattering of an already scattered wave. In the Born approximation, the scattered radiation at detector distance $\vec{D}$ will simply be the sum of the scattered amplitudes from individual scatterers caused by the incoming radiation. Due to the wavenature of the radiation, this sum will depend on the phase of the different amplitudes at distance D, and assuming that the scattering is elastic (no energy transfer between the particles) the phase difference depends only on the scatterers positioning relative one another. In this thesis using small-angle scattering, only elastic scattering is considered as this is what yields information about the structure of our sample, with inelastic scattering regarded as additional background in the measurement. Having two particles at positions r_j and r_k from an arbitrary origin, we see with a simple geometrical argument illustrated in Figure 15 that the phase difference (difference in path travelled) of the two scattered waves must be given by

$$\varphi = \vec{k_s} \cdot (\vec{r_j} - \vec{r_k}) - \vec{k_i} \cdot (\vec{r_j} - \vec{r_k}) = \vec{q} \cdot (\vec{r_j} - \vec{r_k}) \tag{19}$$

The vector $\vec{q}$ is usually representing the independent variable in scattering studies, and is defined as $\vec{q} = \vec{k_s} - \vec{k_i}$ with the resulting magnitude

$$|\vec{q}| = q = \frac{4\pi}{\lambda} \sin\theta \tag{20}$$

also easily deduced from geometrical arguments as shown in Figure 15. Given two scatterers at a distance, $(\vec{r_j} - \vec{r_k})$, from each other which both emit a spherical wave upon radiation, the detected amplitude at a distance $\vec{D}$ from the original scatterer will then be:

$$a_s(\vec{D}, \vec{q}) = a_0 e^{i\vec{k_s}\cdot\vec{D}} \times \frac{b_j}{|\vec{D}|} + \left[a_0 e^{i\vec{k_s}\cdot\vec{D}} \times \frac{b_k}{|\vec{D}|} \right] \cdot e^{-i\vec{q}\cdot(\vec{r_j} - \vec{r_k})} \tag{21}$$

where $e^{-i\vec{q}\cdot(\vec{r_j} - \vec{r_k})}$ corrects for the phase difference of the waves which gives rise to interference. This amplitude can be easily be generalized to n number of point scatterers by simply summing the amplitude contributions from all scatterers at the distance $\vec{D}$ while correcting for the phase difference:

$$A_s(\vec{D}, \vec{q}) = \sum_{j=1}^{n} a_i e^{-i\vec{q}\cdot\vec{r}} \tag{22}$$

where a_i corresponds to the amplitudes of the waves originating from scattering center i, while $\vec{r}$ is the distance from some arbitrary origin giving the relative phase shift of the amplitude. This can be recognised as a Fourier series, and therefore the scattering amplitude may simply be converted from this image of the Fourier transform of the positions, called reciprocal space, back into real space by performing a inverse Fourier transform.

What is detected from a scattering experiment however, is not the amplitude of the wave of scattered radiation, but its intensity:

$$I_s(\vec{q}) = < A_s(\vec{D}) \cdot A_s(\vec{D}) > = \frac{a_0^2}{D^2} \sum_{j,k=1}^{n} b_j b_k e^{-i\vec{q}\cdot\vec{r_{jk}}} \tag{23}$$

where $\vec{r_{jk}} = \vec{r_j} - \vec{r_k}$. The dependency on the vector $\vec{D}$ has disappeared as $e^{i\vec{k_s}\cdot\vec{D}} \times e^{-i\vec{k_s}\cdot\vec{D}} = 1$, and the intensity depends only on the scattering lengths of the scatterers and their relative locations. While

the intensity clearly gives the q-dependence of the squared amplitude, it does not contain information about the phases of the waves. This is what gives rise to the phase problem in diffraction. The term before the sum in equation 23 is merely an instrumental constant, while the second term is sample specific. This sum is what is usually identified with the differential scattering cross-section of the sample, and it has the units of an area. The differential scattering cross-section is defined as the flux of scattered radiation, $d\sigma$ into the solid-angle element $d\Omega = \sin\theta d\theta d\phi$. Normalization to sample volume gives the normal unit of inverse cm:

$$\frac{d\Sigma}{d\Omega}(\vec{q}) = \frac{1}{V} \cdot \frac{d\sigma}{d\Omega} = \frac{1}{V} \sum_{j,k=1}^{n} \left\langle b_j b_k e^{-i\vec{q}\cdot r\vec{_{jk}}} \right\rangle \tag{24}$$

For X-rays, as an atom is made up of several scattering units, each atom will still have their own characteristic scattering pattern dependent on their distribution of electrons, giving them a distinct atomic form factor. These atomic form factor can then easily be used to find the scattering from a structure made up of different atoms. For neutrons, although in their case the atomic form factor would simple equal the scattering length, these scattering lengths not only depend on the number of protons constituting the nucleus of the atom, but also on the number of neutrons (the isotope) as well as the spin state of the atom. This means that for one atom there is not one scattering length but rather a distribution of scattering lengths. We can account for this by modifying expression 24 to include this distribution. First taking the average of $b_j b_k$ over the different scattering lengths for one atom:

$$\langle b_j b_k \rangle = \begin{cases} \left\langle b^2 \right\rangle = \langle b \rangle^2 + \langle b - \langle b \rangle \rangle & \text{for } i = j \\ \\ \langle b \rangle^2 & \text{for } i \neq j \end{cases} \tag{25}$$

Splitting equation 24 into the sum of the $j = k$ and $j \neq k$ terms and inserting from 25 leads us to the following expression:

$$\frac{d\Sigma}{d\Omega}(\vec{q}) = \frac{1}{V_s}\langle b \rangle^2 \sum_{i,j=1}^{N} \rangle |e^{i\vec{q}\cdot\vec{r_i}}|^2 + \frac{N}{V_s}\left(\langle b^2 \rangle - \langle b \rangle^2\right) = \left(\frac{d\Sigma}{d\Omega}(\vec{q})\right)_{coherent} + \left(\frac{d\Sigma}{d\Omega}\right)_{incoherent} \tag{26}$$

The second part of equation 26 is independent of $\vec{q}$ and so will simply give us a flat background that is independent of the structure of our sample. This is called the incoherent scattering, while the first part which contains all the structural information is called the coherent scattering.

While the above description details how the scattering process can yield structural information about out sample, this is only one way of utilizing scattering normally referred to as static scattering because the recorded intensity is normalized over time. One can, however, also gain information about the dynamics of the system by recording the change in intensity over time, in time-resolved scattering experiments. Both static and dynamic techniques were used in this thesis, and their specifics are discussed in the next sections.

2.5 Basic concepts in small angle scattering

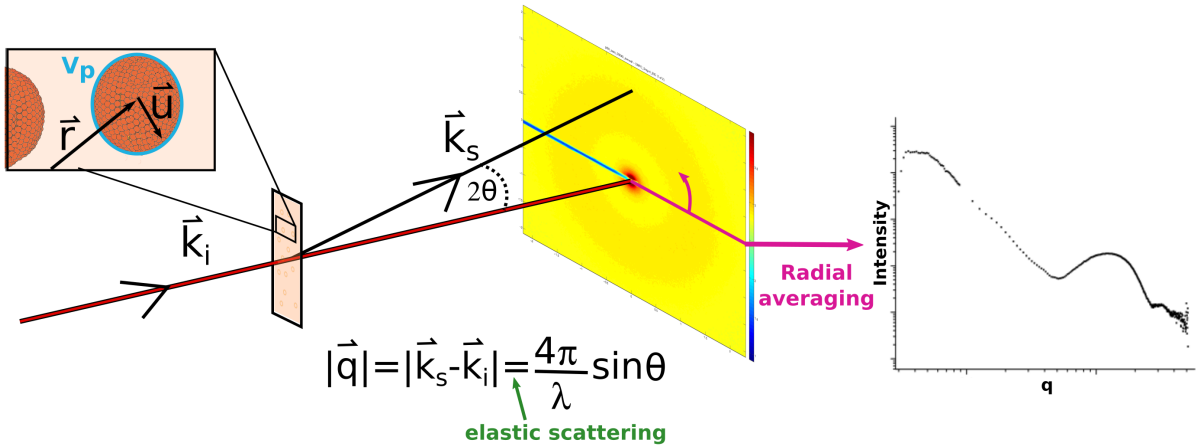

Figure 16: Illustration of a small angle scattering experiment.

Small angle scattering experiments are concerned with finding the structure of the material on a nanometre length scale. In this case, the structural length scale of interest is much larger than that of the wavelength of radiation. It is then convenient to define a scattering length density, ρ that gives the scattering power of a certain volume in the sample, for example that of a molecule.

$$\rho(\vec{u}) \equiv \frac{1}{V}\sum_i b_i \tag{27}$$

$\vec{u}$ in the above equation describes a distance within the particle as illustrated in Figure 16. If we have a particle of scattering density $\rho(\vec{u})$ in a surrounding medium with scattering length density of ρ_s, it is convenient to define an excess scattering length density as

$$\Delta\rho(\vec{u}) = \rho(\vec{u}) - \rho_s \tag{28}$$

Rewriting equation 24 of the previous section in terms of the scattering length density, the differential cross-section of one particle can now be written as

$$\frac{d\Sigma}{d\Omega}(\vec{q}) = \iint_{V_p} \Delta\rho(\vec{u})\Delta\rho(\vec{v})e^{-iq(\vec{u}-\vec{v})}d\vec{u}d\vec{v} \tag{29}$$

with V_p being the volume of the particle and $\vec{u}$ and $\vec{v}$ being distances within the particle. Extending this to N number of particles located at positions $\vec{r}$ from an arbitrary origin gives

$$\frac{d\Sigma}{d\Omega}(\vec{q}) = \frac{1}{V}\left(\sum_{i=1}^{N} e^{-i\vec{q}\cdot\vec{r_i}}\int_{V_p}\Delta\rho(\vec{u})e^{-i\vec{q}\cdot\vec{u}}d\vec{u}\right)\left(\sum_{j=1}^{N} e^{-i\vec{q}\cdot\vec{r_j}}\int_{V_p}\Delta\rho(\vec{v})e^{-i\vec{q}\cdot\vec{v}}d\vec{v}\right) \tag{30}$$

This expression is valid for all types of radiation, but with $\Delta\rho$ assuming a different identity. While for X-ray and neutron scattering $\Delta\rho$ signifies the difference in scattering lengths of the particle and surrounding medium, for light scattering it will be identified with the change in the dielectric constant of the particle from the surrounding medium.

In the special case of neutron scattering, it was already pointed out in Section 2.4 that neutrons scatter differently from different isotopes of an atom. This difference in scattering lengths of isotopes can be used for contrast variation experiments, opening up the possibility for isotope

substituting that can give us contrast where there was none before. The most prominent is the contrast between the scattering lengths of hydrogen (H) and deuterium (D); deuterium (^{2}H) has a positive scattering length of 0.677×10^{-12} cm while protium (^{1}H) has a negative scattering length of -0.374×10^{-12} cm [69]. The use of isotope substitution in neutron scattering has many applications. Deuterium substitution could yield information about the locations of hydrogen which is an inaccessible quantity with X-rays. By varying the relative amounts of H_2O and D_2O in the solvent we can vary $\Delta\rho$ for different components in our particle, making it possible to study the scattering from one component at a time. The H/D contrast difference can also be used to study dynamics, such as the mixing of a deuteriated and hydrogenated compounds or, as it is used in this thesis, the transport of solvent across vesicles prepared in one solvent (H or D) and then mixed with the other solvent before measurement.

The terms in $\Delta\rho$ that control the intensity in equation 29 show a periodicity of $(\vec{u} - \vec{v}) = \frac{2\pi}{q}$. If this periodicity is on a large scale it means that it can be detected at low q [70]. Simplified, large distances in real space corresponds to small distances in reciprocal space, q. In small angle scattering one takes advantage of this feature to study the larger structures in real space by detecting the scattering intensity at very low angles, so at very small q-values. This can give information on the size, shape and interaction between mesoscopic particles rather that just the interatomic distances in the material. Rearranging the general expression for the scattering cross-section in equation 30 gives

$$\frac{d\Sigma}{d\Omega}(\vec{q}) = \frac{N}{V}\left\langle \left(\iint_{V_p} \Delta\rho(\vec{u})\Delta\rho(\vec{v}) e^{-i\vec{q}\cdot(\vec{u}-\vec{v})} d\vec{u}d\vec{v} \right) \left(\frac{1}{N}\sum_{i=1}^{N}\sum_{j=1}^{N} e^{i\vec{q}\cdot(\vec{r_j}-\vec{r_i})} \right) \right\rangle \tag{31}$$

Since the systems studied in this thesis are in solution, an average over all possible positions and orientations of the particle, denoted by the angle brackets, has been included. If the system is isotropic, this also reduces the equation from being dependent on $\vec{q}$ to only being dependent on the magnitude, $|\vec{q}| = q$, giving us circular symmetry around $q = 0$ in our detected scattering pattern (see Figure 16).

The integral of equation 31 describes the scattering from a single particle, while the double sum describes the scattering due any structure arising from interactions between particles.

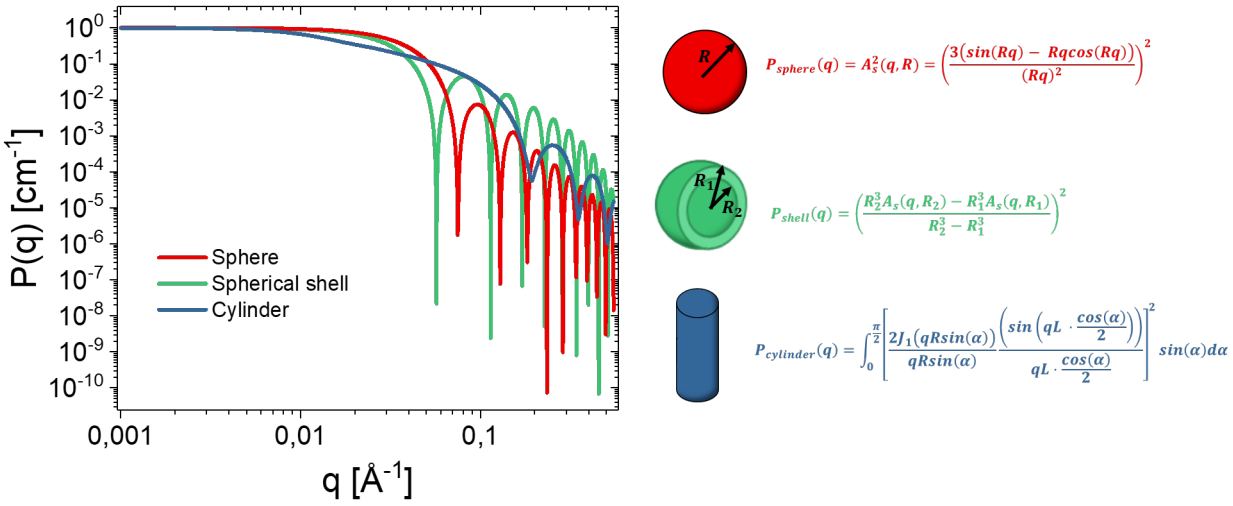

Figure 17: Examples of form factors of simple geometrical objects. Expressions can be found in reference [52]

At this point, for a particle of uniform density $\Delta\rho$, equation 31 is usually written as

$$\frac{d\Sigma}{d\Omega}(q) = \frac{N}{V}\langle\Delta\rho\rangle^2 V_p^2 P(q)S(q) \tag{32}$$

where $P(q)$ is called the form factor and contains the information on the size and form of the particle. $P(q)$ is derived by doing the integration in equation 31 over the form of the particle.

$$P(q) = \iint_{V_p} e^{-i\vec{q}\cdot(\vec{u}-\vec{v})} d\vec{u}d\vec{v} \tag{33}$$

Some examples of form factors for simple geometrical objects can be seen in Figure 17. $S(q)$ is the structure factor of the system, describes the interference due to scattering from different particles:

$$S(q) = \frac{1}{N}\sum_{i=1}^{N}\sum_{j=1}^{N} e^{i\vec{q}\cdot(\vec{r_j}-\vec{r_i})} \tag{34}$$

The structure factor is closely linked to the interaction potential between particles, which can be estimated using various approximations in liquid state theory [71]. If it is known that the form factor does not depend on concentration, one can also determine experimental structure factors by dividing the obtained scattering by the form factor and the known experimental parameters in equation 32. $S(q) \to 1$ as the concentration goes to zero. This also means that in cases where the measurements are performed in the very dilute regime, as is the case in the systems studied in this thesis, the structure factor is assumed to be one so that the scattering is only dependent on the contrast and the form factor.

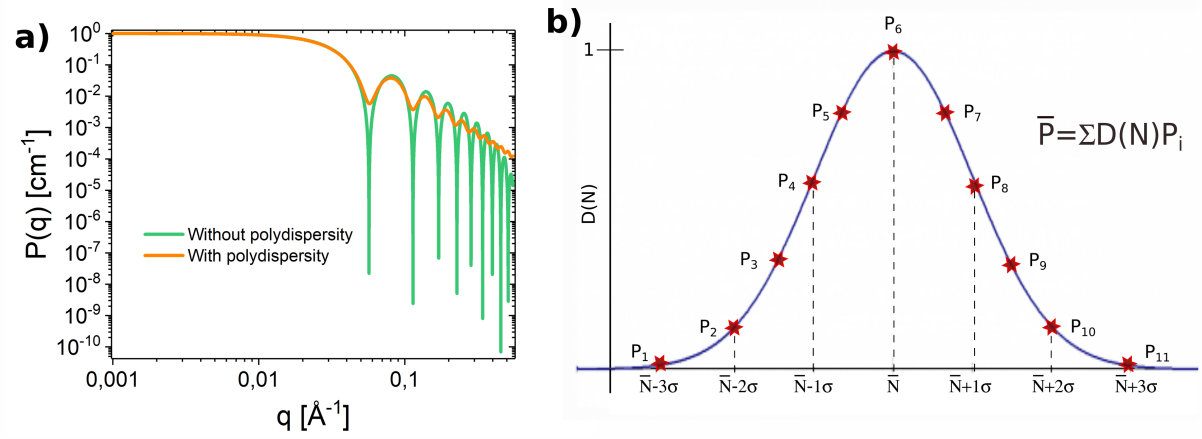

Figure 18: a) Example of the effect of polydispersity on the spherical shell form factor. b) Illustration of the numerical integration over a distribution function to account for polydispersity.

Another factor which affects the scattering pattern is the polydispersity of the sample, which is a measure of the distribution of sizes in the particle solution. A monodisperse solution consists of particles all having the same size and will have a form factor as shown in Figure 17. A polydisperse sample will however have a range of different sized particles. In this case, their form factor will be smeared out, as can be seen an example of in Figure 18 **a)**, because the scattering at any q is not determined by a single form factor, but by an average of the form factors of the differing particles. Polydispersity can be accounted for in the form factor by integrating it over a normalized size distribution, $D(N)$ [72]:

$$\bar{P(q)} = \int D(N)P(q,N)dN \tag{35}$$

where N described the property for which the particles differ, such as radius or length. The integration is usually done numerically, but can in some rare cases be done analytically if an analytical solution to the integral exists. The numerical process is illustrated for one q-value in Figure 18 **b)**. Here $D(N)$ is a Gaussian distribution, but the same process holds for any distribution that the particles might have. A certain number of points (11 in Figure 18) are selected on the curve and the form factor is calculated for the chosen Ns and multiplied by $D(N)$. The different form factors are then summed together to give the average value for the polydisperse form factor at that q. This has to be done for all q-values. If structure factor contributions are present, the effect of polydispersity becomes more difficult to calculate as the interaction between particles will likely depend on their differing properties but may still be approximated with a monodisperse structure factor in certain cases [72].

Although one can analyse the detected scattering from small angle scattering by doing an inverse Fourier transformation as is usually done in wide angle scattering to obtain the interatomic distances, another approach in small angle scattering studies is to analyse by direct modelling. This consists of an iterative process where an analytical model for the presumed system is compared with the experimental data. If the model cannot be fitted to the data with the variable parameters, changes to the analytical model must be made, and this process is continued until an appropriate model is found. The models that were used as a basis for the analytical models developed in this thesis are described in Sections 2.6.1 -2.6.3.

2.6 Analytical models for small angle scattering

2.6.1 Scattering model for block co-polymer micelles

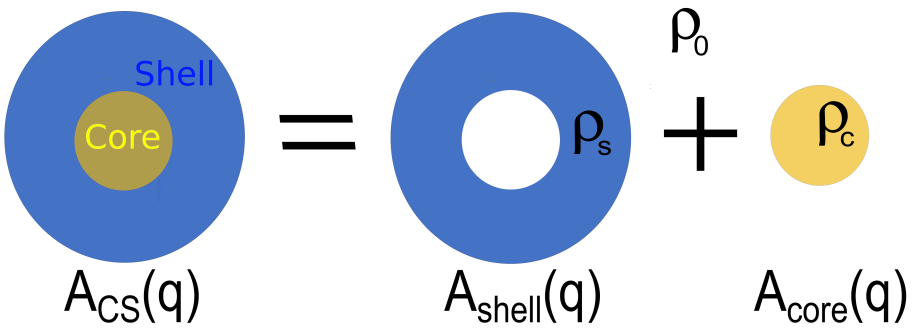

Figure 19: Illustration of how the scattering from a core-shell structure is modelled

Small angle scattering from micelles can be modelled as scattering from a core-shell structure, where the interior hydrophobic parts constitute the core with a scattering density ρ_c and the exterior hydrophilic part form a surrounding shell with a scattering density ρ_s (illustrated in Figure 19) [52]. The resulting scattering amplitude will then be the superposition of the scattering amplitudes from the individual components, core and shell, yielding

$$A_{CS}(q) = (\rho_c - \rho_0) \times V_c \times A_c(q, R_{\text{core}}) + (\rho_s - \rho_0) \times V_s \times A_s(q, R_{\text{outer}}) \tag{36}$$

where V_i and ρ_i are the volumes and scattering length densities of the core-forming ($i = c$) and shell-forming ($i = s$) blocks, ρ_0 is the scattering length density of the solvent, and $A_i(Q)$ is the scattering amplitudes for sphere and shell structures. These may be the amplitudes corresponding the spherical and shell form factors listed in Figure 17 for simple surfactant micelles with a dense shell structure.

In the case of polymeric micelles, however, the shell will not consist of a dense layer of the hydrophilic part, but rather of a diffuse corona of polymers. The internal structure of the polymers should be taken into account, as there will be local contrast between the polymer structure and the solvent. A so-called blob scattering, F_{blob} is therefore added to the core-shell scattering arising from the short ranged chain-chain interactions scattering between the polymer chains. Because the polymer chains also exhibit excluded volume effects that are significant (due to chain-chain interactions), an expression based on Monte Carlo simulations from Pedersen et al. [73] gives a

better description of the scattering from block copolymer micelles then equation 36 [52]:

$$I_{CS}(q) = \frac{\phi}{P_{\text{agg}} V_{cs}} \left(\Delta\rho_c^2 \cdot P^2 V_c^2 \cdot A_c(q)^2 + \Delta\rho_s \cdot P_{\text{agg}}^2 (P_{\text{agg}} - F_{blob}(0)) V_s \cdot A_s(q)^2 + 2\Delta\rho_c \Delta\rho_s \right. \\ \left. \cdot P_{\text{agg}}^2 V_s V_c \cdot A_c(q) A_s(q) + \Delta\rho_s V_s^2 \cdot F_{blob}(q) \right) \tag{37}$$

where ϕ is the volume fraction of the polymer ($\phi = c/(d_{sol})$), $V_{cs} = V_c + V_s$ is the total volume of the block co-polymer, P_{agg} is the aggregation number while $\Delta\rho_i$ constitutes the difference in scattering length density of core or shell component from solvent.

For the core, being assumed to be a homogeneous sphere, the resulting expression will simply be [52]

$$A_c(q) = \frac{3\left(sin(q \cdot R_c) - q \cdot R_c cos(q \cdot R_c)\right)}{(q \cdot R_c)^3} \cdot e^{\frac{-q^2\sigma_{int}^2}{2}} \tag{38}$$

while for the shell, consisting of a distribution of polymer chains, a Fourier transform must be done over the specific density profile, $n(r)$ of the shell:

$$A_{sh}(q) = \int_{R_c}^{\infty} 4\pi n(r) \frac{\sin(qR)}{qR} dr \cdot e^{\frac{-q^2\sigma_{int}^2}{2}} \tag{39}$$

with

$$n(r) = \frac{1}{C} \frac{r^{-x}}{1 + e^{\frac{r - R_m}{\sigma_m R_m}}} \tag{40}$$

where x is a scaling exponent to account for excluded volume effects as mentioned in Section 2.1.3. It is equal to 4/3 for star-like micelles [74]. $1/C$ normalises the density profile to the volume. R_m constitutes the overall micellar radius, while σ_m is the width of the corona smearing. The last term in the scattering amplitudes of both core and shell, $\exp(-q^2\sigma_{int}^2/2)$, is called the Debye-Waller factor [75]. This is included because the boundary between core and shell as well as between the shell and solvent are not realistically perfectly sharp, and the Debye-Waller factor makes the distribution profiles more smeared by convoluting the core density profile with a Gaussian of standard deviation of σ_{int}. The Debye-Waller factor is the term originally used for the correction for thermal fluctuations in scattering, but the factor also accounts for spatial fluctuations at the interfaces.

The blob scattering contribution is effectively modelled as

$$F_{blob}(q) = \frac{P(q)_{chain}}{1 + \hat{v} \cdot P_{chain}(q)} \tag{41}$$

where $\hat{v}$ is defined as the density of scattering sites times the Fourier transform of the direct correlation function between sites on different chains, therefore related to the amount of excluded volume and scales with the effective concentration of polymer[76]. The PEO chain scattering, $P_{chain}(q)$ can be approximated by an empirical expression from Beaucage:

$$P_{chain}(q) = e^{\frac{(-q^2 R_g^2)}{3}} + (\frac{d_f}{R_g^{d_f}})\Gamma(\frac{d_f}{2}) \left(\frac{\text{erf}(qkR_g)/\sqrt{6}^3}{q} \right)^{d_f} \tag{42}$$

where d_f is the so-called fractal dimension of the polymer chains, R_g is the radius of gyration of the free chain and $k = 1.06$ [77][52].

In dilute solution, where the structure factor effects are small, $S(q)$ can be approximated by a virial expansion of equation 34, yielding [78]

$$S(q) = \frac{\phi}{F(q \to 0)} \approx \left(\frac{1}{P(q \to 0)} \right) \left(\frac{1}{V_m} + 2A_2\Phi \right) \tag{43}$$

where the interparticle interferences are expressed by a second virial coefficient A_2. This procedure is called the Zimm approximation.

Polydispersity was not included in the model for the micelles as it was not found to be necessary to describe the scattering data.

2.6.2 Scattering model of lipid bilayers and liposomes

The simplest way of modelling a liposome is by assuming it is a homogeneous shell structure with a scattering length density equal to that of the lipid forming the membrane

$$\rho_{\text{lipid}} = \frac{\sum_i b_i}{V_{\text{lipid}}} \tag{44}$$

where i signifies each individual atom in the lipid molecule. In this case, assuming a dilute solution so that no structure factor comes into play, one can simply use the form factor for a spherical shell as given in Figure 17 to calculate the scattered intensity:

$$\frac{d\Sigma}{d\Omega}(q) = \frac{N}{V}\Delta\rho^2_{\text{lipid}} V_p^2 P_{\text{shell}} \tag{45}$$

This relatively simple model works reasonably well for neutron scattering when most of the contrast is between the protonated hydrocarbon chains in deuterated solvent, with a gradient increase in scattering length density across the polar head groups.

In terms of electron density, however, the phospholipid bilayer is a layered structure where the phosphate in the head groups have a higher electron density than both the surrounding water and the hydrocarbon chains. In this case it is better to model the liposomes with several concentric shells of individual scattering lengths densities, evoking more complex models as the interference terms between the shells must be taken into account.

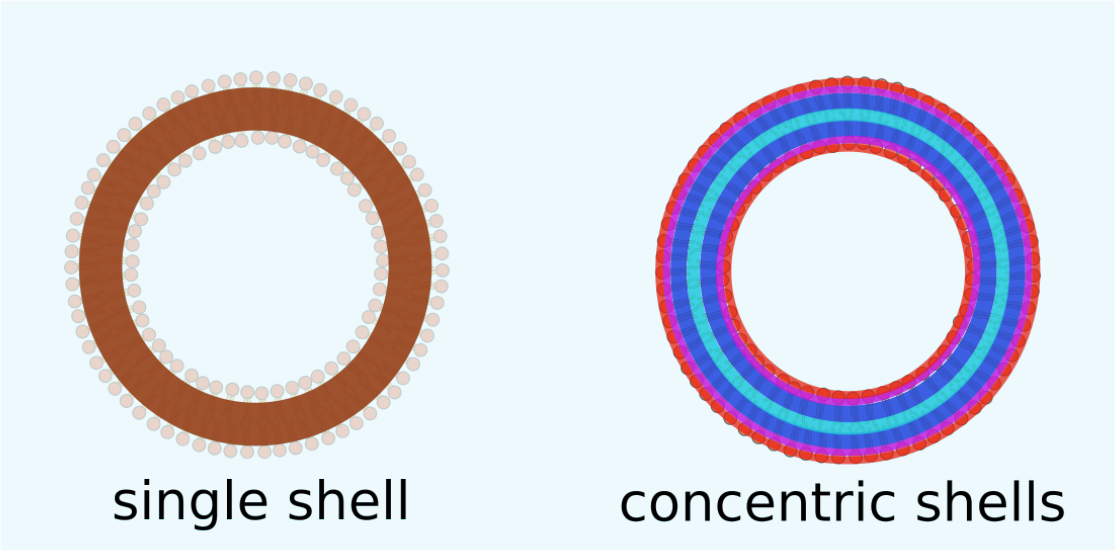

Figure 20: Illustration of two different ways of modelling a liposome. Different colors represent different scattering length densities.

For this thesis, the bilayer itself has been modelled by partitioning it into distinct segments of different scattering length densities. This partitioning can certainly be done in different manners,

often chosen differently for X-rays or neutrons due to the difference in the electron and neutron scattering length density profiles (ED and NSLD profiles, respectively). The model used in this thesis is based on the partitioning from Kučerka et al. [79] who used molecular dynamics simulations to parse the lipid molecule into components that were meaningful in terms of both the ED and NSLD profiles. The partitioning is illustrated in Figure 21. It is based on the volume probability, P_i profiles of the components, as can be seen in the graph in Figure 21, which describes the probability of finding the component at any point z traversing the bilayer. Such a distribution can easily be converted to ED/NLSD profiles as this merely consists of scaling the different scattering length densities with their respective volume probability at all positions z [80]:

$$\Delta\rho(z) = \sum_{n}^{i} (\rho_i - \rho_w)\, P_i(z) \tag{46}$$

As can be seen from the illustration in Figure 21, the probability distributions, with the exception of the methylene groups, are modelled as Gaussian functions:

$$P_i(z) = \frac{c_i}{(2\pi)^{1/2}} \exp\left[-\frac{(z-z_i)^2}{2\sigma_i^2}\right] \tag{47}$$

c_i scales the Gaussians by the volumes to have a maximum probability equal to

$$c_i = \frac{n_i V_i}{A\sigma_i} \tag{48}$$

where $n_i V_i$ is the volume of that specific part of the molecule, while A is the lipid area. The whole hydrocarbon region, CH, is modelled as a half-period squared sine/cosine function in accordance with the model by Eicher et al. [22]:

$$P_{HC} = \begin{cases} \sin\left(\frac{z - z_{\mathrm{HC_{inner}}} + \sigma_{\mathrm{HC}}}{2\sigma_{\mathrm{HC}}} \frac{\pi}{2}\right) & \text{if } z_{\mathrm{HC_{inner}}} - \sigma_{\mathrm{HC}} \leq z \leq z_{\mathrm{HC_{inner}}} + \sigma_{\mathrm{HC}} \\ 1 & \text{if } z_{\mathrm{HC_{inner}}} + \sigma_{\mathrm{HC}} \leq z \leq z_{\mathrm{HC_{outer}}} - \sigma_{\mathrm{HC}} \\ \cos\left(\frac{z - z_{\mathrm{HC_{outer}}} + \sigma_{\mathrm{HC}}}{2\sigma_{\mathrm{HC}}} \frac{\pi}{2}\right) & \text{if } z_{\mathrm{HC_{outer}}} - \sigma_{\mathrm{HC}} \leq z \leq z_{\mathrm{HC_{outer}}} + \sigma_{\mathrm{HC}} \end{cases} \tag{49}$$

where $z_{\mathrm{HC_{outer/inner}}}$ is the z-position of the 0.5-probability value of the hydrocarbon region, and $z_{\mathrm{HC_{inner}}} = -z_{\mathrm{HC_{outer}}}$ in the symmetrical model. The probability distribution of the methylene groups is then defined as

$$P_{\mathrm{CH_2}} = P_{\mathrm{HC}} - P_{\mathrm{CH_3}} \tag{50}$$

Finally, the solvent volume probability distribution is defined as the excess probability [79] [22]:

$$P_w(z) = 1 - \sum_i P_i(z) \tag{51}$$

From the subsequent scattering density length profiles calculated according to equation 46, the form factor is easily obtained by simply doing a Fourier transform:

$$F_b(q) = \left[2\int_0^{D/2} \Delta\rho(z) cos(qz) dz\right]^2 \tag{52}$$

where $D/2$ is a point beyond which $\Delta\rho$ becomes zero. The model in equation 52 assumes a symmetric bilayer, and so followingly the imaginary parts of the Fourier transform of the inner leaflet and outer leaflet will cancel eachother out ($sin(iqz) - sin(-iqz) = 0$), while the real part will add, giving the factor of 2 ($cos(qz) - cos(-qz) = 2cos(qz)$). The possibility to account for asymmetry in

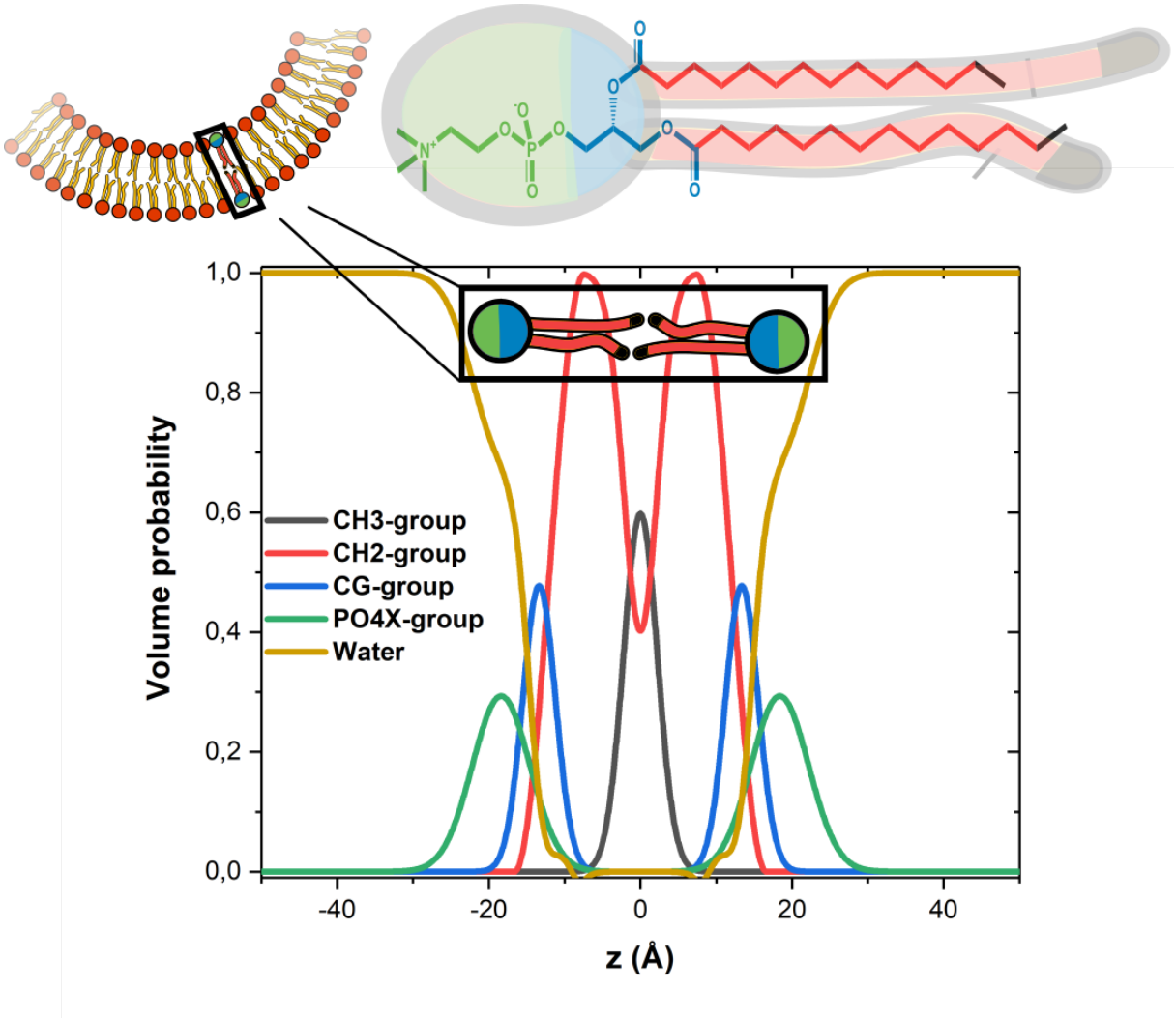

Figure 21: Illustration of how the bilayer is partitioned by the volume probabilities of the different phospholipid components.

was also incorporated into the model. Differences in the lipid distributions of the inner and outer leaflet should not be observed for the pure liposomes [81], but it was expected to become of great importance in the modelling with additives such as PEO or peptide. In the asymmetric model, based on the expression of Kučerka et al. in reference [81], the number of partitioned groups is almost doubled, except for that the end-methyl group is assumed to still be a single Gaussian. The asymmetry means that the sin terms in the calculation of $F(q)$ will not be cancelled and we will therefore have to include them in our calculations:

$$F_b(q) = \left[\int_{-D/2}^{D/2} \Delta\rho(z) cos(qz) dz\right]^2 + \left[\int_{-D/2}^{D/2} \Delta\rho(z) sin(iqz) dz\right]^2 \tag{53}$$

Additionally, one needs to account for the sphericity of the liposomes; this can be done by simply multiplying $F(q)^2$ above with the form factor of an infinitely thin sphere of radius R:

$$F_s = \left[4\pi \frac{R^2}{qR} sin(qR)\right]^2 \tag{54}$$

This approximation, called the method of separated form factors, can only be used as long as the bilayer thickness is much smaller than the radius of the liposomes [20]. It was found to hold for ULVs where the length scale of the vesicles was ≈ 10 times that of the bilayer [82]. R in equation 54 is defined from the centre of the liposome to $z = 0$, that is, to the middle of the bilayer.

The full expression for the macroscopic scattering cross-section can now be written as

$$\frac{d\Sigma}{d\Omega}(q) = nF_s(q, R)F_b(q, D) \tag{55}$$

where n is the number of scattering units, which is determined by the volume fraction ϕ and the aggregation number of the liposomes:

$$n = \frac{\phi}{P_{\text{agg}} V_{\text{lipid}}} \tag{56}$$

with

$$P_{\text{agg}} = \frac{4\pi(R + D_c)^3 - 4\pi(R - D_c)^3}{3V_c} \tag{57}$$

2.6.3 Scattering model for liposomes stabilised by polymer brushes

The model for scattering from liposomes with surface-grafted PEO used in this thesis is based on the approach from Arleth and Vermehren [83]. They used a simple spherical shell form factor describing the liposome where the PEO-chains are attached to, as was described in the very beginning of Section 2.6.2. In this work, however, their expressions for the PEO-scattering have been combined with the more complex model for liposomes presented in Section 2.6.2. While it is assumed that the PEGylated lipids are partitioned equally within the inner and outer leaflet in the article in the article, this is not necessarily true. Considering the limited space within the liposome it could be hypothesised that the PEO might preferably be in the outer leaflet of the liposomes. The model in this thesis allows for this to be varied by including a f_{inner} parameter that is set to the fraction of PEO in the inner leaflet. The total scattering intensity is split up into the following terms, illustrated in Figure **??**:

$$I_{\text{PEO-liposome}}(q) = I_{\text{ss}}(q) + I_{\text{chain}}(q) + I_{c_i c_i}(q) + I_{c_o c_o}(q) + I_{sc_i}(q) + I_{sc_o}(q) + I_{\text{chain}(q)} + I_{c_i c_o}(q) \tag{58}$$

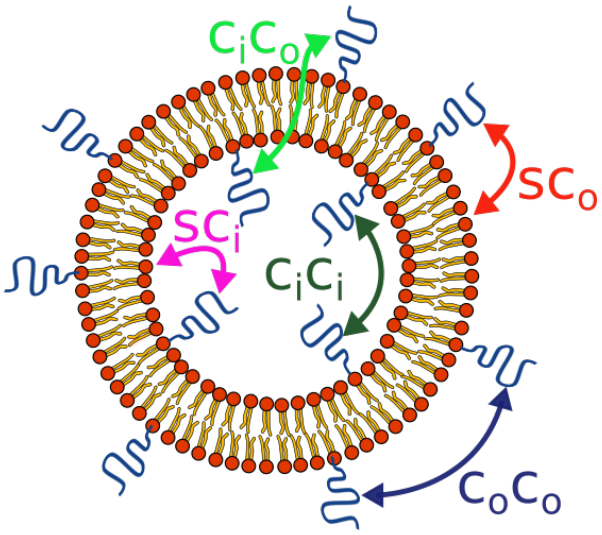

Figure 22: Illustration of the different interference terms in the model for the PEGylated liposomes.

where I_{ss} is identified with the scattering from the liposomal bilayer itself - found in equation 55. I_{chain} is the scattering from the PEO-chains alone, given by

$$I_{\text{chain}}(q) = n\Delta\rho_{PEO}^2 V_{PEO}^2 N_{PEO} \times 2\frac{e^{-(qR_g)^2} - 1 + (qR_g)^2}{(qR_g)^4} \tag{59}$$

where f_{PEO} is the fraction of PEO-modified lipids in the liposomes, V_{PEO} is their volume and N_{PEO} is defined as the number of PEO-chains per liposomes:

$$N_{\text{PEO}} = f_{\text{PEO}} \times P_{agg} \tag{60}$$

The next terms $I_{c_ic_i}$ and $I_{c_oc_o}$ are the intra-interference terms of the inner and outer PEO-chains, respectively, while the last term $I_{c_ic_o}$ describes the interference between the inner and outer chains:

$$\begin{aligned} I_{c_ic_i}(q) = n\Delta\rho_{PEO}^2 V_{PEO}^2 N_{PEO} f_{\text{inner}} \times (N_{PEO} f_{\text{inner}} - 1) \\ \times \left\{\frac{1 - \exp\left[-(qR_g)^2\right]}{(qR_g)^2}\right\}^2 \times \left\{\frac{\sin\left[q(R_{inner} - R_g)\right]}{q(R_{inner} - R_g)}\right\}^2 \end{aligned} \tag{61}$$

$$\begin{aligned} I_{c_oc_o(q)} = n\Delta\rho_{PEO}^2 V_{PEO}^2 N_{PEO}(1 - f_{\text{inner}}) \times [N_{PEO}(1 - f_{\text{inner}}) - 1] \\ \times \left\{\frac{1 - \exp\left[-(qR_g)^2\right]}{(qR_g)^2}\right\}^2 \times \left\{\frac{\sin\left[q(R_{outer} + R_g)\right]}{q(R_{outer} + R_g)}\right\}^2 \end{aligned} \tag{62}$$

$$\begin{aligned} I_{c_ic_o}(q) = n\Delta\rho_{PEO}^2 V_{PEO}^2 \times 2N_{PEO}^2 f_{\text{inner}} \times (1 - f_{\text{inner}}) \times \left\{\frac{1 - \exp\left[-(qR_g)^2\right]}{(qR_g)^2}\right\}^2 \\ \times \left\{\frac{\sin\left[q(R_{inner} - R_g)\right]}{q(R_{inner} - R_g)}\right\} \times \left\{\frac{\sin\left[q(R_{outer} + R_g)\right]}{q(R_{outer} + R_g)}\right\} \end{aligned} \tag{63}$$

The last remaining terms are the interference cross-terms of the outer and inner chains with the bilayer:

$$\begin{aligned} I_{sc_o}(q) = nA_bA_s \times \Delta\rho_{PEO} V_{PEO} \times 2N_{PEO} f_{\text{inner}} \times [N_{PEO} f_{\text{inner}} - 1] \\ \times \left\{\frac{1 - \exp\left[-(qR_g)^2\right]}{(qR_g)^2}\right\} \times \left\{\frac{\sin\left[q(R_{outer} + R_g)\right]}{q(R_{outer} + R_g)}\right\} \end{aligned} \tag{64}$$

$$I_{sc_i}(q) = nA_bA_s \times \Delta\rho_{PEO}V_{PEO} \times 2N_{PEO}(1 - f_{\text{inner}}) \times [N_{PEO}(1 - f_{\text{inner}}) - 1] \times \left\{ \frac{1 - \exp\left[-(qR_g)^2\right]}{(qR_g)^2} \right\} \times \left\{ \frac{\sin\left[q(R_{inner} - R_g)\right]}{q(R_{inner} - R_g)} \right\} \tag{65}$$

where A_b and A_s are the scattering amplitudes corresponding to scattering form factor in equation 53 for the bilayer and equation 54, respectively.

2.7 Dynamic light scattering

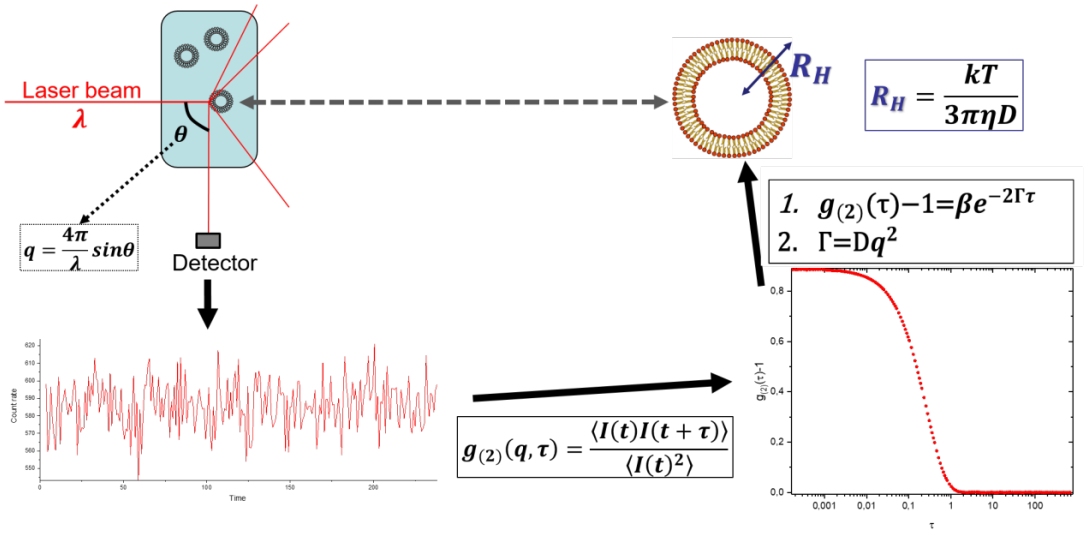

Figure 23: Illustration of the DLS technique.

Dynamic light scattering (DLS) is an effective technique for obtaining the hydrodynamic radius of particles in solution. This hydrodynamic radius corresponds to the radius of a sphere that has the same diffusion rate as the particle. The technique, illustrated in Figure 23, is based upon the fluctuations of the scattering intensity of a coherent laser beam from particles that are free to diffuse in solution. As a particle passes the laser beam it will scatter the light, causing an increase in scattered intensity at an angle θ, and this increased intensity will be maintained until the particle has diffused past the beam. DLS is therefore a method for measuring the motion of scattering particles. The scattered beam is detected at an angle, defined by the q-vector as described in Section 2.4 (equation 20). The resulting plot of the monitored intensity vs. time can look like the left graph in Figure 23. By correlating the intensity at different times t, a so called autocorrelation function is defined as

$$g_{(2)}(q,\tau) = \frac{\langle I(t)I(t+\tau)\rangle}{\langle I(t)\rangle^2} \tag{66}$$

where τ is the time over which the correlation is done. This autocorrelation function may look like the right graph in Figure 23, where the normalised $g_{(2)}(q,\tau) - 1$ has been plotted. At very small correlation times τ, the intensity is not expected to change much for most times t, so from equation 66 one gets that $g_{(2)}(\tau = 0) = \langle I(t)^2\rangle / \langle I(t)\rangle^2$. For very long correlation times, that extend above the time it takes for the particles to diffuse past the laser beam, it is expected that $\langle I(t+\tau)I(t)\rangle = \langle I(t)\rangle$ so that $g_{(2)}(q,\tau) = 1$, or $g_{(2)}(q,\tau)-1 = 0$ as in the graph in 23, corresponding to no correlation. Somewhere in between these extremes there will be a decay of the correlation that describes the time interval in which the particles are actually moving in the way of the laser beam [84]. This diffusion time depends on the particle's size; larger particles will diffuse slower than smaller particles. For spherical particles such as liposomes, the Stokes-Einstein equation relates the diffusion coefficient, D with the particle's radius of hydration, R_H [85]:

$$D = \frac{k_B T}{8\pi\eta R_H^3} \tag{67}$$

Precise knowledge of the temperature, T as well as the viscosity η of the solvent is therefore required for determination of R_H. To connect the diffusion coefficient with the correlation function above,

the Siegert relation is used: [86]

$$g_2(q,\tau) = 1 + C|g_1(q,\tau)|^2 \tag{68}$$

where C is a coherence factor that accounts for the beam not being perfectly coherent. Theoretically, for a monodisperse solution, $|g_1(q,\tau)|$ is a single exponential

$$g_1(q,\tau)| = e^{-\Gamma_c \tau} \tag{69}$$

with Γ_c (labelled with c to distinguish it from the Gamma-function $\Gamma(x)$) denoting the decay rate being equal to

$$\Gamma_c = Dq^2 \tag{70}$$

Experimentally, however, it is found that the data on particle diffusion is better explained by an intensity weighted integral over a distribution of decay rates $G(\Gamma_c)$ [87]:

$$g_1(\tau) = \int_0^\infty G(\Gamma_c) \exp^{-\Gamma_c \tau} \, d\Gamma_c \tag{71}$$

Instead of using equation 69, a stretched exponential that accounts for the distribution is used to describe the data:

$$g_1(\tau) = e^{-(\tau/\tau_c)^\beta} \tag{72}$$

β accounts for the stretching of the exponential and its value will therefore tell us about the extent of deviation from the ideal case in equation 69. τ_c denotes a characteristic relaxation time. If β is equal to one, $\tau_c = 1/\Gamma_c$, and equation 72 would be equal to 69. Otherwise, the mean of the relaxation times, $\langle \tau_c \rangle$, is taken as the integral of the stretched exponential which can be solved analytically as

$$\langle \tau_c \rangle = \left[\frac{\tau_c}{\beta} \times \Gamma\left(\frac{1}{\beta}\right) \right] \tag{73}$$

The diffusion coefficient can then again be found by using $1/\langle \tau_c \rangle$ for Γ_c in equation 70:

$$\Gamma_c = Dq^2 = \left[\frac{\tau_c}{\beta} \times \Gamma\left(\frac{1}{\beta}\right) \right]^{-1} \tag{74}$$

DLS therefore provides a useful way of assessing the global structure of particles in the nanometre range.

3 Experimental section

A full list of materials and equipment used in this thesis can be found in the appendix (section 6.1).

3.1 Liposome preparation

3.1.1 Liposome protocol

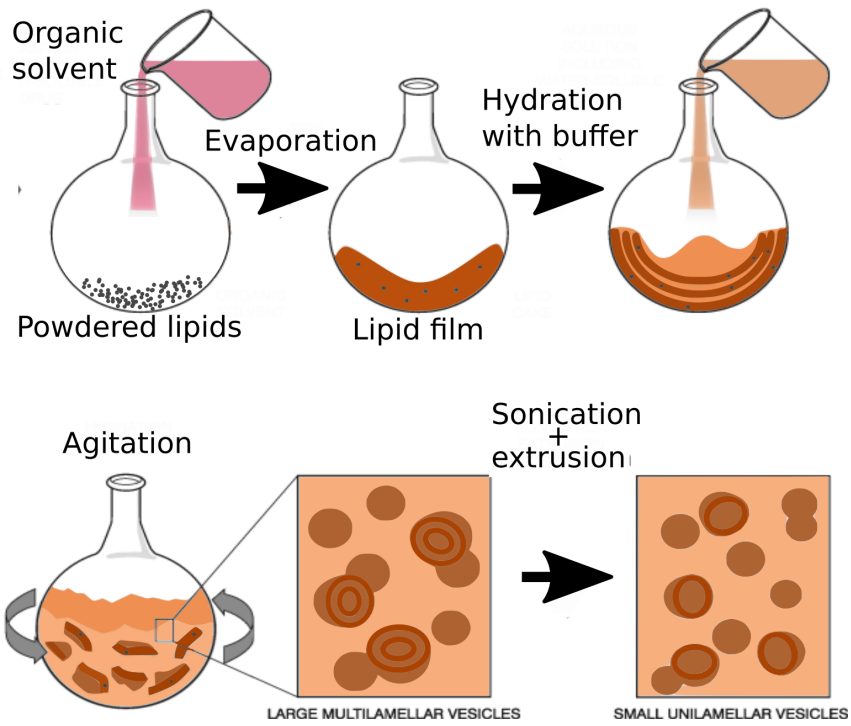

Figure 24: Illustration of the liposome preparation. Image adapted from Avanti polar lipids [88]

All liposomes, regardless of their composition, were produced using the same well-established protocol [88].

First, the correct amounts of the different phospholipids according to the desired ratio were weighed into a round-bottomed flask using scales of 0.1 mg accuracy. The lipids were then dissolved in a volume of chloroform and methanol (3:1) corresponding to the wanted final volume of the solution. The organic solvents were evaporated under rotation using a rotary evaporator. The temperature was kept 10 °C above the transition temperature of the main phospholipid while gradually decreasing the pressure down to 40 mbar until only a dry lipid film was left in the flask. The wanted volume of Tris buffer (pH=7.4) was then be added and the solution was kept under rotation at the same temperature until the whole film was dissolved (about 1 hour). During this step, multilamellar liposomes are formed as the layers of phospholipids are released from the glass. Next, the solution was sonicated in a sonicator bath at the same temperature for 10 min to decrease multilamellarity. After this, the liposomes were extruded using an mini extruder with filters of 100 nm pores. This finally yielded a solution of very monodisperse and unilamellar liposomes of approximately 100 nm diameter.

3.1.2 PEO solutions

All n-alkyl-PEOs were synthesized by Dr. Lutz Willner at the Jülich Centre for Neutron Science (JCNS). The different concentrations of n-alkyl-PEO was made by diluting a stock solution of high concentration (highest used in this thesis was 4.5mg/ml). The liposome-n-alkyl-PEO mixtures were prepared by adding the PEO-solution to an equal volume of the liposome solution and mixing by pipette.

3.2 Dynamic light scattering

To avoid problems with multiple scattering, samples measured with light scattering need to be very dilute. Testing showed a concentration of 1 mg/ml of liposomes would be sufficiently dilute (see appendix, Section 6.3). As DLS measurements are very sensitive to the presence of large particles in the light path, the sample must be made as dust free as possible. This was attempted by filtering the sample into the sample containers (clean NMR tubes) and sealing the tubes inside a pressurized glove box. For all DLS-measurements the DLS-instrument located at the Department of Chemistry, UiO was used. An image can be seen in Figure 25. The instrument has 8 angles, from $\theta = 22°$ to $\theta = 141°$ with $17°$ separation between each angle. The laser has a wavelength of 632.8 nm, and each measurement had a duration of 240 s for which the autocorrelation functions were calculated.

Analysis of the multi-angle DLS measurements consisted of fitting the stretched exponential function of S Section 2.7 to each of the correlation functions resulting from different angles. An example of a fit to the correlations functions from DLS measurements of pure DMPC-DMPG liposomes can be seen in Figure 26 together with the resulting parameters. From this the diffusion coefficient is found by a linear fit of equation 70, shown in Figure 26. The diffusion coefficient, equal to the slope of this linear fit, was then used to find the radius of hydration of the liposomes through the Stokes-Einstein relation (equation 67 in Section 2.7) by using the viscosity of water at 37 °C (0.6913 mPas [89]). The entire analysis was performed using the Origin software (OriginLab, Northampton, MA).

For each liposome with different concentrations of C_{14}-PEO or with PEGylation, DLS measurements were done over time at 37 °C. Each liposome was measured 3 times for each time point to check for variation in between measurements. The standard deviations was calculated from these three executive measurements. The time zero for all measurements is taken to be the first measurement done on that specific liposome preparation so that any difference that would be due to the liposome would be included in all the different mixtures variation over time. The first time point of each liposome mixture should be taken as right after mixing. Although the time here might vary slightly, the time from mixing to first measurement never exceeded 6 minutes, and as each measurement takes 4 minutes, the difference in mixing times is much less than the actual measurement time as is therefore not presented in the data. Between measurements, the samples were kept at 37 °C in an incubator assuring constant temperature.

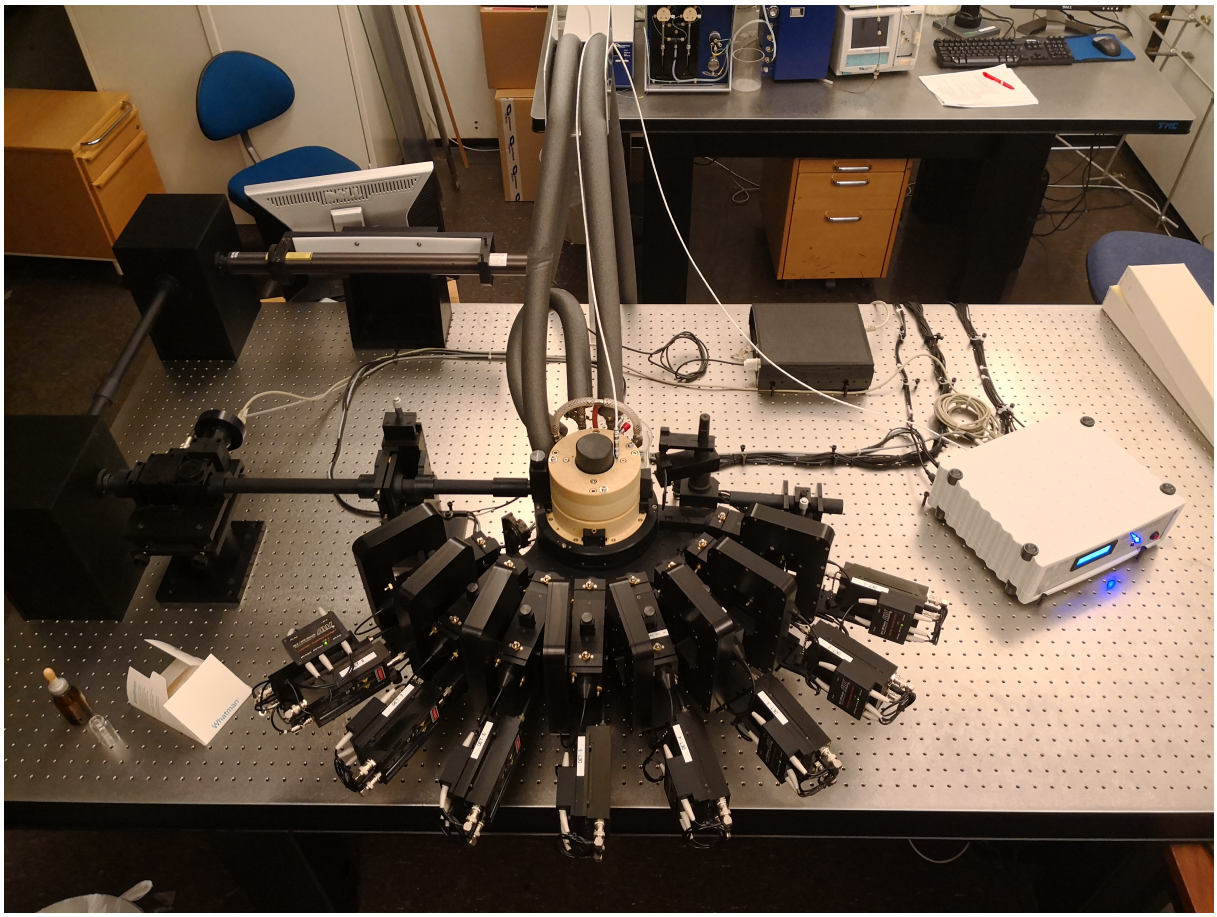

Figure 25: The multiangle DLS instrument at Department of Chemistry, UiO

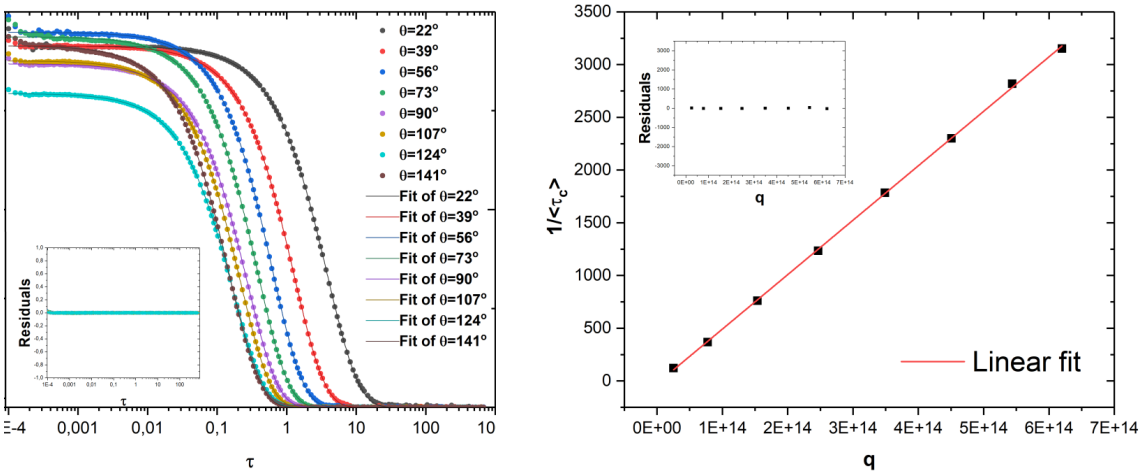

Figure 26: a) shows an example fit of equation 73 to the correlations functions from DLS measurements of pure DMPC-DMPG liposomes with the inset showing the residual plot from the fit. b) shows a fit of equation 70 to data points calculated from the fitted parameters in a) with the residual plot inset.

3.3 Differential scanning calorimetry

Differential scanning calorimetry (DSC) measures the amount of heat that needs to be transferred to/from a sample to change the temperature of the sample by a certain amount compared to a reference. It is therefore a good method for studying the calorimetric properties of soft matter systems such as liposomes, where the studied material is dissolved in a solution. The sample and reference is simultaneously heated or cooled at at constant rate, and the DSC instrument measures the differential heat flow between them over the scanned temperature range. The measurement can either be performed by power compensation or heat conduction.In power compensation, the temperature is actively varied in independent heating/cooling elements, and the instrument measures the additional power that must be added or subtracted to maintain the temperature differential. In the heat conduction method, both sample and reference are immersed in a common source of excess thermal mass, and the temperature difference is recorded [90].

The nano-DSC used in this thesis uses the method of power compensation [91]. The technique relies on a high surface for the heat transfer - as such, it requires relatively large sample volumes (0.3 µL), although not high concentrations, making it optimal for dissolved nano-scale systems. A phase transition in the system is easily detected by the increased amount of heat having to be transferred to/from the sample to change the temperature at certain points as compared to the pure solution. When plotting the heat flow as a function of temperature the transition temperatures are characterised by a peak/inverse peak in the heat flow as the transition requires/releases energy.

All DSC measurements for this thesis were performed by Bente Amalie Breiby at the School of Pharmacy, UiO at a Nano DSC instrument. Solutions were prepared according to the description in Section 3.1 and scanned against a reference of pure Tris buffer (pH=7.4). The data were analysed using the NanoAnalyze software from TA instruments. This analysis involved subtracting the reference, followed by converting the heat flow data to molar heat capacity, c_p:

$$c_p = \frac{\text{heat flow}}{[\text{scan rate}] \times [\text{number of moles lipid}]} \tag{75}$$

The transition enthalpy and transition temperature were determined by the following procedure:

1. Establishment of integration baseline with a first degree polynomial.
2. Integration of the peak to yield the transition enthalpy.
3. Finding the maximum of the peak to give the transition temperature T_m.

For samples showing 2 peaks, steps 1.-3. were performed independently for each peak.

3.4 Small angle X-ray scattering

The theory of small angle scattering has been extensively covered in the theoretical background (section 2.5), so the following section builds on concepts introduced there.

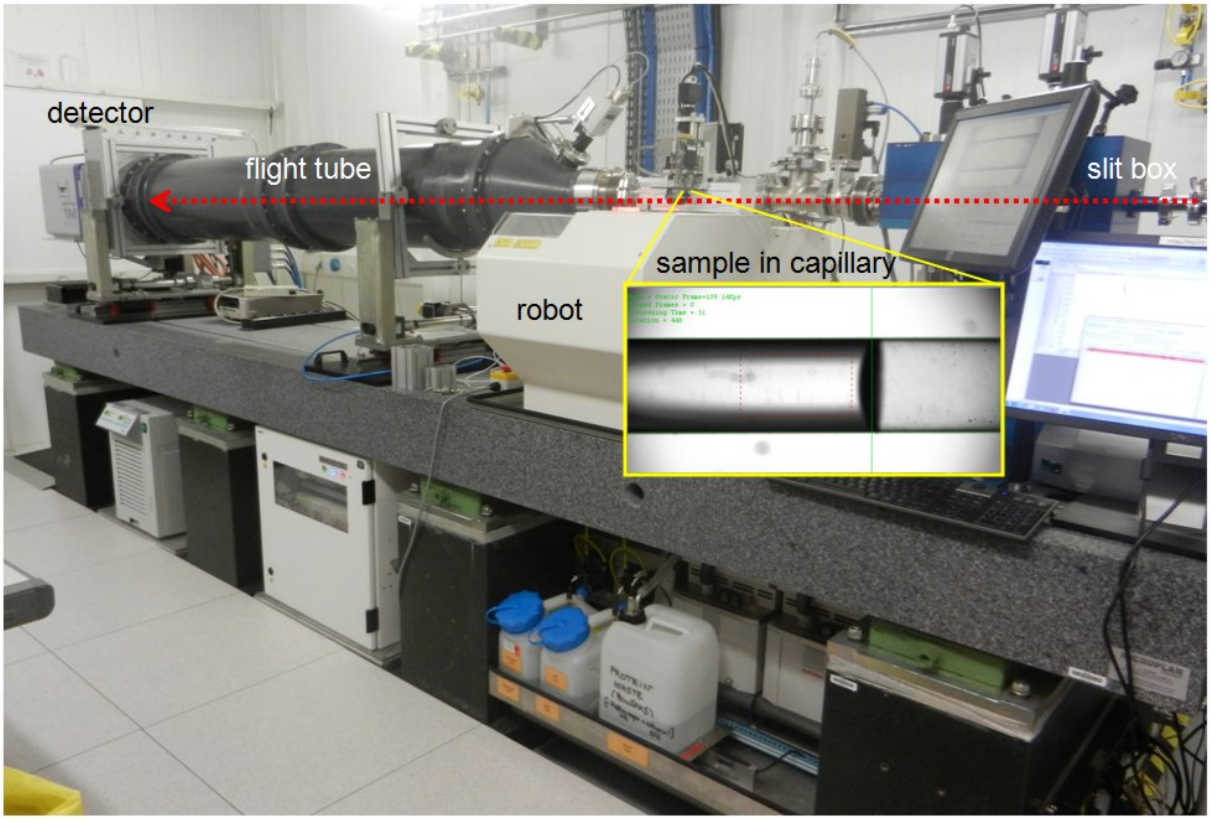

Figure 27: A depiction of the BM29 instrument at the ESRF with description of the different parts. Figure taken from the ESRF website [92].

All SAXS measurements presented in this thesis were performed at the BioSAXS instrument BM29 at the European Synchrotron Radiation Facility (ESRF) in Grenoble, France. The instrument can be seen in Figure 27. The instrument has an automated sample handling system that injects the sample into the exposure cell (capillary). The buffer is measured before and after each sample measurement. The measurement is done under constant flow of the sample through the capillary to minimise radiation damage. The available q-range at the instrument is 0.025-6 nm^{-1}, which corresponds to a maximum detectable length scale of 20 nm in real space.

The primary result from a SAXS measurement is the 2D-detector image. The first thing that happens in treating the resulting scattering pattern is to scale each pixel by the transmitted intensity and data collection time. Intermodulus gaps, hot pixels and beamstop are also removed by using a mask. This is usually based on the calibration with a homogeneous scatterer where the q-independent scattering gives a flat field that in addition to the correcting the above things can also be used to correct for the detector being 2-dimensional while the scattered wave is that of a sphere. For the Pilatus detectors at BM29, all pixels are individually calibrated, there is no dark current and in the SAXS geometry is so that any distortion of the optical path can be ignored. An explicit flat field correction is therefore not needed.

The next thing that is done is the radial averaging (azimuthal integration) of the 2D-detector image. At a radius $r_{\text{detector}} = d_{\text{detector}} \tan(\theta)$ an average of every pixel in that radius is calculated. The centre of this radius is taken from measurements of the direct beam. q is also calculated for each radius as:

$$q = \frac{4\pi \sin(\theta)}{\lambda} \tag{76}$$

So we need calibrated values for the energy, λ, beam position, and the sample to detector distance, $d_{detector}$ for doing the radial averaging and obtaining a $I(q)$ scattering curve [93].

Normalisation to absolute scale, giving the actual scattering cross-section, is done by measuring an internal standard. In the case of BM29, water at 20 °C is used, which has a known scattering cross-section:

$$\frac{d\Sigma}{d\Omega}_{st}(q=0) = 1.632 \times 10^{-2} cm^{-1} \tag{77}$$

This absolute form is independent of instrument settings and so allows us to compare scattering data collected at different instruments and times. Both the empty cell and the cell with the water standard is measured, and the empty cell is subtracted from the water measurement to give I_{st}. The scattering cross-section of our sample $(d\Sigma/d\Omega)_s$ can then be found from [94]:

$$\frac{d\Sigma}{d\Omega}_{s}(\vec{q}) = \left[\left(\frac{d\Sigma}{d\Omega}_{st}(q=0)\right) \Big/ \left(\frac{I_{st}\left(\vec{(}q) \to 0\right) - \text{BG}_{st}}{d_{st} T_{st+cell}}\right)\right] \times \frac{I_s\left(\vec{(}q)\right) - \text{BG}_s}{d_s T_{s+cell}} \tag{78}$$

So we see that the first term in equation 78 equals a scaling factor for our sample scattering intensity that accounts for all instrumental factors. This can be done for every pixel in the 2D-scattering pattern, as it is at BM29, or for the radially averaged $I(q)$ function.

After azimuthal integration and data scaling, averages of both the sample and the two buffer frame measurements are performed. The software at BM29 also compares frames, detects signs of radiation damage on the sample if the frames vary by more than a certain amount and excludes these frames from this average. The averaged background scattering from the buffer is then subtracted from the average sample scattering giving the final scattering curve.

A qualitative analysis was performed involving comparison of the scattering from the measured mixtures with the summed scattering of the individual components. This means that all the components in the mixtures were also measured individually at the same concentration as in the final mixture. The scattering from the references were then simply summed giving the scattering curve we would expect if there was no interaction between the mixed components.

The analytical models described in Section 2.6, as well as in the results section, were programmed in C++ in the QtiKWS software developed by Vitaliy Pipich [95]. Model fits were performed using the Nelder-Mead method as implemented in the QtiKWS software. This method is good for obtaining relatively large improvements after relatively few iterations, but suffers from a lack of convergence theory; this means that the iterations quite often need a complete restart due to numerical breakdown of the algorithm [96]. The algorithm was therefore at times supplemented with the Levenberg–Marquardt algorithm, which is better at convergence but more susceptible to local minima. The polydispersity was modelled using the built in polydispersity option in QtiKWS, using 300 points from a Gaussian distribution of liposome radii to calculate the average scattering at each q value.

3.5 Small angle neutron scattering

The theory of small angle scattering has been extensively covered in the theoretical background (Section 2.5) and so the following section builds on concepts introduced there. All SANS measurements were performed at the very small angle scattering diffractometer with focusing mirror (KWS-3) in Forschungs-Neutronenquelle Heinz Maier-Leibnitz in Münich, Germany (excepting the results from JEEP II, Institutt For Energiteknikk in Kjeller, Norway that are presented in appendix). The instrument has 2 detector distances, covering a q-range from 4.0×10^{-5} - 2.0×10^{-2} $Å^{-1}$ [97].

Each of the liposomes were prepared both in pure H_2O buffer and D_2O buffer at a concentration of 10 mg/ml. For the water transport experiment the liposomes that were prepared in H_2O were mixed with an equal amount of D_2O buffer, while the ones prepared in D_2O were mixed with H_2O buffer. The mixing was done right before the experiment in an eppendorf tube, before injecting the mixture into the sample cell and placing it in the measurement position. The time from mixing to the start of the measurement was on average 1 minute.

The steps in the performed data reduction are as follows:

- The active area of the detector is selected by creating a mask that removes the beam stop, and possibly any tails of the direct beam.
- Scaling by the sensitivity-matrix. Calculation of the sensitivity matrix involves calibration towards a well characterised isotropic scatterer, in our case Plexiglass. Scaling the sample measurements by this sensitivity matrix corrects for detector differences and puts our data on an absolute scale.
- Subtraction of empty cell and background measurements. Equation 78 holds equally well for neutrons to give the data on an absolute scale.

All data reduction was performed in the QtiKWS software [95]. Measurements of the buffer sample were not performed for this experiment as the background is expected to be flat for all samples.

4 Results and discussion

The characterisation for the pure system of liposome without any stabiliser and the C_{14}-PEO by itself is presented first as these provide the references and the basis for analysis of the two stabilised model systems. The results from the C_{14}-PEO stabilised liposomes are then presented and discussed, followed by the presentation of results from the liposomes stabilised by PEGylation. Finally, the results from the studies of water transport across the bilayer of the chosen liposomal system is presented.

4.1 Structural characterisation of lipid vesicles

Although DMPC-DMPG liposomes that have not been modified with PEO on the surface ("unPEGylated" liposomes) cannot be used for studying the interaction with Indolicidin itself, their analysis is important as a reference for the stabilised systems. The liposomes were first characterised for their global structure (overall size) and stability over time using dynamic light scattering. The detailed structure of the bilayer was then investigated using small angle X-ray scattering and quantitatively analysed by fitting the suggested model to the scattering data. The model was tested with two independent batches of liposome.

4.1.1 Global structure evaluation using dynamic light scattering

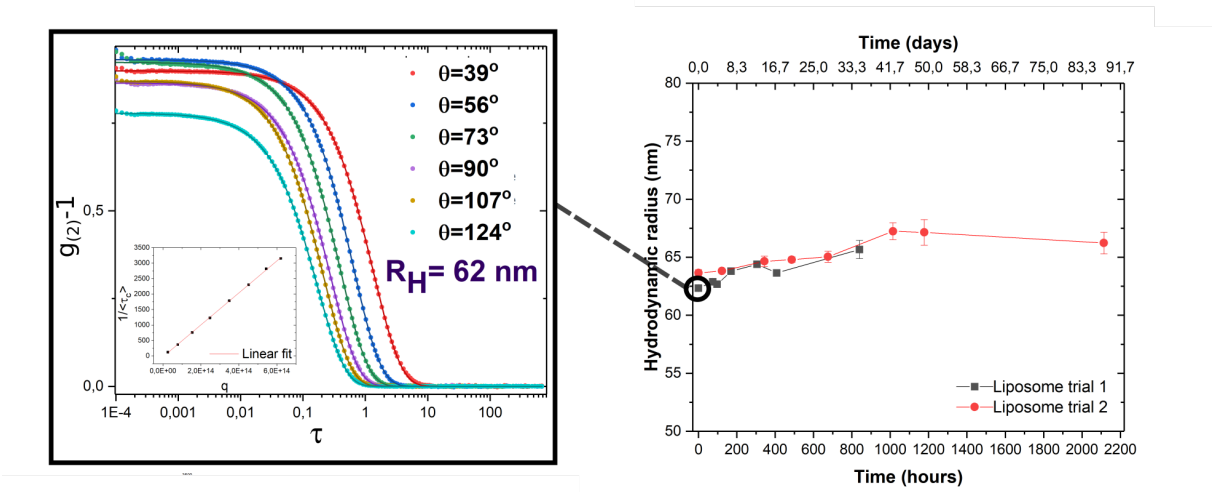

Figure 28: The analysis of the global structure of the liposome. The fit of the stretched exponential of equation 72 gives the q-dependent $\langle \tau_c \rangle$ values. These were then used to find the diffusion coefficient by a linear fit of $\langle \tau_c \rangle$ vs. q^2 according to equation 70. Using the Stokes-Einstein relation the hydrodynamic radius was calculated and found to be 62 nm. The liposomes were kept at 37 °C and the hydrodynamic radius was remeasured at several time points. The result of this analysis is the plot of the hydrodynamic radius over time seen to the right in the figure.

The hydrodynamic radius of the DMPC-DMPG liposomes was determined by DLS measurements. The output of this measurement is a set of autocorrelation functions, one for each detection angle, as seen to the left in Figure 28. This plot also shows the expected q-dependence of the decay - the function decays faster with increasing width of the angle. The stretched exponential function of equation 72 was fitted to the obtained autocorrelation functions to give the excellent fits displayed in the Figure. The resultant fit had β values that were very close to 1 ($0.97 < \beta < 0.98$), which means that the exponential is not very stretched. This signifies a solution that has a quite narrow size distribution. The resulting values from this fit were used to calculate the $\langle \tau_c \rangle$ values for each scattering angle q. As described in the experimental section (Section 3.2), by doing a linear fit of $1/\langle \tau_c \rangle$ vs q^2 the diffusion coefficient D can be derived which directly gives the hydrodynamic radius through the Stokes-Einstein equation (given in equation 67). This analysis gave a hydrodynamic radius of 62 nm for the first liposome trial. The samples were kept and remeasured to see if there was any change in the size over time. The result from all the measurements can be seen in the right graph of Figure 28 where the hydrodynamic radius is plotted against time. The hydrodynamic ra-

dius of the liposomes was found to be reasonably stable over a long time period, not deviating by more than 2 nm after one month.

The obtained values for the hydrodynamic radius of the liposomes were taken as reasonable considering they should have an actual radius of about 50 nm from the extrusion process. Their hydrated radius of about 62 nm is expectedly larger as the diffusion of the liposomes is affected by the accompanying hydration layer of solvent molecules. From following the liposomes over time we see that the values do not deviate much from the originally measured value. The liposomes can therefore be seen as kinetically stable at 37 °C and any effect of additives such as C_{14}-PEO on the hydrodynamic radius should be discernible.

4.1.2 Detailed structural analysis and quantitative data modelling

Before any modifications could be studied, the microscopic structure of the unmodified DMPC-DMPG liposomes was characterised by small angle X-ray scattering. Figure 29 **a)** shows the scattering curves of two different batches of liposome preparations. A qualitative inspection of this curve already shows the typical scattering pattern of a unilamellar vesicles structure. At the very low q values, information about the size and polydispersity of the liposomes can be extracted. In this region it is the interference resulting from the full shape of the particle that dominates, in our case being the spherical form. We see a small plateau in the scattering here which results from the oscillations of the spherical form factor (see equation in Figure 17).

At higher q-values, information about the thickness and contrast of the bilayer is found. It is this intermediate and high q region that gives us the information about the electron density (ED) across the bilayer as seen in 29 **c)** and the volume probability profiles seen in Figure 29 **d)**. The z-values on the x-axis of these two graphs correspond to the position through the bilayer. z=0 is defined to at the position of the CH_3-groups, in the middle of the bilayer. The negative z-values therefore correspond to positions in the inner leaflet while the positive correspond to the outer leaflet. The ED profile simply gives the distribution of electron density as compared to the solvent electron density across the bilayer. The volume probability distribution gives us how the individual components of the bilayer are distributed. Each profile gives the probability of finding the volume of that component at any position across the bilayer. The volume probabilities profiles are particularly interesting because they allows us to obtain the positioning of anything that might be in the bilayer - including peptides. This detailed information is extracted by fitting the model described in Section 2.6.2 to the measured data.

One quite important characteristic of liposomes scattering is the minimum at intermediate q-range. The significance of this minimum is understood from equation 46 in Section 2.6.2. From ED profile in Figure 29 we see that the electron density of the hydrocarbon region is lower than that of water, giving a negative $\Delta\rho$. If the scattering length density of the hydrocarbon weighted by the volume probability at position z is equal in absolute size to that of the head groups weighed by their volumes, they cancel each other out to give a net zero scattering at a specific q-value. In that case the minimum goes to zero. If they only come close to cancelling each other out the minimum is still present, but does not go to zero. Asymmetry in the bilayer causes the minimum to not go to zero; the smearing from the resolution and polydisperisty will also give us a measurement where the

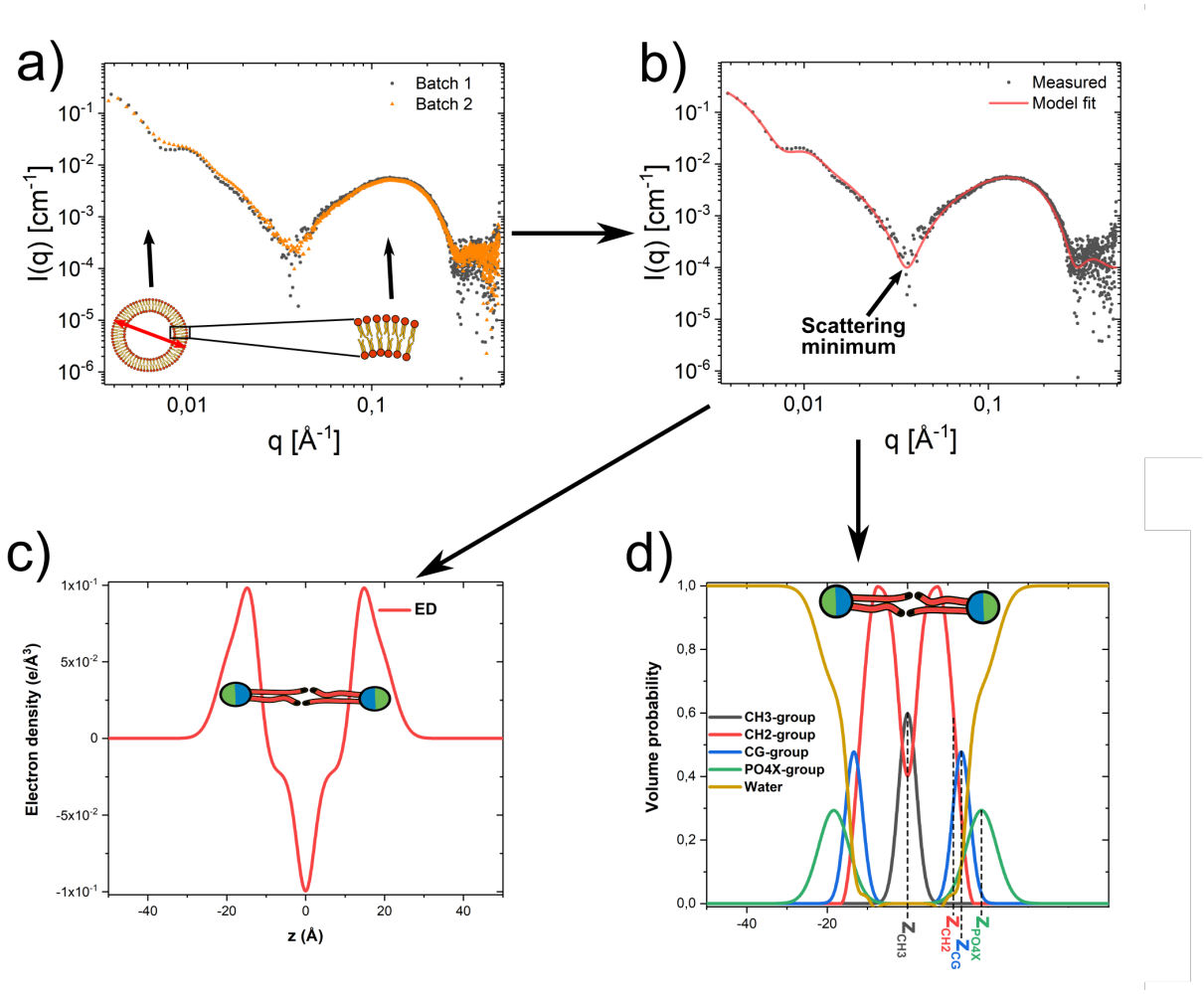

Figure 29: a) The scattering curves of two different replicates of liposomes with illustration representing the correspondence of the scattering with real space length scales. b) The fit of the model from Section 21 to one set of the experimental data. The minimum in the scattering curve is an important characteristic because its q-position is highly dependent on the properties of the bilayer. c) The electron density extracted from the fit in b). d) The volume probability profiles of the lipid components across the bilayer.

minimum does not go to zero even though the bilayer is symmetric. The scattering minimum is very sensitive to anything that changes the scattering properties of the bilayer, and its characterisation is therefore important for studying the effect of additives at a later point.

The qualitative comparison of the two replicates in Figure 29 shows that there is a slight difference at low q, but the scattering at high q overlaps. This implies that there is a difference in the radius and polydispersity of the two batches, but the bilayer structure remains qualitatively unchanged across replicates. To extract more detailed information about the bilayer and vesicle structure, the scattering model from Section 2.6.2 had to be fitted to the data. The result of the fit is a number of parameters that quantitatively describes both the overall liposome structure and the microscopic bilayer structure. The parameters have been adjusted by the fitting algorithm until an optimal fit was found. In the low q-region, the spherical form factor in the model dominates and the radius R and polydispersity are the relevant fit parameters. The radius is in this case the distance from the centre of the liposome interior to the middle of the bilayer, where $z = 0$. A change in these does not affect the predicted bilayer scattering at high q; an illustration of this can be seen in appendix 6.2. For the bilayer region, the volume probability profile as displayed in Figure 29 **d)** gives the full description of the bilayer structure. The phospholipid is partitioned into the groups as described in Section 2.6.2 and the bilayer is assumed to be symmetric for the pure liposomes. The z_i-values are fit parameters in the model, and correspond to the positions of highest probability for each of the phospholipid groups as described by a Gaussian distribution. For the CH_2-group the z_i-value signifies the 0.5 probability of the hydrocarbon region. The σ_i-values describe the width of the Gaussian/CH functions and are also fit parameters in the model. $V_{\mathrm{CH_2}}$, the volume occupied by each CH_2-group is used to calculated the scattering length density of the group and this is also fitted in this model. From this volume, the CH_3-volumes are calculated based on the estimated ratio of 1.9 between these groups [98]. The lipid area is a parameter that gives a change in the bilayer scattering at high and intermediate q, and corresponds to the head group area of the phospholipids. One important characteristic for the fit is the minimum at intermediate q-values. This minimum is important because any change in the scattering of the bilayer, for example due to insertion of peptide, causes this minimum to occur at a different q-value. It was therefore very important that the minimum was correctly determined by the fit of the model to the data.

A common concern with the direct modelling approach is that several models may provide equally good fits as long as enough parameters are introduced. In our case, the general structure of the liposome is very well known from other techniques such as microscopy and diffraction. The uncertainty is therefore in whether our model can accurately determined the exact distribution of the lipid groups in the bilayer. With the amount of parameters included in the model there is still the danger of over-parameterisation and getting multiple good fits that correspond to different volume probability distributions. To avoid this, some parameters were fixed based on values from previous studies and a number of constraints were imposed on the variable parameters that disallowed fits giving unphysical results. The position of the CH_3-groups were set to 0 by symmetry arguments, and their standard deviation to 2.2 Å [21]. The volume of the whole head group (CG+PO_4X) was set to 319 Å, with the CG-volume being 153 $Å^3$ [98]. The values for the scattering length density of the PO_4X-groups were then taken as weighted average values from the relative amounts of DMPC and DMPG lipids. The lipid area was set to the value of 60.4 Å based on previous results obtained for DMPC [99] and DMPG bilayers [100]. The position of the CH_2-groups was constrained to a value greater than $\sigma_{\mathrm{CH_3}} + 2\sigma_{\mathrm{CH_2}}$ to avoid unphysically small values values for the thickness of the hydro-

carbon region. A constraint was also put on the relative z-values of the Gaussian functions as fitting often yielded negative probability values for water. When the probability summed to more than 1 where it is defined to be 1 according to the function for the CH_2-probabilities, the PO_4X-group was moved by the amount that made it have a probability of < 0.01 at this point. This was followed by setting the CG-group to a minimum distance from the CH_2-group that made its probability go to < 0.01. Finally, to avoid probabilities exceeding 1 due to overlap of the CG and PO_4X-functions, the standard deviation of the PO_4X-function was made smaller until the two Gaussian functions summed to the maximum value of 1. This constraint of 0.01 means that negative values on this scale can still happen. It was not made more stringent, however, because increased strictness usually counteracted the fitting procedure, hindering it from attempting new values. As might be seen from the volume probability curve, there is therefore still the possibility of negative water probabilities. This was allowed since the fit was otherwise relatively stable. Noticeably, the concentrations are fit parameters in the model. Although we know the starting concentration of lipids to be 2.5 mg/ml in both cases, quite a significant amount can be lost during the preparation of the liposomes. This loss is due to factors that cannot be perfectly under experimental control, and so fitting the concentration is necessary. This is quite unproblematic, however, as it only involves a scaling of the scattering intensity.

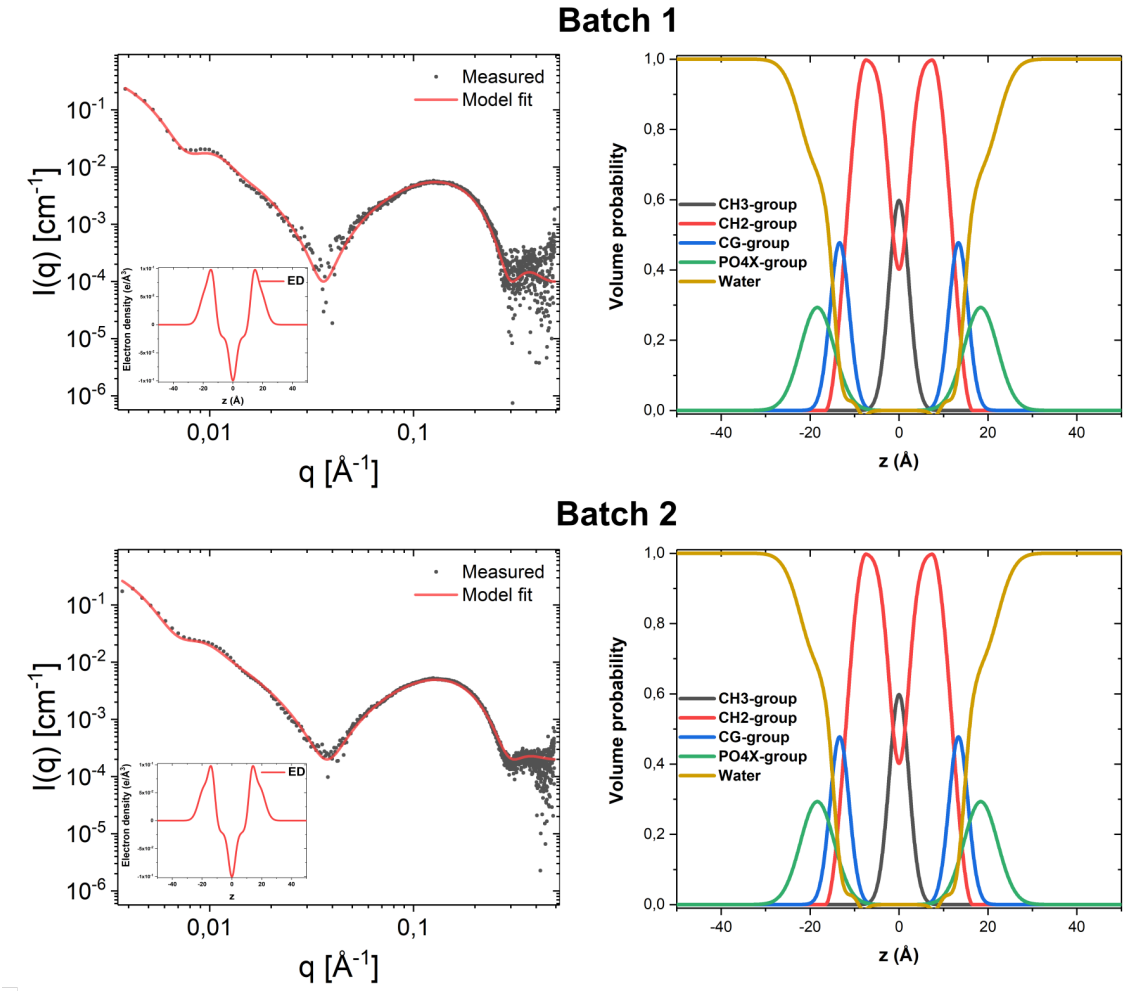

Figure 30: The scattering curves of two different replicas of DMPC-DMPG liposomes with fits of the model described in Section 2.6.2 on the left. Notice that for batch nr.2 the statistics are slightly better and the background is higher than batch nr 1; this is because the two data sets were collected at different beam times at the same instrument. Inset shows the corresponding electron density (ED) profiles. The volume probability profiles of the different phospholipid components are shown to the right of its corresponding scattering plot. Fit parameters are listed in Table 2.

Figure 30 shows the fits to the two batches on the left side. The fitted curves overlaps very well with the measured data; with the imposed constraints the model can therefore describe the measured data perfectly. The achieved fit parameters are given in Table 2. From the fit parameters we then calculated the electron density profile of the bilayer and the volume probability curves of the different lipid components. These can be seen next to their corresponding scattering curve in Figure 30. The volume probability curve summarises most of the results from the fitting. We see that the two batches have almost identical volume probability curves confirming the qualitative observation that they do not differ in their bilayer scattering. Two measures of double layer thickness were also calculated. D_C is a measure of the chain length of the CH_2-group found to be 11.8 Å and 12 Å. D_B is a measure of the full thickness from the inner phospholipid head groups to the outer phospholipid head groups, calculated to be 34.2 Å and 34.8 Å.

From Table 2 we see that the greatest variation in the fits of different replicates are in the concentration and the radius of the liposomes. A variation in radius is to be expected as the extrusion process is very sensitive to different environmental parameters, such as temperature and pressure, that are difficult to have under full experimental control. The loss of material during the liposome preparation is very high; the concentration assuming no loss of lipids should have been 2.5 mg/ml in both cases, so the loss seems to be between 1/3 and 1/5 from the achieved fits. The greatest sources of loss are likely during the hydration process, for example due to formation of other lipid phases than spherical bilayers, as well as the extrusion process. Interestingly, the polydispersity is quite large, an observation that seems to contradict the results from the dynamic light scattering measurements. This is very likely due to the fact that SAXS is more sensitive to the presence of smaller particles. The extrusion process only works to break up liposomes that are larger than 100 nm in diameter, while possible aggregates that are smaller than this are not affected.

The distance between the CG-group and the hydrocarbon interface, at 1.6 and 1.4 Å, is slightly larger than what has been reported for PC-lipids before. Kucerka et al. [99] reports it to be in the range of 0.45-1.1 Å. The extra distance is maybe larger than expected even considering the presence of the PG-groups. The values for the exact positions of the groups varies more than for the other z-values across the two replicates, which is possibly due to the difference in radius. The consideration that the position of the CG-group was the most unstable during the fitting suggests that the partitioning in the model is not completely optimal. Other options were tested though: modelling the PO_4X and CG-groups by a single Gaussian function does not give as good fits of SAXS data, and further partitioning of the head group did not improve the fits either. It was therefore considered the best option within this study to keep the partitioning from Kučerka et al. [79] despite the apparent instability in the positioning of the CG-group.

The volume of the CH_2-groups V_{CH_2} is less than what has been reported before for pure DMPC-bilayers [21] [98]. This parameter is extremely sensitive, as small changes in this value causes very large shifts in the minimum at intermediate q without any of the other parameters being fully able to compensate for this change. Therefore we must assume that the achieved value is reliable within our model, as can be seen across replicates. This also makes the values of the thickness, D_B and D_c, slightly smaller than in previous studies [98]. It is important to note that the previous studies have been liposomes of a single lipid, while in this study a mix of two lipids was investigated. Another consideration is that most results in the literature do not fit the entire q-range as we do; it would be much easier to obtain good fits if only the bilayer region had been used. Importantly,

Parameter	Values batch 1	Values batch 2	Fitted?
Concentration	1.6 mg/ml $\pm$ 0.1 mg/ml*	1.4 mg/ml $\pm$ 0.1 mg/ml*	Yes
Radius	392 Å $\pm$ 10 nm*	422 Å $\pm$ 10 nm*	Yes
Area	60.4 Å	60.4 Å	No
z_{CH3}	0	0	No
z_{CH2}	12.3 Å	12.0 Å	Yes
z_{CG}	13.9 Å	13.4 Å	Yes
z_{PO4X}	18.3 Å	18.4 Å	Yes
σ_{CH3}	2.2 Å	2.2 Å	No
σ_{CH2}	4.8 Å	4.6 Å	Yes
σ_{CG}	2.3 Å	2.2 Å	Yes
σ_{PO4X}	3.8 Å	3.8 Å	Yes
D_B	34.2 Å	34.8 Å	Derived
D_C	11.8 Å	12 Å	Derived
V_{CH2}	25.6 Å^3 $\pm$ 0.1 Å^3	25.64 Å^3 $\pm$ 0.1 Å^3 0.1	Yes
σ_{SD} (Polydispersity)	0.22	0.25	Yes

Table 2: Obtained fit parameters of two replicates of DMPC-DMPG liposomes. A list of the full number of parameters with values used can be found in appendix. The asterisk (*) marks errors that result from evaluation of the fit, as described in the appendix. The other values result from the bilayer scattering which should be the same for the two liposomes batches, so a better description of the error here is the discrepancy between the two values.

our fits include the scattering minimum, which is usually not included in the fitting of the bilayers. Therefore, the values might be expected to deviate from those obtained in previous studies. With this in consideration, all the values seem reasonable when compared to what has been reported for previous systems.

The global structure liposomes as well as that of the bilayer was characterised using the presented model to fit the scattering data. The liposomes were found to have good agreement across replicates with mainly the concentration and radius being very different. This provides us with a reliable strategy and basis for the analytical models for investigating the effect of the PEO-modifications and later peptide addition.

4.2 Structural characterisation of C_{14}-PEO

The block co-polymer C_{14}-PEO is known to self-assembles into micelles. Before testing the effect of stabilisation with these polymers on liposomes, the C_{14}-PEO system had to be properly characterised. To determine any effect the formation of micelles might have on the microscopic structure of the liposomes concentrations below and above the CMC had to be used. The critical micellar concentration of C_{14}-PEO was therefore determined at 20 °C and later at 37 °C by small angle X-ray scattering to decide which concentrations to use for the experiments on steric stabilisation.

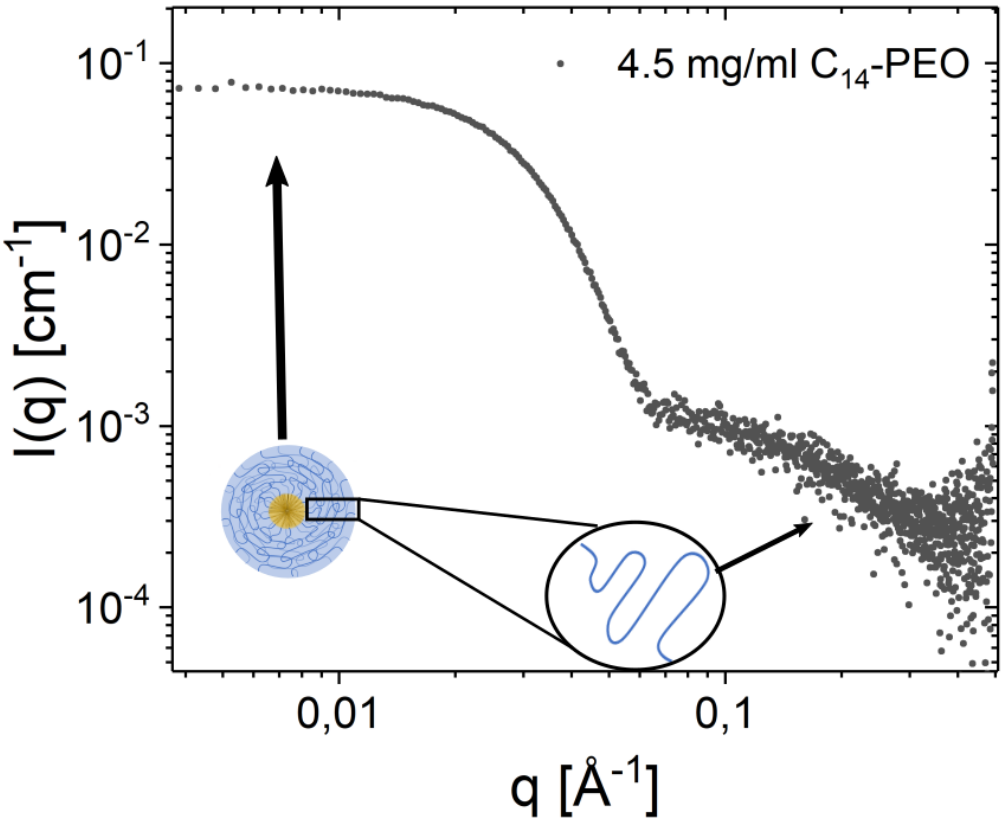

Figure 31: The scattering curve of C_{14}-PEO showing the typical micelle scattering. The plateau at low q gives information about the size of the micelles. At high q we see the scattering dependence typical of polymer chains in good solvents.

Figure 31 shows the measured scattering from one concentration of the C_{14}-PEO. The scattering curve displays three distinct regions of scattering. At low q we see a plateau in the scattering, classically called the Guinier region, which gives information about the overall size of the micelles. This region is also where the structure factor affects the scattering if it is present. Values such as the aggregation number of the micelles and the virial coefficient A_2 from equation 43 can be extracted from this region. The plateau is followed by a sharp decay at intermediate q. This decay is what gives most of the characteristics of the micelles: the micellar radius, R_m, the shell and core size as well as the smearing between them. Changes in these values are therefore expected to be visible in this q-range. The last region consists of a slower decay at high q values, which is characteristic of the single polymer chain scattering and has a $q^{-1.7}$-dependence for polymers in a good solvent.

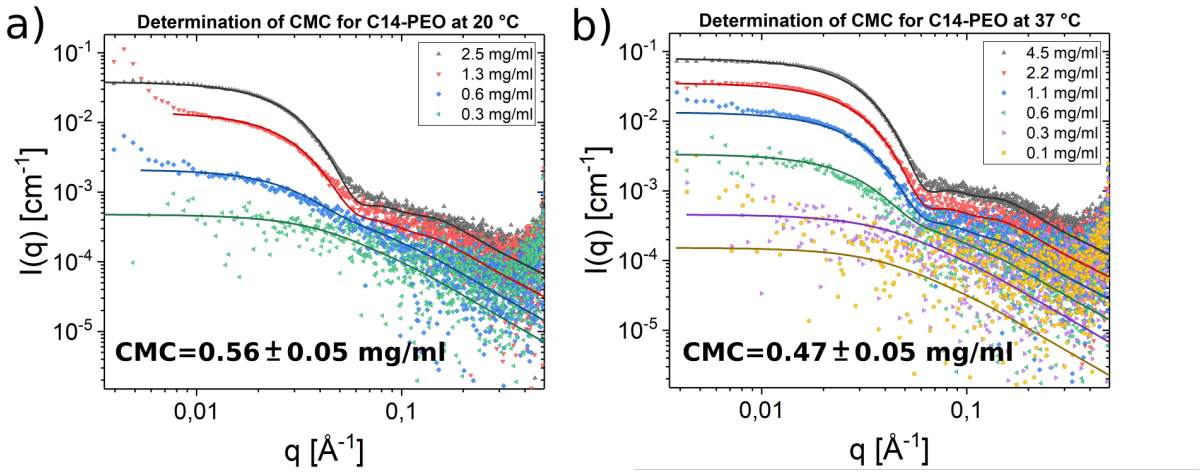

Figure 32: The scattering curves from different concentrations of C_{14}-PEO at 37 and 20 °C with fits for the determination of the critical micellar concentration (CMC) using the model described in Section 2.6.1. Fixed values are taken from other studies characterising n-alkyl-PEO [101] [102]. The error in the CMC is estimated as described in the appendix (Section 6.7). Fits give an aggregation number of 13 and a total radius of 77 Å for 37 °C.

Figure 32 shows the result from measuring different concentrations of C_{14}−PEO at 20 °C and 37 °C in order to determine the CMC. The intensity increases with the concentration independently of which structure is present as there are more scattering units. The concentration at which micelles have been formed in solution is clearly visible from the appearance of the sharp decay in the intermediate q-range at 0.6 mg/ml. The scattering from concentrations below the CMC simply shows the typical scattering of free polymer chains, with a plateau giving the full size of the unimer followed by the power law scattering of the polymers.

To find a more exact estimate of the CMC, we used the model for micelle scattering described in Section 2.6.1 together with some modifications to account for the presence of free unimers of C_{14}−PEO. The fit model accounts for the full scattering from both micelles and free unimers in solution as

$$I_{\text{full}}(q) = (1 - f_{unimers})\, I_{CS} + f_{unimers} I_{chain} \tag{79}$$

where I_{CS} is defined in Section 2.6.1 equation 37 and

$$I_{chain} = \Phi V_{cs} \Delta\rho_{c+s}^2 P_{chain} \tag{80}$$

with Φ being the volume fraction and ρ_{c+s} being the average scattering length of the core and shell forming blocks and all other variables as defined in Section 2.6.1. P_{chain} is the form factor for the polymer chains as defined in equation42. $f_{unimers}$ in expression 79 is defined as

$$\begin{cases} f_{unimers} = 1 & \text{if CMC} > \text{concentration} \\ f_{unimers} = \dfrac{[CMC]}{[concentration]} & \text{elsewhere} \end{cases} \tag{81}$$

The CMC was decided by the scattering contribution of the micelles compared to the contribution of the free block co-polymer that are present in the scattering at each concentration, as shown in equation 81. The model has been fitted to the data in a simultaneous fit of all the different concentrations. The CMC is then the fit parameter that decided at which concentration the micelle scattering occurs. The other fitted parameters were the aggregation number P, micellar radius R_m,

Parameter	Values 37 °C	Values 20 °C	Fitted?
P	13*	13*	Yes
R_m	77 Å $\pm$ 1 Å	79 Å $\pm$ 1 Å	Yes
σ	0.1	0.1	No
R_g	32 Å	32 Å	No
$\hat{\nu}$	7$\pm$ 1	8 $\pm$ 1	Yes
d_f	1.7	1.7	No
A_2	0.006	0.000	Yes
σ_{int}	5	5	No
$R_{G_{\text{chain}}}$	35 Å	35 Å	No
CMC	0.47mg/ml $\pm$ 0.5	0.56 $\pm$ 0.5 mg/ml	Yes

Table 3: Fitting parameter from model fit to C_{14}-PEO at 37 and 20 °C. The global fit itself is very stable. The error in the fit is less than the last significant digit for every parameter, except for the CMC which has an error +/-0.05 mg/ml, evaluated as described in the appendix (Section 6.7). *For the aggregation number P, the error is smaller than 1.

the excluded volume parameter $\hat{\nu}$. The virial coefficient A_2 was fitted to check for structure factor contributions. All other parameters were fixed to values found in to previous studies [78] [101] [102].

The obtained fits can be seen in Figure 32 and the parameters from the model fits are listed in Table 3. The fits are in excellent agreement with the experimental data. These fits are very stable having very small errors in the parameters characterising the micelles. These parameters have very small changes for different temperatures: while the aggregation number remains the same, the micellar radius as well as the excluded volume parameter decreases slightly with increasing temperature. The greatest error is that of the CMC itself. A description of the estimation of error in the fits can be found in appendix 6.7.

The decrease in the micellar radius with temperature is quite small, but can be expected if water becomes a worse solvent for PEO with temperature causing the chains to contract. The change is as expected very small, since we are well below the ϑ-temperature of the polymer. A_2 is very small; any contributions from the interaction between the micelles can therefore be assumed to be very small. The CMC values of 0.56 mg/ml and 0.47 mg/ml is quite low for C_{14}-PEO at the studied temperatures, as compared with for example C_{12}-PEO which does not form micelles at these concentrations and temperatures (see appendix, Section 63). It decreases with temperature, which might be expected; in that case the micellation process is largely still entropy-driven in this temperature range. It does not have a very large shift at the two temperatures, however, and as the system is expected to be at both 37 °C and room temperature during the length of the experiments it was important that the characteristics of the C_{14}-PEO did not change drastically dependent on this.

The analysis of the scattering data provided the necessary characteristics of the micellar system, with the model fitting perfectly to the measurements. The CMC was determined within a reasonable range. To study the steric stabilisation of liposomes C_{14}-PEO, a concentration below (0.3 mg/ml), approximately at (0.6 mg/ml) and above (1.1 mg/ml) the determined CMC were chosen.

4.3 Liposomes sterically stabilised with end-capped poly(ethylene oxide) (Cn-PEO)

The DMPC-DMPG liposomes with C_{14}-PEO added after the liposomes had been fully prepared was first analysed for any change in their global structure as well as their kinetic stability using DLS. Differential scanning calorimetry was used to determine possible changes in the melting temperature of the bilayer, signifying changes in the packing of lipids. The detailed interaction of C_{14}-PEO with the bilayer structure was then analysed using SAXS. For a quantitative analysis the model in 2.6.3 had to be modified. The effect of adding PEI and Indolicidin to the system was investigated using DLS to check for global changes and SAXS for microscopic structural changes.

4.3.1 Global structure and lipid melting temperature of liposomes with C_{14}-PEO

The liposomes were mixed with three different concentrations of C_{14}-PEO (0.3 mg/ml, 0.6 mg/ml and 1.1 mg/ml) as decided upon from the determination of the CMC in Section 4.2. All three concentrations were measured with DLS along with the original liposome for reference. The liposomes were followed over time after mixing. The plot of the measured hydrodynamic radius over time for three replicate trials is given in Figure 33 **b)**, **c)** and **d)**. Figure 33 **a)** shows an example of fits of the stretched exponential function to one of the DLS measurement of the liposomes with 0.6 mg/ml C_{14}-PEO added. The exponentials are not very stretched, and so the C_{14}-PEO does not seem to affect the size distribution of the sample to any great extent. As seen from the first data points in Figure 33 **b)**, for this trial all the liposomes have an initial increase in size, but not in a systematic way - the intermediate concentration shows the least increase in size. Not all replicates showed this initial increase. For the two other replicates in 33 **c)** and 33 **d)** some of the liposomes actually shows a decrease in radius upon addition of C_{14}-PEO. Noticeably, however, the lowest concentration does show a slight, but varying increase for all replicates. For all three replicates, at all concentrations of C_{14}-PEO that were studied, the liposomes have fluctuation in size over time that are much larger than that of the liposome alone. The effect most certainly has a concentration dependence, with the highest concentration showing the largest fluctuations, although a definite trend of the fluctuations is not observable in the replicates. The C_{14}-PEO causes both decreases and increases in the hydrodynamic radius across all replicates, concentrations and time, and it does not seem that an equilibrium was reached even after the span of 3 months (as seen in 33**c)**).

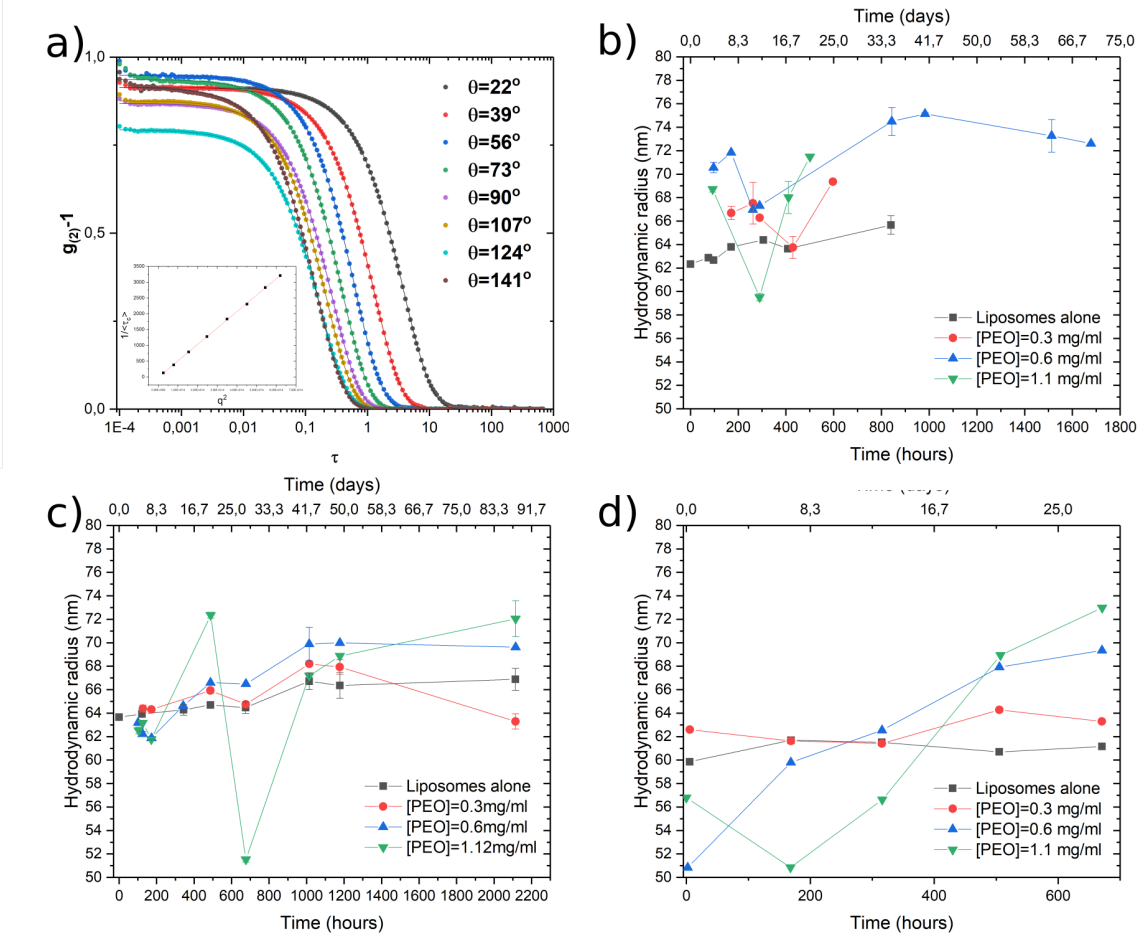

Figure 33: The hydrodynamic radius of liposomes stabilised by C_{14}-PEO. a) Correlation function and fits of the the equations as described in the methods section to one example of DLS data of liposome with 0.6 mg/ml added C_{14}-PEO. b), c) and d) show 3 independent replicates where the hydrodynamic radius of liposomes with and without C_{14}-PEO added was monitored by dynamic light scattering over time. The addition of PEO gives very dramatic changes in radius for all concentrations above the CMC, which might reach an equilibrium radius which is slightly above that of the pure liposome.

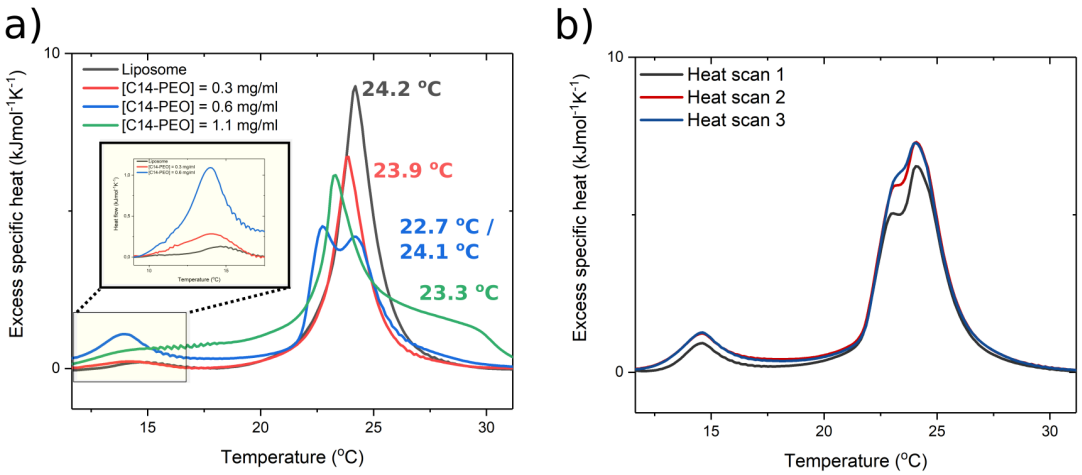

Figure 34: Determination of the melting temperature of liposomes stabilised by C_{14}-PEO. (a) Calorimetric measurements of liposomes with different amounts of C_{14}-PEO added, where a shift in the transition temperature of the liposomes with addition of C_{14}-PEO is observed. The liposomes show a pre-transition temperature, shown more clearly in the inset. A noticeable results is the bimodal peak at [C_{14}-PEO]=0.6 mg/ml, which is right around the CMC at these temperatures. (b) The bimodal peak from (a) was replicated in a second DSC experiment with the same C_{14}-PEO concentration, but a with a higher ratio of lipids.

DSC measurements were performed on the liposomes with the same concentrations of C_{14}-PEO as used for the DLS experiment. The result of the measurement can be seen in Figure 34 **a)**. Two peaks in excessive specific heat can be seen in the plot for the reference liposome without any C_{14}-PEO, one large at 24.2 °C and one very small, zoomed into in the inset, at 14.7 °C. The large peak corresponds to the main melting transition of the bilayer going from the gel state to the liquid crystalline phase, while the small peak corresponds to a pre-transition to the ripple phase. The enthalpy of the transition corresponds to the integral of the excess specific heat, C_p with respect to the temperature, T:

$$\Delta H = \int C_p dT \tag{82}$$

Table 4 shows the transition temperatures as determined by the peak position and the enthalpies of transition for the different systems. For the lowest concentration of C_{14}-PEO (0.3 mg/ml) there is a shift in the transition temperature of the main transition as well as a decrease in the enthalpy. In contrast, the pre-transition enthalpy is increased. For the concentration close to the CMC (0.6 mg/ml) there is actually a splitting of the peak of the main transition. To be sure that these results were not an experimental artefact, the experiment was repeated with the liposomal solution with

C_{14}-PEO concentration (mg/ml)	**Pre-transition**		**Main transition**	
	ΔH (kJ/mol)	**T_m (°C)**	**ΔH (kJ/mol)**	**T_m (°C)**
0	0.7	14.7	20.3	24.2
0.3	1.2	14.2	14.6	23.9
0.6	2.8	14.0	14.7	22.7/24.1
1.1	-	-	29.9*	23.3
0.6 (halved C_{14}-PEO:lipid ratio)	1.8	14.6	22.9	23.1/24.1

Table 4: Calculated transition enthalpies of the lipid bilayer at different concentrations of C_{14}-PEO. *Integral is taken under the whole range shown in Figure 34 due to lack of a proper baseline in this range.

0.6 mg/ml C_{14}-PEO, but with a higher lipid concentration and more heat scans. This gave the same results as before, seen in 34 **b)**. This effect was also observed for liposomes with C12-PEO at concentrations around its CMC (appendix, Section 6.9). The highest concentration does not have a reliable baseline due to the smearing of the transition, so its calculated enthalpy likely does not represent the true enthalpy in the transition. Excluding the highest concentration, the enthalpy of the main transition decreases with increasing C_{14}-PEO concentrations, while the enthalpy of the pre-transition increases.

One approach to quantitatively determine the cooperativity of the transition is to calculate the cooperative unit size of the bilayers as suggested in literature [103] [90]. These values give us little information as it is difficult to compare the different systems when they all have different peak shapes. From a qualitative inspection of the curves in Figure 34 it is obvious that the cooperativity in the transition, being inversely related to the temperature range over which the transition occurs, decreases with increasing C_{14}-PEO.

If the C_{14}-PEO simply attached to the surface of the liposome, we would expect only a small increase in the hydrodynamic radius of the liposome. Even though all liposomes seem to show a slight increase in radius over time, the drastic fluctuations suggest that they do not simply add to the surface of the liposomes as intended, but induce accelerated lipid dynamics in the liposomal system as well. Increased dynamics is in this case used to describe that the phospholipids have increased mobility to exchange between liposomes. These results might mean that the C_{14}-PEO actually solubilises the phospholipids, increasing the lipid exchange, and thus creating a very dynamic system. The lipids might then exist in solution as mixed micelles of phospholipid and C_{14}-PEO. The DLS results are overall difficult to interpret, but clearly displays that the system has lost its kinetic stability when comparing with the reference DMPC-DMPG liposome. The possible explanation of the varying result can be partitioned into the following steps: i) the liposomes are partially dissolved by the C_{14}-PEO, causing liposomes to become destabilised and decrease in size due to lipids being removed, ii) lipids that come into solution due to the destabilised membrane is the cause of increased lipid dynamics, which in turn leads to iii) growth of the intact liposomes.

The results from the DLS are supported by the DSC results, which show some interesting behaviour above the CMC of C_{14}-PEO. A clear overlap of two peaks occur at the intermediate concentration of C_{14}-PEO. At the highest concentration the peak is very deformed, either because the melting process has been made much less cooperative (such as how impurities affect transitions) or because of the co-existence of many forms of aggregate with variable melting temperature. This last scenario is likely the case for the bimodal peak at intermediate concentration. The C_{14}-PEO might be inserting inhomogeneously, causing different domains to transition at different temperatures.

The DSC results also show that the enthalpy of the main melting transition is decreased with increasing C_{14}-PEO concentrations. This might be explained by phospholipids being removed from the liposomes or by the C_{14}-chains having an already ”melted” structure in the observed temperature range that facilitates the transition. Tetradecane (C_{14}) has a melting point of 5.87 °C [104]. If the C_{14}-chain inserts into the bilayer it is expected to affect the melting temperature. The C_{14}-chain attached to PEO is expected to have higher mobility than the chains in the phospholipids, and might keep this mobility when inserted into the phospholipid bilayer. This could explain the lower transition enthalpy. Interestingly, the C_{14}-PEO seems to enhance the enthalpy of the pre-transition. The

most reasonable explanation for this is that layer of polymer on the surface of the bilayer makes it more resistant to the ripples of the ripple phase. Other studies have shown the importance of the head group in the pre-transition [105], supporting a hypothesis that the increased enthalpy is due to the head groups rather than the packing.

In summary, the DLS and DSC results presents the C_{14}-PEO as a poor option for stabilising the liposomes. Although they do stabilise against AMP-induced aggregation, the effect of the AMP in this system is difficult to interpret when one has to take into account the effects C_{14}-PEO itself has on the system. The next step was to see whether the insertion of the C_{14}-PEO could be observed with SAXS and quantitatively analysed using model fits.

4.3.2 Detailed structural analysis using derived scattering model

Figure 35 show the scattering curves obtained from SAXS measurements of the liposomes mixed with the three different concentrations of C_{14}-PEO (0.3 mg/ml, 0.6 mg/ml and 1.1 mg/ml). The calculated scattering curve is simply the sum of the DMPC-DMPG liposomes and C_{14}-PEO measured individually. If the C_{14}-PEO has no interaction with the liposomes, the measured and calculated curves should overlap as the two systems would scatter independently. If C_{14}-PEO inserted without changing the lipid packing, we expect the size of the liposomes to slightly increase giving a difference at low q, but without changing the scattering at high or intermediate q. The two highest concentrations do show a considerable shift in the scattering intensities in the intermediary q-range as well as a shift in the low q-range compared to the calculated intensity. This suggests that the C_{14}-PEO affect the liposomal bilayer in addition to changing the size of the structure. At the lowest concentration the shift in the intermediary q-range is not considerable, while the shift at low q still suggests a size change.

For the liposome model with n-alkyl-PEO, we needed a fit model that accounted for the presence of free n-alkyl-PEO and micelles in solution as well as the effect of insertion of the single n-alkyl-chain into the bilayer before. For this, the model for the micelle scattering described in Section 36 was included into the model in Section 2.6.3. This was done by linking the free n-alkyl-PEO with the PEO that is grafted onto the liposomes with a new parameter f_{bound}. f_{bound} is equal to the fraction of the the n-alkyl-PEO concentration that has inserted into the liposomes. f_{PEG} is then

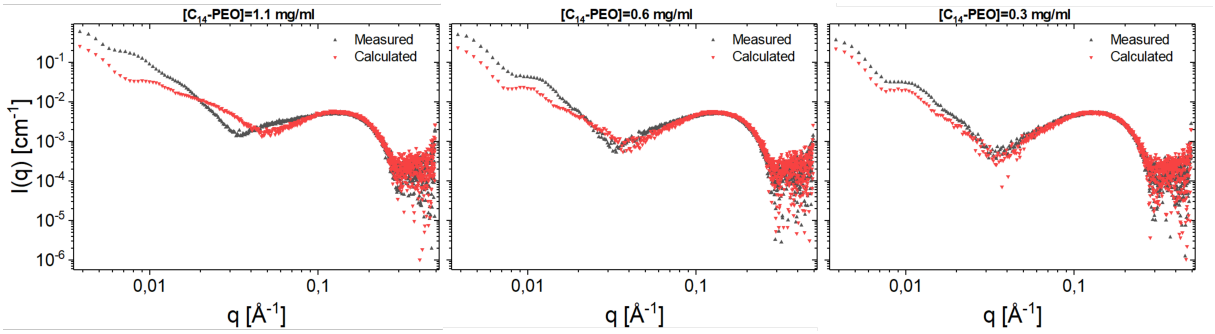

Figure 35: The measured scattering curves of liposomes (2.5mg/ml) with different concentrations of C_{14}-PEO representing molar ratios of 7.4:1, 14.8:1 and 29.6:1 of lipids:C_{14}-PEO respectively, together with the calculated scattering curves of the sum of the scattering intensities of liposome and C_{14}-PEO by themselves. Fits of the model described in this Section are shown for the two lowest concentrations, as well as in figure 36.

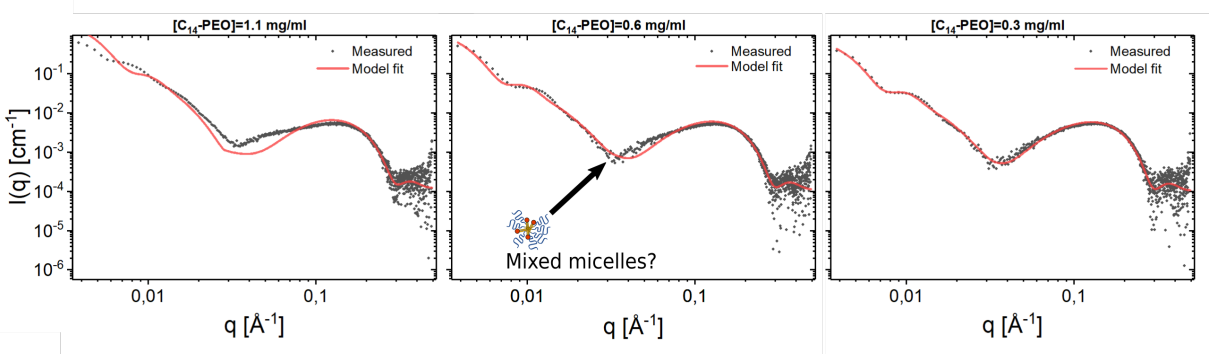

Figure 36: Fits of the model in 2.6.3 to the experimental data. It was not possible to achieve good fits at for the higher concentrations, possibly due to the presence of mixed micelles that contribute to the scattering in this q-range.

calculated from f_{bound} by

$$f_{PEO} = \frac{c_{\text{PEO}} f_{\text{bound}} / (M_{\text{PEO}})}{c_{\text{PEO}} f_{\text{bound}} / M_{\text{PEO}} + c_{\text{lipid}} M_{\text{lipid}}} \tag{83}$$

and used in expression 60 in Section 2.6.3. The unbound n-alkyl-PEO concentration, $c_{\text{PEO}}\,(1 - f_{\text{bound}})$ is used to calculate the volume fraction as in Section 2.6.1. To account for the insertion of single chains into the outer leaflet of the bilayer, the volumes of the outer groups, V_{i_o} (i=CG,PO_4X,CH_2) were changed with volume of the corresponding group in n-alkyl-PEO $V_{i_{\text{PEO}}}$ in correspondence with their fraction:

$$V_{i_o} = V_i\,(1 - f_{PEO}) + V_{i_{\text{PEO}}} f_{PEO} \tag{84}$$

and the scattering length density of the head groups were changed as:

$$\rho_{i_o} = (1 - f_{PEO}) \frac{b_i}{V_i} + f_{PEO} \frac{b_{\text{PEO}}}{V_{\text{PEO}}} \tag{85}$$

This corresponds to making a sort of new ”pseudomolecule” that accounts for the scattering by weighing the contributions from the C_{14}-PEO and the phospholipids to the scattering length of the new pseudomolecule by their amounts.

The PEO-chains were set to start at the hydrocarbon interface, so that R_{inner} and R_{outer} in expressions 61-65 were defined as:

$$R_{\text{inner}} = R + z_{\text{CH}_2,i} \tag{86}$$

$$R_{\text{outer}} = R + z_{\text{CH}_2,o} \tag{87}$$

where R is is the radius of the liposomes defined to the position of the CH_3-groups, as used in Section 21. The expression for the final scattering intensity that is fitted to the data is then

$$I_{\text{full}}(q) = I_{\text{PEO-liposome}}(q) + (1 - f_{unimers})\, I_{CS} + f_{unimers} I_{chain} \tag{88}$$

with I_{CS} as defined in equation 37, Section 2.6.1 and with $f_{unimers}$ and I_{chain} defined in Section 4.2.

The only parameter that was fitted in the model was the new f_{bound} parameter. This in turn affects the other parameters through the changes made to the model as described above. The other parameters were set according to what had already been obtained from fitting the DMPC-DMPG liposomes (Section 4.1.2) and C_{14}-micelles (Section 4.2). This can be done since the measurements were performed using the same batches as used in these sections at the same beamtime.

The obtained fits can be seen in Figure 36. The lowest concentration is well describes by simply fitting the amount of bound PEO (f_{bound}) in the membrane in the model. The same procedure was

C_{14}-PEO concentration (mg/ml)	f_{bound}	$[\text{PEO}]_{\text{free}}$	f_{PEO}
0.3	0.44	0.17 mg/ml	0.010
0.6	0.40	0.36 mg/ml	0.020

Table 5: The resulting values from fitting the model described in Section 2.6.3 to the SAXS-data from liposomes with added C_{14}-PEO. f_{bound} is the fraction of C_{14}-PEO that is bound in the bilayer, $[\text{PEO}]_{free}$ is the concentration of C_{14}-PEO left in solution or micelles, f_{PEO} is the is the fraction of lipid content that the C_{14}-PEO constitutes in the liposome. Values for the highest concentration is not included since a fit was not obtained.

attempted with the 0.6 mg/ml concentration, but here it was necessary to set the CMC to zero to get a reasonable fit, corresponding to a situation where all the C_{14}-PEO unimers are forming micelles or have attached to the surface of the liposome. The resulting values from the fit are given in Table 5. No reasonable fit of the model was achieved for the liposomes with the highest concentration, as displayed in the figure. The f_{PEO} values are quite low still, at 1 % and 2 %, so the polymers that have attached to the surface are expected to be in a mushroom conformation and assuming good solvent conditions to have their solvated radius of gyration, as is assumed in the modelling. An estimate of the distance s between the chains on the surface can be taken as (see appendix 6.5 for derivation)

$$s = 2\sqrt{\frac{a_0}{\pi \times f_{PEO}}} = 2\sqrt{\frac{60.4\mathring{A}^2}{0.01}} \approx 87.7\mathring{A} \tag{89}$$

which is almost three times the length of the radius of gyration.

The detailed analysis of the SAXS data show that at the concentration below the CMC the scattering can be accounted for by a model that merely inserts the C_{14}-chain into the bilayer, creating a stabilising layer og PEO on the surface of the liposomes. This is in correspondence with the results from DLS and DSC described in the previous section for this concentration. Although the C_{14}-PEO might still induce some dissolution of phospholipids these are not visible from the SAXS pattern. The liposomes are not followed over time as they were with the DLS, and it could very well be that the same size fluctuations would be observed with SAXS if they were measured over similar time scales with this technique. The fact that the CMC had to be set to 0 in the fit of the intermediate concentration of C_{14}-PEO suggests that there is a change in the C_{14}-PEO system as well. The lowering of the CMC be the case if the phospholipids act as good nucleants for micelle formation, thereby forming mixed micelles. There is still some scattering at intermediary q that is unaccounted for in the model, and this is possibly from the hypothesized mixed micelles. Although models might account for the scattering from these micelles, it would be difficult to design a system of only mixed micelles to test such a model. It would in addition introduce a large number of free parameters accounting for the new structure to the model, making the model over-parametrised. Therefore it was not attempted to introduce any mixed micelle scattering into the model used for our system.

Overall, the observations from the SAXS measurements supports the previous observations from DLS and DSC that the C_{14}-PEO partially dissolves the liposomes and forms mixed micelles. It does, however, confirm that C_{14}-PEO becomes grafted onto the liposomes forming a low-density layer of PEO. The modified model can account for this change, as shown by the liposomes with the C_{14}-PEO concentration below the CMC, but cannot account for the presence of the new species of mixed micelles.

4.3.3 Addition of PEI

As described in the Introduction, the C14-PEO stabilises the liposomes from a macroscopic phase separation by PEI. With this, the next step was to test if the PEI still had some microscopic effect on the structure of the liposomes using DLS and SAXS using the same procedure as for the testing of the effect of C_{14}-PEO addition itself, described in Section 4.3.1. Any effect that PEI might have with C_{14}-PEO alone was also investigated by SAXS measurements.

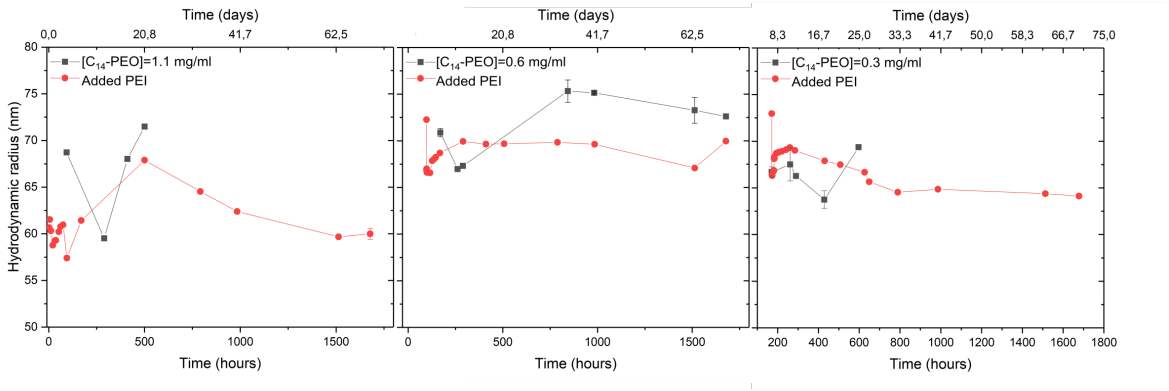

Figure 37: DLS measurements over time of liposomes with C_{14}-PEO after addition of PEI. The black data points correspond to the liposome with different C_{14}-PEO concentrations and correspond to the ones depicted in (b) of figure 33. The PEI seems to actually decrease the hydrodynamic radius compared to the effect of C_{14}-PEO only.

The results from the DLS measurements of liposomes with added C_{14}-PEO followed by addition of 0.8 mg/ml of PEI can be seen in Figure 37. The measurements were done immediately after mixing. They show that the radius seems to actually have decreased compared to the liposomes with C_{14}-PEO. The measurements are following the same fluctuations as the ones with C_{14}-PEO alone and it is difficult to discern whether the decrease in size is an actual effect or not. What seems to be sure is that PEI does not have much effect on the hydrodynamic radius compared to the pure liposome.

SAXS-measurements of the different PEI concentrations mixed with the highest concentration of C_{14}-PEO without any liposome were performed to check for any possible interaction between the two components and can be seen in Figure 38. The calculated curve from the sum of the C_{14}-PEO scattering and PEI scattering overlaps completely with the measured scattering for the low concentration of PEI. There is a small difference at the low-q data for the highest concentration of PEI which might suggest an aggregation, but data at lower q are required as the statistics are not good enough to confirm this. Importantly, however, the PEI concentration used in the DLS experiments did not show any signs of aggregation.

From the SAXS measurements of the liposome with C_{14}-PEO and PEI, shown in Figure 39, there is no difference between the calculated and measured scattering, indicating that the PEI does not have any interaction with the liposome. Any interaction of PEI with the C_{14}-PEO is not discernible here either, since we then expect a difference from the calculated curve. The results suggest that the C_{14}-PEO and liposomes act completely independently of the added PEI. Interestingly, when measuring the concentration of liposome used in the DLS-experiments (Figure 40), there is a slight difference in the high-q region between the measured and calculated curve.

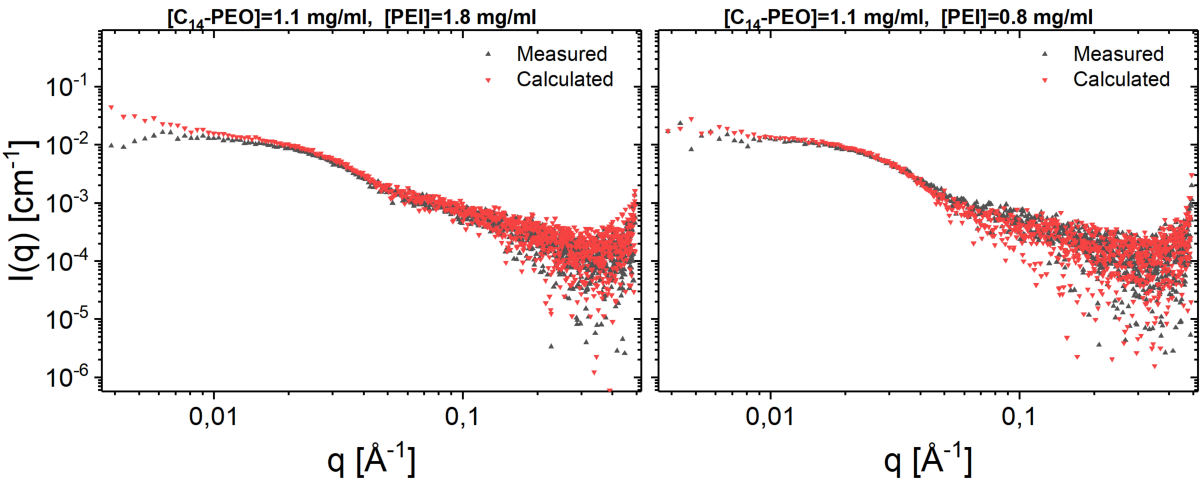

Figure 38: SAXS measurements of C_{14}-PEO mixed with PEI seem to suggest some aggregation with the highest concentration of PEI and C_{14}-PEO (left graph), but there is no difference in the calculated and measured scattering curves of the lower concentration of PEI (right graph).

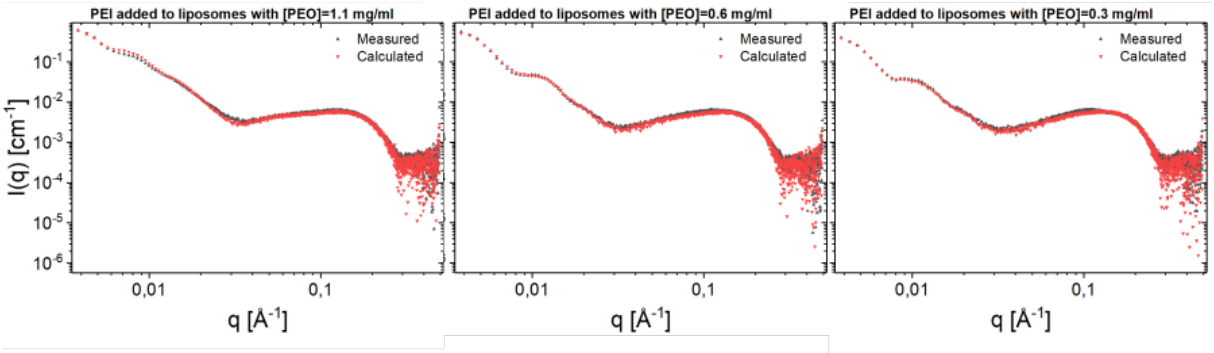

Figure 39: SAXS measurements of liposomes (2.5 mg/ml) with different amounts of C_{14}-PEO with 3.7 mg/ml of PEI added to the system. The results reveal little difference between the calculated and measured scattering, suggesting that PEI has little effect on the structure of the bilayer and on the overall structure of the liposome.

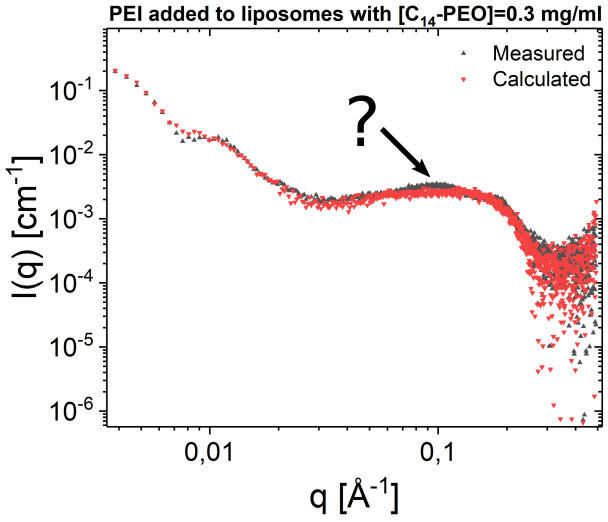

Figure 40: SAXS measurement of liposome (1 mg/ml) with a low concentration of C_{14}-PEO (0.3 mg/ml) and a high concentration of added PEI (3.7 mg/ml) indicates effect of the PEI in the bilayer.

The hypothesis was that if the addition of PEI/peptide to the liposome disrupts and breaks the membrane, this causes an increase in the lipid exchange between liposomes resulting in a growth of the liposomes. This was contrary to what was observed in the DLS measurements. Since the hydrodynamic radius appears to actually decrease, it was hypothesized that the PEI might interact with the C_{14}-PEO, causing it to be withdrawn from the liposomal system. Due to the low concentration of lipids used in DLS, the PEI-to-lipid ratio is very high. Therefore, if PEI actually has an effect on the lipid dynamic we still expect this to be quite clear from the result, regardless of any interaction with free C_{14}-PEO. The SAXS measurement showed some difference at low q, but the statistics are too bad to say anything certain about aggregates. In addition, any aggregates of the size that is out of the probing range of the SAXS measurement should have been visible in the DLS measurements, as this leads to a stretching of the exponential function with β values deviating a great deal for all angles. Such observations were not made. It is therefore questionable whether aggregation had any effect in the DLS measurements at all. The difference in size did not show itself until after several days with DLS, though, so it might be that the PEI-C_{14}-PEO-interaction is slow kinetically speaking, and that the timescale of the SAXS experiment was therefore too short. The time one gets for such experiments at the synchrotron is usually 24 hours. One option which could solve such problems in the future would be to mix the components some days before the scheduled beamtime and compare these aged samples with the ones mixed at the beamline.

There is a slight effect in the bilayer scattering at the very high ratio of PEI. The effect does not resemble that of any intercalation of the polymer into the membrane since it does not affect the minimum at intermediate q. One might think that the PEI only loosely associates with the surface of the liposomes, but this association is in that case not visible on neither the global structure as measured by DLS nor the microscopic structure as measured by SAXS. No fit of the liposomes with PEI was attempted since this would anyway largely just correspond to the previous fits of Section 4.3.2 with the PEI scattering simply added.

In summary, although PEI clearly must have an interaction with the pure liposomes since it causes a macroscopic phase separation, it does not seem to interact with the membrane in the C_{14}-PEO system. It could be that PEI has a purely flocculating effect on the liposomes due to its cationic charge, but does not really interact microscopically with the membrane. In this case the C_{14}-PEO masks the charges of the membrane from the PEI making it ineffective as a flocculant.

4.3.4 Addition of Indolicidin

The effect of Indolicidin on the C_{14}-PEO liposome system was investigated using the same approach as for the PEI.

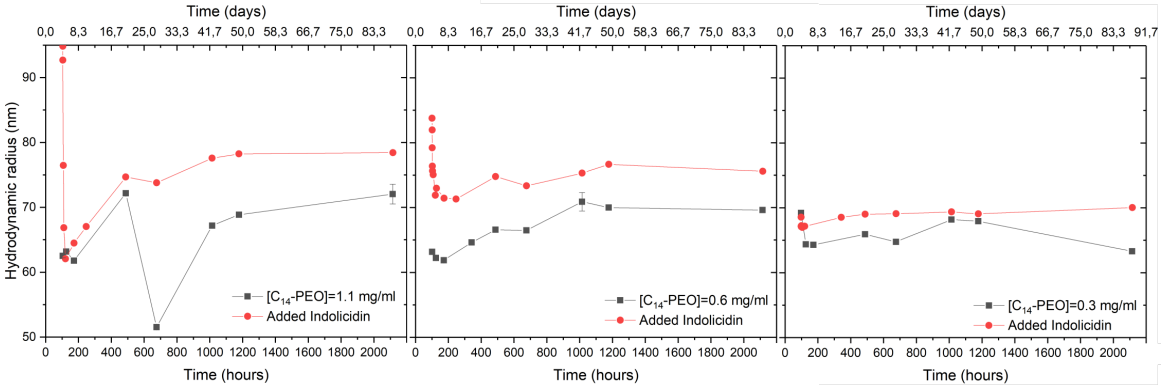

Figure 41: DLS measurements over time of liposomes with C_{14}-PEO after addition of indolicidin. The black, square data points are the liposome with different C_{14}-PEO concentrations and correspond to the ones depicted in (a) of figure 33.

The results from the DLS giving the changes in the hydrodynamic radius upon addition of 0.7 mg/ml can be seen in Figure 41. The addition of the antimicrobial peptide does seem to cause an initial increase in the hydrodynamic radius of the liposomes (Figure 41), but this increase is quite small. Since the effect actually decreases with decreasing C_{14}-PEO concentrations, it is questionable whether this is the effect of the peptide or just another effect of the C_{14}-PEO on the liposomes. Strangely, there is a very drastic increase in the beginning right after addition of the Indolicidin, with the system then decreasing in size almost down to the original value of the liposome.

SAXS measurements were performed to test whether the C_{14}-PEO might interact with the peptide as well. Figure 42 **b)** shows the scattering from highest concentration of C_{14}-PEO mixed with the highest Indolicidin concentration. The scattering of the individual components that are summed to give the calculated intensity in 42 **b)** are displayed in 42 **a)** for comparison. If the Indolicidin had no effect on the micelles or vice versa, we expect this calculated scattering curve. Instead we see a scattering curve that indicates that the micelles are smaller in presence of Indolicidin, as seen by the shift the decay of the curve to higher q-values than for the original micelles. The upturn at low q that we see in the calculated scattering curve is largely due to the presence of Indolicidin clusters that are normally present in pure Indolicidin solutions. This scattering is reduced for the measured curve, signifying that clusters are removed from solution. The other measurements, presented in Figure 43, show a clear trend with increased C_{14}-PEO and Indolicidin concentrations, supporting these results. There is an increasing shift of the scattering curves with increasing either the C_{14}-PEO concentration or the Indolicidin concentration.

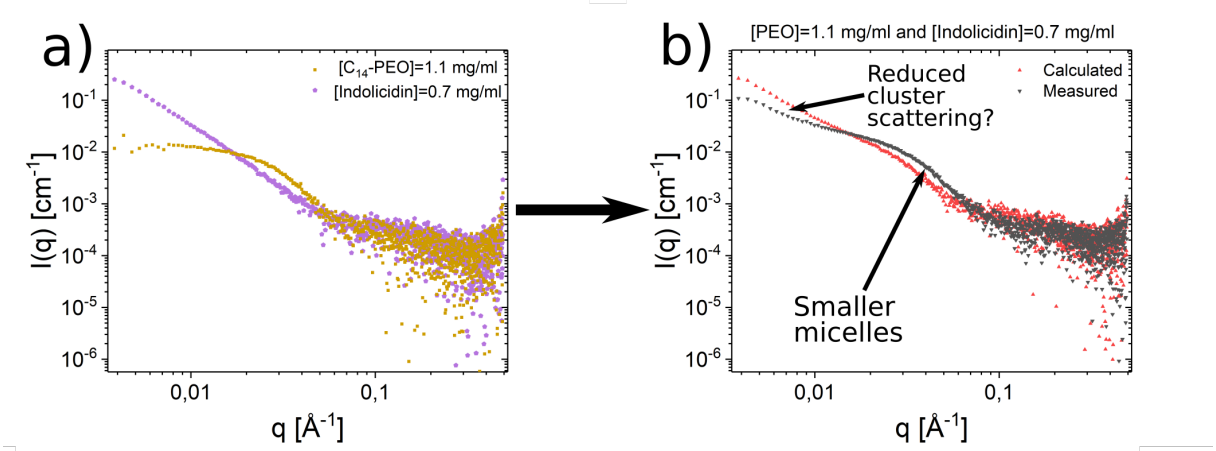

Figure 42: SAXS measurements of C_{14}-PEO mixed with Indolicidin. There is clear difference between the expected scattering curve if the two components acted independently in solution (calculated) and the measured. This increase in scattering at possibly described by the formation of clusters of the C_{14}-PEO micelles.

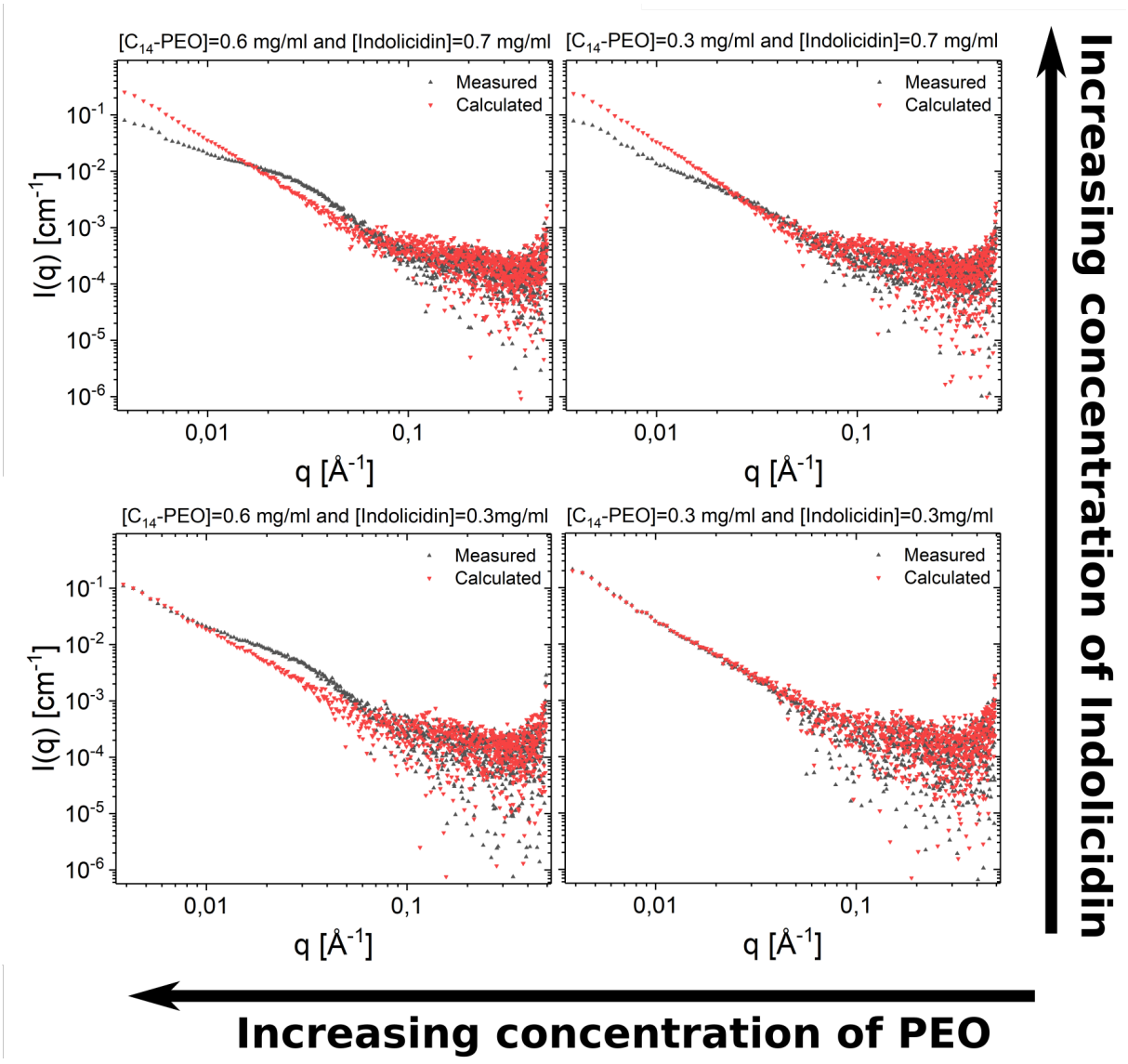

Figure 43: SAXS measurements of the different concentrations of C_{14}-PEO mixed with two concentrations of Indolicidin. While there is no difference at the lowest concentrations of the two substances, there is a clear interaction effect increasing with increased concentration of either component.

The addition of Indolicidin to C_{14}-PEO stabilised liposomes has a considerable effect on the scattering curve, as can be seen from Figure 44. The minimum at intermediate q of the measured curve is shifted compared to the calculated average, suggesting that there is an increase in scattering from the bilayer. Simply adding the effect from any C_{14}-PEO-Indolicidin aggregates does not cause such a shift. Another observation is that the shift seems to be quite similar for all the different C_{14}-PEO concentrations. There is also an increase in the size of the liposomes and they are more polydisperse.

The DLS results show that the liposomes increase in size as is expected if there is an increase in lipid exchange. The very drastic increase at the beginning of the DLS measurement are difficult to explain, but might be due to the presence of larger Indolicidin aggregates that are later dissolved and can then affect the liposomes causing them to increase in size. This increase is not very large, however, and is not maintained over time, so in that case the effect of Indolicidin is purely upon initial insertion. The system then perhaps recovers an equilibrium. The C_{14}-PEO liposomes with added Indolicidin actually seems more stable than the ones without. An explanation for this is the interaction Indolicidin has with C_{14}-PEO, thereby reducing the effect of the block co-polymer on the system.

The formation of a new structure from mixing Indolicidin and C_{14}-PEO is quite clear from the data. If Indolicidin inserts into the interface of the micelles as a surfactant this could cause the aggregation number to decrease which would explain why the new micelles are smaller than the pure micelles. The Indolicidin would also change the contrast in the micelles. No fits were accomplished with a simple micelle model including Indolicidin in the micelles, however, so this clearly does not fully account for the new aggregates. The observed interaction between the two components in itself makes C_{14}-PEO more or less useless in a model system: not only does it interfere with the peptides' mode of action on the model membrane, but to separate out any possible effect on the membrane would require extensive development of the model, where the interaction between the C_{14}-PEO and Indolicidin would have to be included. This not only requires a model to be developed and tested for the scattering seen in Figure 43, but it would also introduce several other free parameters making the fitting analysis more unstable.

The scattering from Indolicidin added to C_{14}-PEO stabilised liposomes do show a considerable effect on the system, but separating whether this is an effect of the interaction between C_{14}-PEO

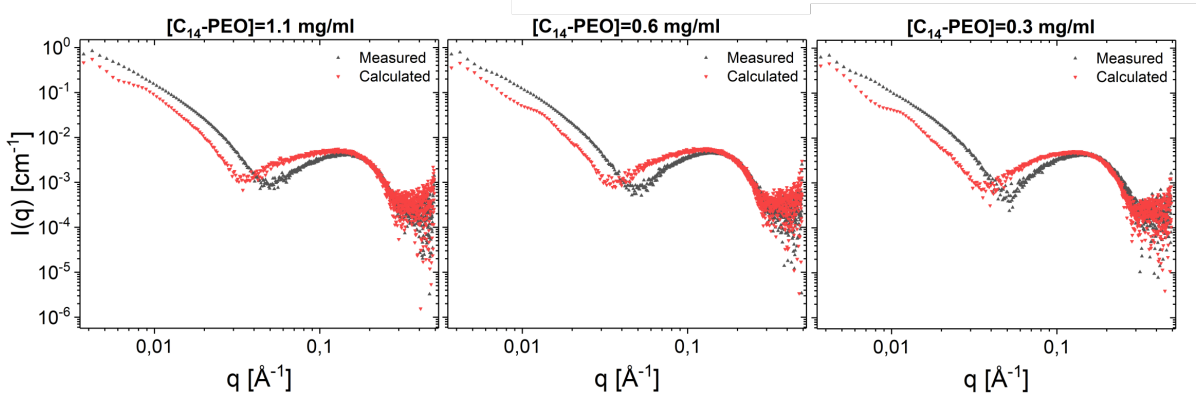

Figure 44: The measured scattering curves of liposomes (2.5mg/ml) with different concentrations of C_{14}-PEO (same as in figure35) and Indolicidin at a concentration of 0.7 mg/ml, corresponding to a molar ratio of $\approx$ 1:10 lipids:Indolicidin.

or the liposomes with Indolicidin is difficult. The changes can of course signify that the peptide is inserting into the membrane, and one might compare with the results in Section 4.4.4 and see that the results are rather similar. The C_{14}-PEO alone caused a shift in this minimum to lower q, however, so if the Indolicidin is causing C_{14}-PEO to be withdrawn from the liposomes or from the possible mixed micelles that were discussed in Section 4.3.1, we would perhaps expect to see that the minimum returned to its original value. The fact that the shift is similar for all concentrations of C_{14}-PEO supports the hypothesis that the peptide does insert, thereby having the same effect on all the different systems. One might argue that the peptide, only being tested at one concentration, might withdraw the same amount of C_{14}-PEO from each system, thereby causing the same amount of shift in scattering for all systems. Of course, the shift at intermediate q also occurs for the lowest concentration of C_{14}-PEO with Indolicidin, where there was not a very large difference with C_{14}-PEO alone (see for example Figure 36 in Section 4.3.2). Furthermore, at the lowest concentration, the C_{14}-PEO unimers have less aggregation together with Indolicidin, as seen from the SAXS results in Figure 43. This means that at least at the lowest concentration of C_{14}-PEO, the change in the scattering from the bilayer must be attributed to the effect of Indolicidin on the liposomes.

A summary of all the effects observed with C_{14}-PEO can be seen in Figure 45. Although the Indolicidin very likely does have an effect in the membrane of the liposomes, it would be difficult to create a model to quantitatively describe its effect separated from the effect of C_{14}-PEO on the liposomes and the Indolicidin. The scattering from possible mixed micelles and C_{14}-PEO-Indolicidin aggregates must then be accounted for. Accounting for all these effects would take considerable effort compared to the gain in the extracted information. This problem can be avoided by using PEGylated liposomes where the polymer chains are fully attached on the surface of the bilayers; the next section shows and discusses the results obtained from this system.

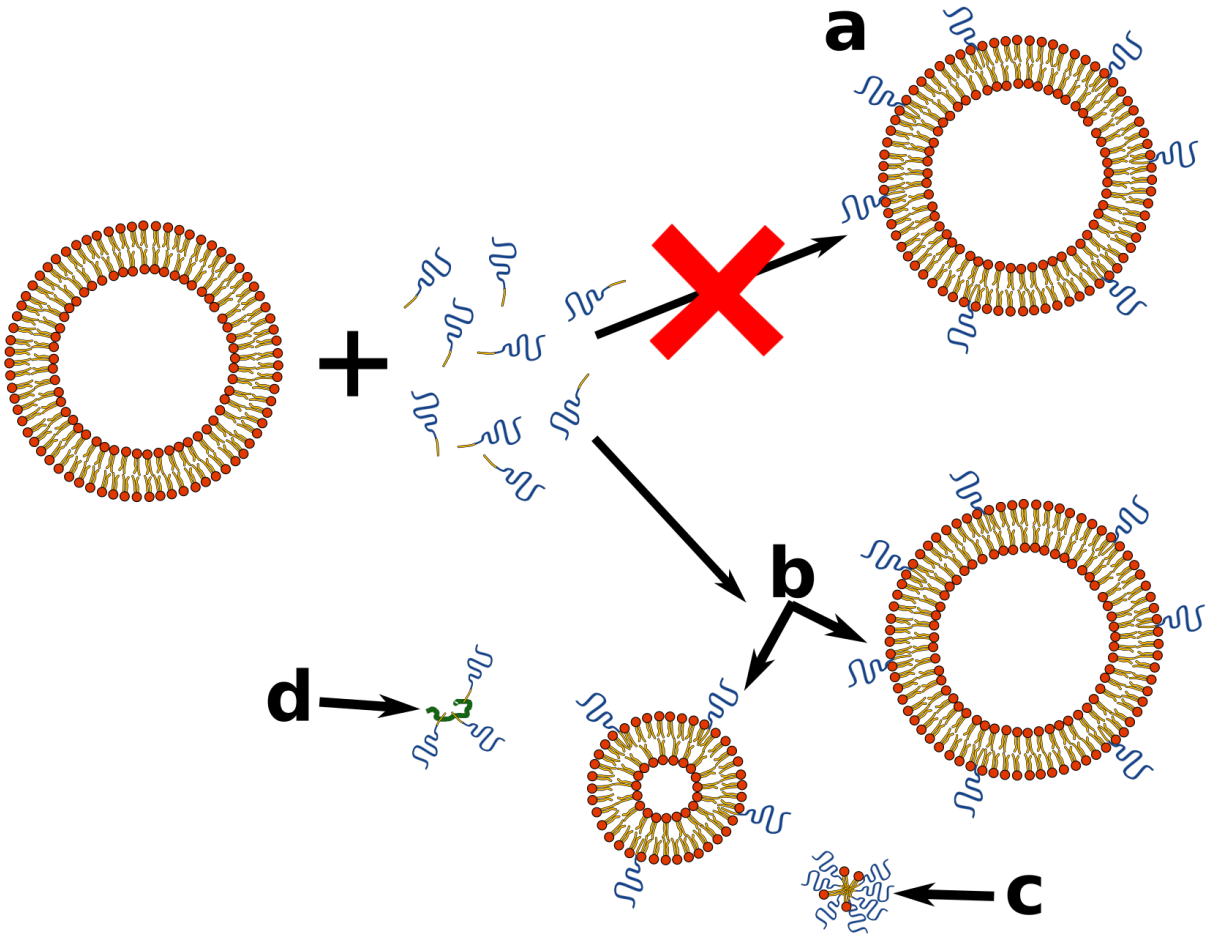

Figure 45: Summary of the results from the liposomal system sterically stabilised by C_{14}-PEO. The C_{14}-PEO did not merely add onto the surface as wanted, illustrated in **a**. The observations suggested at the C_{14}-PEO partially dissolved the liposomes, making a more polydisperse system of liposomes with surface-grafted C_{14}-PEO (**b**) as well as mixed micelles (**c**). The C_{14}-PEO was also found to interact with the Indolicidin (**d**). All of these extra effects are unwanted in a model system as they make the effect of the Indolicidin more difficult to discern.

4.4 Liposomes sterically stabilised by PEGylated lipids

As for the C_{14}-PEO stabilised liposomes, the liposomes that have been prepared with PEGylated phospholipids were tested for their kinetic stability using DLS and their effect on the melting of the bilayer using DSC. Since the PEGylated phospholipids are added together with the DMPC and DMPG in the preparation of the liposomes, the polymers are only in the liposome bilayers and not in solution. SAXS was used to study the microscopic effect of the modified phospholipids have in the bilayer. The effect of PEI and Indolicidin addition to the system was similarly investigated, and a model for the insertion of the peptide is proposed and tested on the scattering data.

4.4.1 The kinetic stability and lipid melting temperature of PEGylated liposomes

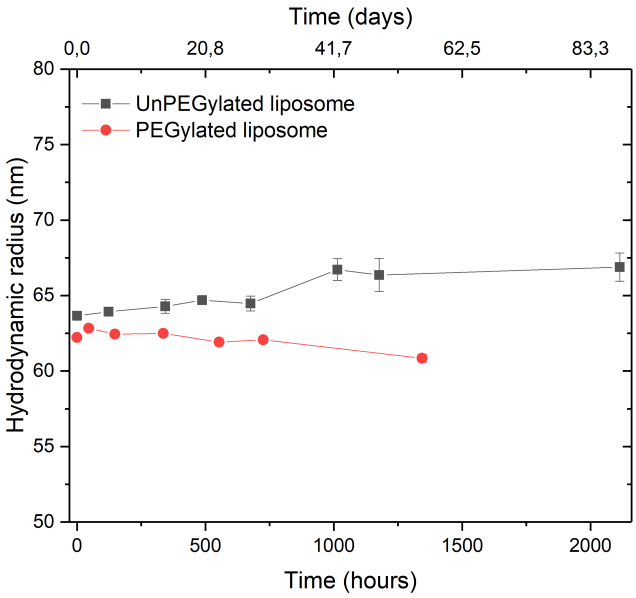

Figure 46: The hydrodynamic radius of PEGylated monitored over time with DLS compared with not-PEGylated liposomes. The PEGylated liposomes seem even more stable than the pure liposomes over time.

Determinations of the hydrodynamic radius of the PEGylated liposomes by DLS over time are depicted in Figure 46. These are compared to the unPEGylated liposomes from Section 4.1.1. The first measurement gave a hydrodynamic radius of 62.2 nm. The PEGylated liposomes are remarkably stable in their hydrodynamic radius over time, with the measurements varying by only about 1 nm throughout the monitored time. This makes the PEGylated liposomes, perhaps as expected, even more stable in size over time than the pure liposomes.

The PEGylated liposomes do not exhibit the same irregular trend in hydrodynamic radius as the C_{14}-PEO stabilised liposomes, but are instead very stable over time. This is a very important quality for when the effect of other additives are to be studied, because in contrast to the C_{14}-PEO stabilised liposomes where it was difficult to separate the interaction of the additives with C_{14}-PEO from the interactions of the PEI/peptide, any effect that PEI/peptide exerts on this system should be easily distinguished and be unequivocally attributed to the interaction of the PEI/peptide with the membrane.

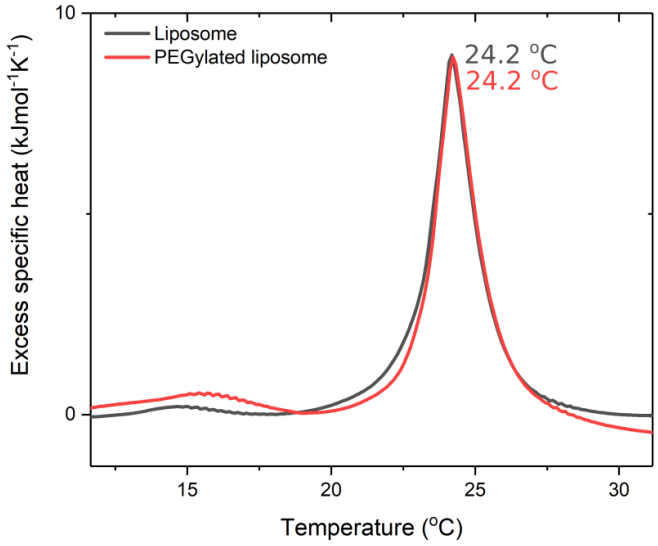

Figure 47: Calorimetric measurements of the PEGylated liposomes compared with the pure liposome. The PEGylation does not change the transition temperature of the bilayer or the enthalpy of the main transition (Table 6), but it does seem to have some effect on the pre-transition.

C_{14}-PEO concentration (mg/ml)	Pre-transition		Main transition	
	ΔH (kJ/mol)	T_m (°C)	ΔH (kJ/mol)	T_m (°C)
Pure liposome	0.7	14.7	20.3	24.2
PEGylated liposome	2.4	15.4	20.4	24.2

Table 6: The calculated transition enthalpies of the lipid bilayer at different concentrations of C_{14}-PEO

The results from the DSC measurement of the PEGylated liposomes can be seen in Figure 47, where it is compared with the measurement for the unPEGylated liposome from Section 4.3.1. The PEGylation does not change the melting of the bilayer from that of the pure liposome to any great extent. Table 6 shows the obtained melting temperature values and the calculated enthalpies of the two systems. The main transition is completely unaffected by the presence of the DMPE-PEG both in terms of the temperature and the enthalpy of transition. The PEGylation does seem to have some effect on the pre-transition; both an increase in the temperature at which it occurs and a change in its enthalpy is observed.

The PEGylated liposomes have been modified using DMPE-PEG, so any effect on the lipid melting temperature is due to the polymers on the surface since the hydrocarbon part of the phospholipid is identical to the DMPC and DMPG. The main transition was not changed from that of the unPEGylated liposome, which indicates that the packing of the lipids is not affected by the presence of the PEGylated phospholipids. Therefore, any interaction PEI/peptide has inside the bilayer should be the same as what it has in the unPEGylated bilayer. The change in the pre-transition is the same trend as that which was observed for the C_{14}-PEO stabilised system, further supporting the claim that this change is due to the presence of PEO on the surface making the transition to the ripple phase more energy demanding. Since it is then a matter of head group interaction rather than the actual packing of the lipids, it should not influence the activity of the PEI/peptide in the

bilayer.

Seeing that the PEGylated liposomes did not affect the kinetics nor packing of the bilayer, the next step was to see whether the model of Section 2.6.3 could describe the PEGylated liposomes.

4.4.2 Detailed structural analysis and quantitative data modelling

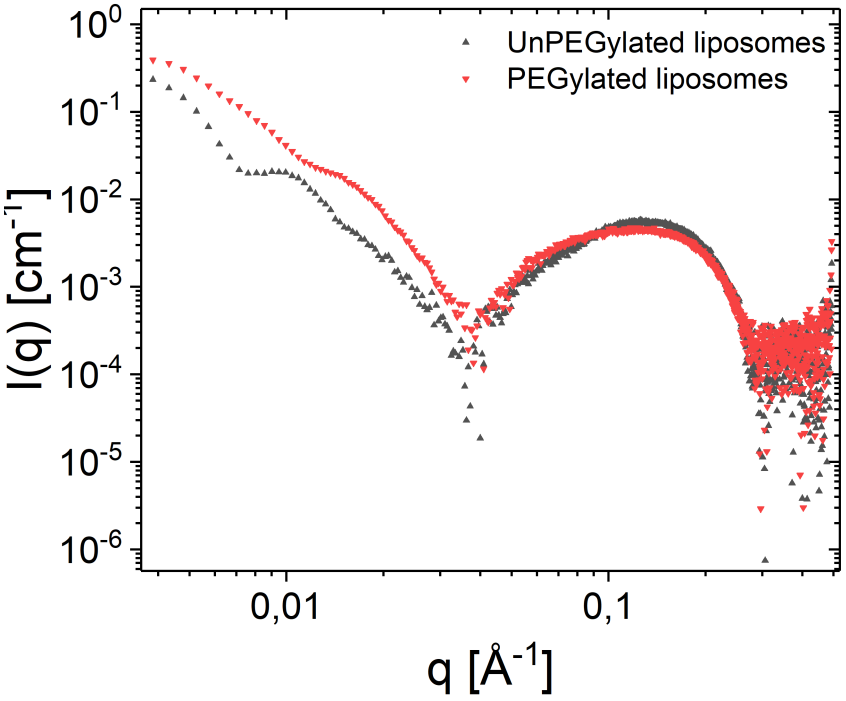

Figure 48: The scattering curve of the PEGylated liposomes with the unPEGylated DMPC-DMPG lipsomes.

A good description of the PEGylated liposomes was required for comparison with the later measurements where peptide is added to the system. Figure 48 shows the scattering curve of the PEGylated liposomes compared with that of the unPEGylated from Section 4.1.2. The main characteristics are conserved, but there are some important differences in the scattering. Importantly, the scattering minimum is at the same position, but the PEGylated liposomes show different curvature in the scattering curve on both sides of the minimum compared to the unPEGylated liposomes. We can see that the radius is slightly smaller and the polydispersity is slightly larger from the higher smearing of the spherical form factor oscillation at low q. Model fits to the data are required for more detailed information about the bilayer structure in the presence of the polymer. This also yields information on what conformation the polymer has on the surface.

The model in Section 2.6.3 was found to require a slight modification to describe the data accurately. R_{inner} and R_{outer} in expressions 61-65 were defined as

$$R_{\text{inner}} = R + z_{\text{PO}_4\text{X},i} - d_{\text{disp}} \tag{90}$$

and

$$R_{\text{outer}} = R + z_{\text{PO}_4\text{X},o} + d_{\text{disp}} \tag{91}$$

where d_{disp} is a displacement factor for the polymer chains. It adjusts for the fact that the starting point of the PEO-chains is not known to be at the position of the PO_4X-groups. The need for this displacement factor occurs due to the partial mixing of the polymer and the bilayer at the interface, similar to what has been reported for the corona and core block in co-polymer micelles [106] [107]. The fitting was performed in the same way as for the unPEGylated liposomes, using the values from the fit of Section 4.1.2 as a initial values. Additionally, asymmetric z_i-values were allowed and the d_disp was introduced as a new fit parameter. f_{PEO} was set to the added ratio of 2.5 %. R_g was set to 15 Å based on the results of Arleth and Vermehren [83]. All the values that were fixed in Section 4.1.2 were kept fixed here as well and the same constraints were implemented.

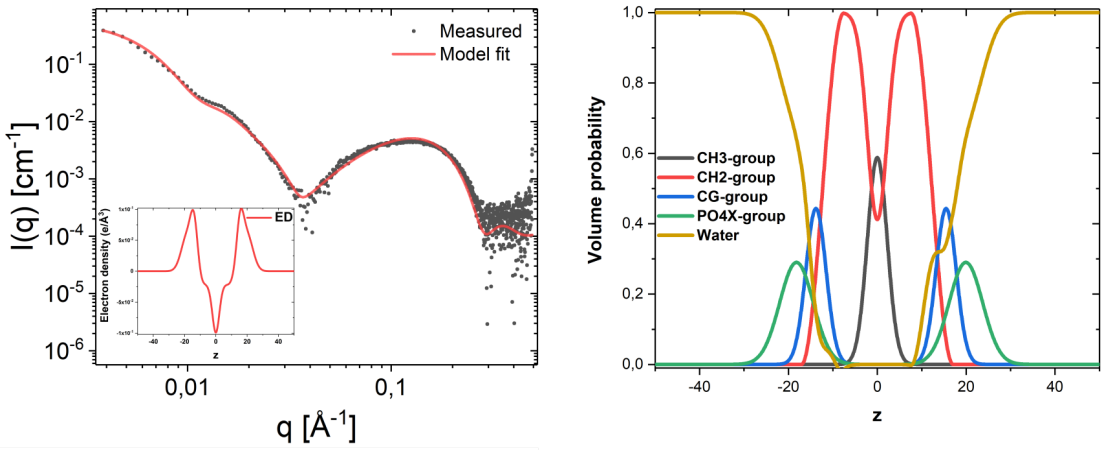

Figure 49: The scattering curve of the PEGylated DMPC-DMPG liposomes with a fit of the model described in Section 2.6.3 on the left. Inset shows the corresponding electron density (ED) profile. The volume probability profiles of the different phospholipid components are shown on the right. Fit parameters are listed in Table 7.

The fit to the adjusted model can be seen in Figure 49. The obtained fit parameters are listed in Table 7. The fit is in good agreement with the scattering data. The liposomes have a smaller radius, expected since this is defined by the bilayer and the PEO-chains are present on the liposomes during extrusion. The fit required the bilayer to be a bit asymmetric. Comparison the volume probability profile with that of the unPEGylated liposomes in section 4.1.2 reveals that the distribution of the lipid groups are the same as before in the inner leaflet, while the head group is further out from the hydrocarbon region than before. The distance between the tethered chains were calculated in the same way as for the C_{14}-PEO liposomes (equation 6.5) to give a distance of 51.1 Å, which is well outside the brush regime. The liposomes are also more polydisperse in radius - this is probably due to a variation of PEO-amounts in the different liposomes causing a difference in how each liposome is extruded.

The difference in the scattering curves of the PEGylated and the unPEGylated liposomes that we saw in Figure 48 can be accounted for by the addition of the scattering from the shell of PEO on both sides of the bilayer. The asymmetry of the PEGylated liposomes might due to the smaller radius of the liposomes themselves or due to the PEO-chains acting differently in the inner leaflet than the outer due to the environment - especially since they are found to be equally distributed on the inside as on the outside. This can be due to the contribution from the DMPE-PEG head groups, as these are allowed further out of the bilayer due to the solvation of the PEO-chain. The PEO-chains in the inner leaflet is more constricted in their extension, thereby not allowing the same for

Parameter	**Values**	**Fitted?**
Concentration	1.4 mg/ml $\pm$ 0.1mg/ml*	Yes
Radius	249 Å $\pm$ 10 Å*	Yes
Area	60.4 Å	No
$z_{\mathrm{CH_3}}$	0	No
$z_{\mathrm{CH_2,\ outer}}$	12.3 Å $\pm$ 0.2 Å	Yes
$z_{\mathrm{CH_2,\ inner}}$	-12.3 Å $\pm$ 0.2 Å	Yes
$z_{\mathrm{CG,\ outer}}$	15.5 Å $\pm$ 0.4 Å	Yes
$z_{\mathrm{CG,\ inner}}$	-13.8 Å $\pm$ 0.4 Å	Yes
$z_{\mathrm{PO_4X,\ outer}}$	19.9 Å $\pm$ 0.1 Å	Yes
$z_{\mathrm{PO_4X,\ inner}}$	18.2 Å $\pm$ 0.1 Å	Yes
$\sigma_{\mathrm{CH_3}}$	2.2 Å	No
$\sigma_{\mathrm{CH_2,\ outer}}$	4.8 Å $\pm$ 0.1 Å	Yes
$\sigma_{\mathrm{CH_2,\ inner}}$	4.8 Å $\pm$ 0.1 Å	Yes
$\sigma_{\mathrm{CG,\ outer}}$	2.3 Å $\pm$ 0.1 Å	Yes
$\sigma_{\mathrm{CG,\ inner}}$	2.3 Å $\pm$ 0.1 Å	Yes
$\sigma_{\mathrm{PO_4X,\ outer}}$	3.8 Å $\pm$ 0.1 Å	Yes
$\sigma_{\mathrm{PO_4X,\ inner}}$	3.8 Å $\pm$ 0.1 Å	Yes
D_B	36.9 Å	Derived
D_C	11.8 Å	Derived
$V_{\mathrm{CH_2}}$	25.59 $\mathrm{Å}^3$ §	Yes
f_{PEO}	0.025	No
f_{inner}	0.5	No
R_g	15 Å	No
d_{disp}	-12.0	Yes
σ_{SD} (Polydispersity)	0.3	Yes

Table 7: Obtained fit parameters of PEGylated DMPC-DMPG liposomes. A list of the full number of parameters with values used can be found in appendix. Asterix (*) denotes error that are estimated from fits as described in the appendix (Section 6.7). All other given errors are calculated from the relative error based on the standard deviation of the measurements in Table 2. §For the CH_2-values the error from both fits and replicates are less than 0.01 $Å_3$.

the inner DMPE-head groups. The radius of gyration for the PEO-chains is small, with an R_g=15 Å. This indicates that the PEO-chains in the PEGylated liposomes are more collapsed than the PEO-chains in the C_{14}-PEO stabilised liposomes. The PEO-block on C_{14}-PEO has a higher molecular weight than the PEO-block on DMPE-PEG, however, and so it is more difficult to perturb.

The scattering from the PEGylated liposomes can be fully accounted for by using the modified scattering model for PEGylated liposomes. We therefore have a well stabilised system without the issues encountered for the C_{14}-PEO stabilised liposomes, enabling us to describe changes in the scattering quantitatively. This paves the way for studying how addition of PEI/Indolicidin affects the stabilised system.

4.4.3 Addition of PEI

In order to test for any interactions between PEI and the PEGylated liposomes, DLS and SAXS measurements were performed similarly to what was done in Section 4.3.3 for the C_{14}-PEO stabilised liposomes. Figure 50 show the scattering curve of the PEGylated liposomes with added PEI.

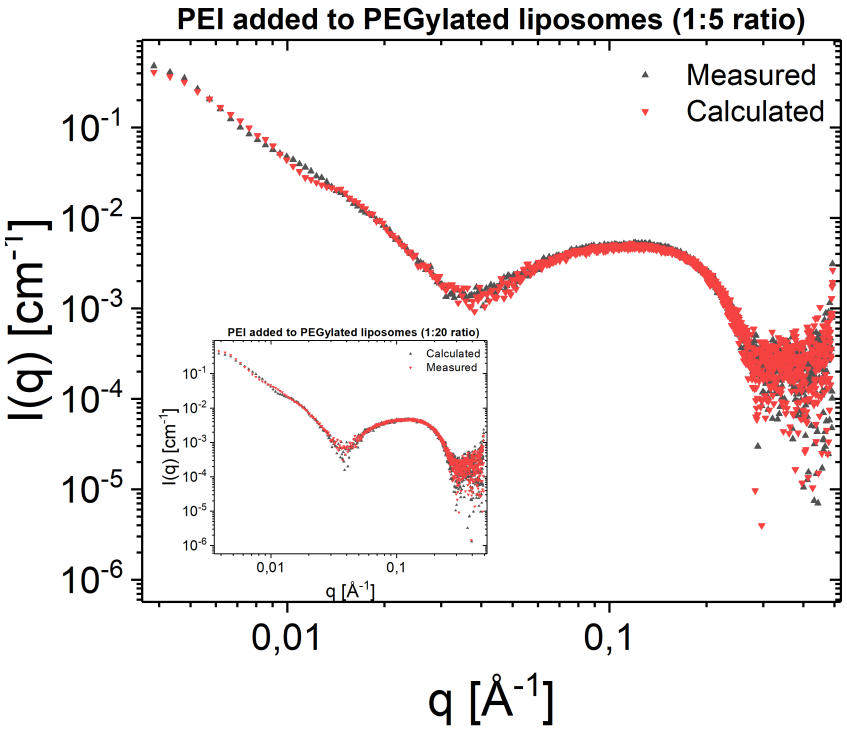

Figure 50: SAXS measurement results of PEGylated DMPC-DMPG liposomes with added PEI (1:5 PEI:lipid ratio). The measured scattering overlaps almost entirely with the calculated scattering, suggesting the PEI has no interaction with the PEGylated liposomes.

The addition of PEI to the PEGylated liposomes does not seem to affect the liposomal structure at all as the measured curve overlaps with the sum of the individual scattering curves. These results cannot be explained by any interaction with other structures as might be the case for the C_{14}-PEO stabilised liposomes. This further supports that the PEI actually does not have any effect in the C_{14}-PEO stabilised system as discussed in Section 4.3.3 as well. Likely, although their mechanism

for the induced aggregation is similar (due to their cationic charge), the mechanism for PEI-induced membrane disruption are quite different from those of Indolicidin.

4.4.4 Addition of Indolicidin

As previously tested for the C_{14}-PEO liposomes, the PEGylated liposomes were monitored for a size change due to Indolicidin. The DLS results show a drastic initial increase in radius after Indolicidin addition at 37 °C. The effect is much more clear than any of the fluctuations seen with the C_{14}-PEO system (Figure 33). The initial growth is the steepest, but the liposomes continues to grow over a long time period. In a previous experiment [108], we found that the solutions with Indolicidin phase separates after about 6 months, suggesting that the liposomes continues to grow in size until aggregation and phase separation occurs. This is in contrast to the PEGylated liposomes without Indolicidin, which were found to be completely stable over the same time period. It is worth noting that the peptide concentration in this experiment was very high, with a lipid:peptide ratio of about 1:2.5. The initial size growth also occurs for lower ratios, supported by the SAXS results discussed below as well as by other measurements from our group [108].

Qualitative inspection of the SAXS measurements of liposomes with Indolicidin compared with the calculated scattering in Figure 52 reveals a clear shift in the minimum at intermediate q of the scattering curve for several concentrations. This indicated a clear change in the bilayer scattering caused by the Indolicidin interacting with the membrane. A clear increase in both radius and polydispersity for the three higher concentrations is observed, supporting the results obtained from the DLS measurements above.

To obtain detailed information about the positioning of Indolicidin in the membrane, the scattering from the peptide had to be incorporated into the model for the bilayer. The peptide was modelled as another Gaussian function in terms of volume probabilities, and so included in equation 46 from Section 2.6.2 with i=peptide. The volume used to scale the Gaussian functions was averaged by the bound fraction of peptide, f_{peptide} to give a maximum probability height of

$$c_p = \frac{Vp \times f_{\text{peptide}}}{A \times \sigma_P} \tag{92}$$

A complicating factor, however, was that the peptides scattering length density contrast varies depending on whether the peptide is inserted into the hydrocarbon region of the bilayer or if it was in intercalated the head group region. We therefore weighted the contrast by the factor f_{Pt} that gives the fraction of peptide in the hydrocarbon region:

$$\Delta\rho = f_{Pt}\left(\rho_p - \rho_{CH2}\right) + \left(1 - f_{Pt}\right)\left(\rho_p - \rho_0\right) \tag{93}$$

f_{Pt} was found by calculating the integral of the overlap of the peptide Gaussian function with the volume probability function for the CH_2-groups. The problem is illustrated in Figure 53. This first required the intersect to be found between the two curves. The Brent-Dekker method [109][110] was therefore implemented in the fit function to numerically find the root of the function $P_{\text{CH}_{2_o}} - p_p$. With this root denoting the intersect, the integration was done from $z_p - 5\sigma_p$ to the intersect value

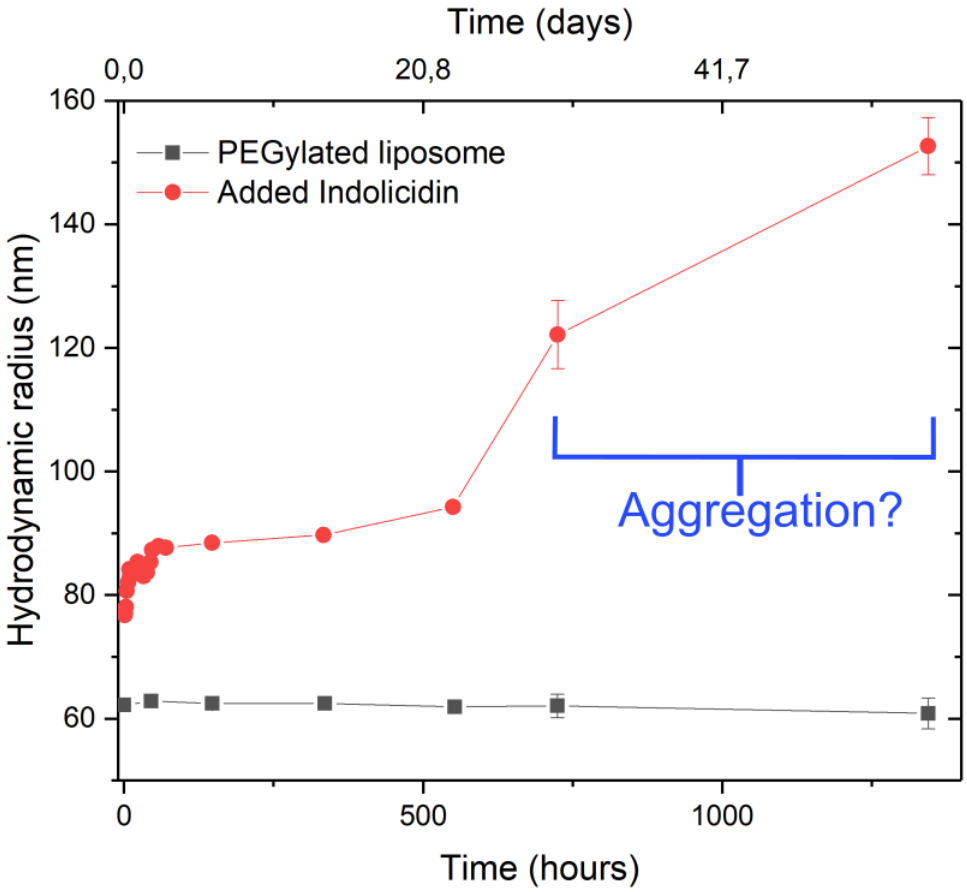

Figure 51: DLS measurements of PEGylated liposomes with and without Indolicidin over time. Based on the inspection of the autocorrelation and comparison of replicates in the last two data points, aggregation seems to have occurred, and therefore the analysed radius does not convey the size of the actual liposomes in this area. Note that the error bars for the PEGylated liposomes without Indolicidin were *multiplied by ten* to give some error bars that are visible in the plot. This was done to give a reasonable impression of the significance of the results of adding Indolicidin. Error was also calculated for the two last Indolicidin measurement, but these are not multiplied by ten, so the error is significantly larger here than for any measurements of the liposome without Indolicidin.

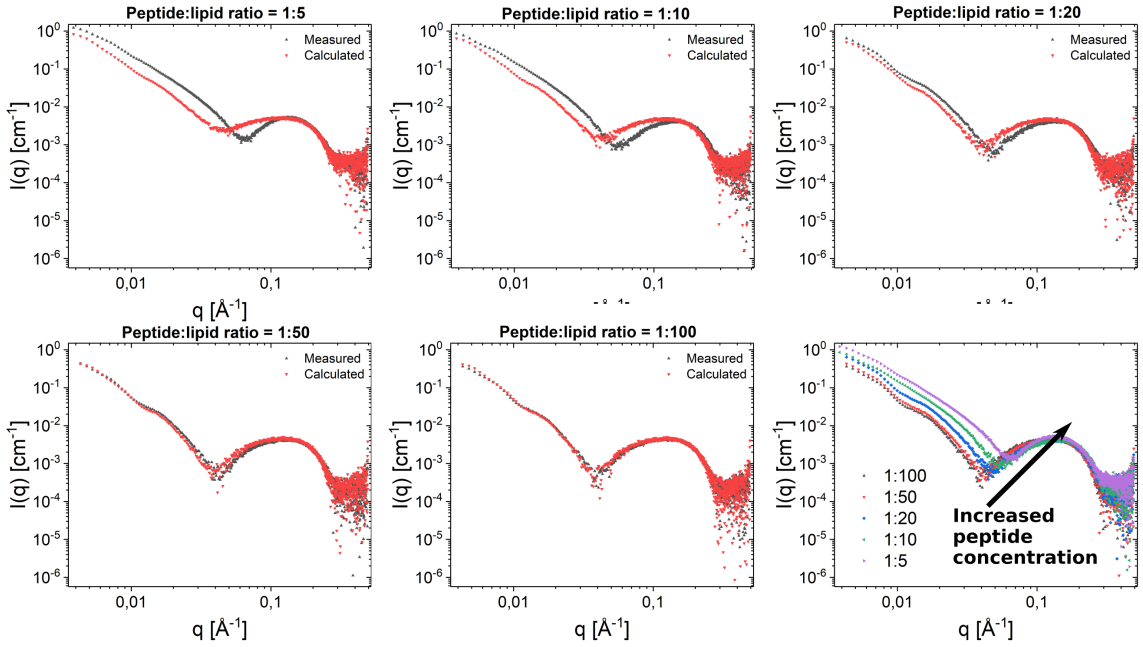

Figure 52: Results from SAXS measurement of PEGylated DMPC-DMPG liposomes with added Indolicidin. The measured scattering is very different from calculated scattering over the whole q-range, showing a very clear effect of the peptide on the liposomes both in terms of growth in size and changes in the bilayer. The effect becomes smaller with decreasing concentrations.

of z, $z_{\text{intersect}}$ over the peptide curve:

$$\int_{z_p-5\sigma_p}^{z_{\text{intersect}}} P_p = -\frac{C_p}{2}\sigma_p \operatorname{erf}\left(\frac{z_p - z_{\text{intersect}}}{\sqrt{2}\sigma_p}\right) + \frac{C_p}{2}\sigma_p \operatorname{erf}\left(\frac{5\sigma_p}{\sqrt{2}\sigma_p}\right) \tag{94}$$

and from $z_{\text{intersect}}$ to $z_{CH2_o} + \sigma_{CH2_o}$ for the CH_2-curve:

$$\begin{aligned}\int_{z_{\text{intersect}}}^{z_{CH2_o}+\sigma_{CH2_o}} P_{\text{CH}_{2_o}} = &\frac{2(K_1\left(z_{CH2_o}+\sigma_{CH2_o}\right)+K_2)+sin\left(2\left(K_1\left(z_{CH2_o}+\sigma_{CH2_o}\right)+K_2\right)\right)}{4K_1} \\ &+ \frac{2(K_1 z_{\text{intersect}}+K_2)+sin\left(2\left(K_1\left(z_{CH2_o}+\sigma_{CH2_o}\right)+K_2\right)\right)}{4K_1}\end{aligned} \tag{95}$$

with $K_1 = \pi/4\sigma_{CH2_o}$ and $K_2 = \pi(-z_{CH2_o} + \sigma_{CH2_o})/(4\sigma_{CH2_o})$. The two integrals were added to give the area where the two curves intersect. f_{Pt} is then defined as

$$f_{Pt} = \frac{\int_{z_p-5\sigma_p}^{z_{\text{intersect}}} P_p + \int_{z_{\text{intersect}}}^{z_{CH2_o}+\sigma_{CH2_o}} P_{\text{CH}_{2_o}}}{\sigma_p C_p} \tag{96}$$

since $\sigma_P C_P$ denotes the full area of the Gaussian function for the peptide volume distribution, following the definition in equation 47 in Section 2.6.2.

Fits of the model with peptide as described in this section can be seen in Figure 54. The fit parameters can be found in Table 13. The concentration denotes the lipid concentration from the fit of the liposome in Section 4.4.2 summed with the concentration of the peptide. The fraction of bound peptide was set equal to the peptide:lipid ratio, signifying that all the peptide inserts into the membrane. The values for the position of the lipid components were allowed to adjust by fitting,

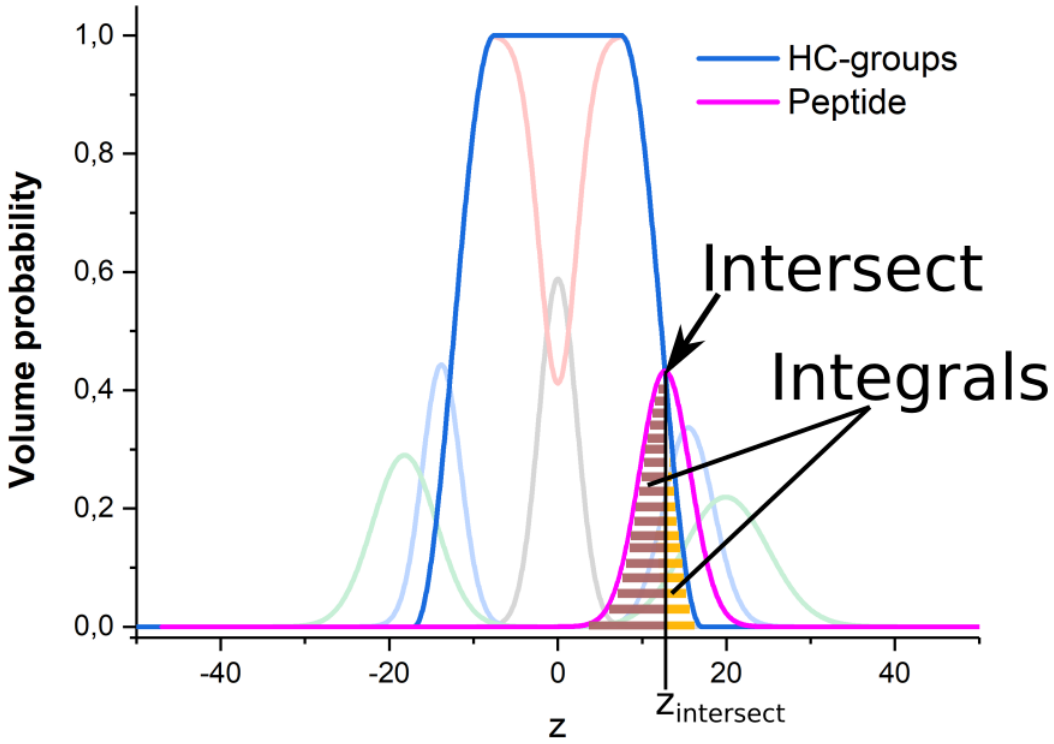

Figure 53: Illustration of how the fraction of peptide in the hydrocarbon region was found from the volume probability profiles. The two integrals are summed and divided by the integral of the entire peptide peak.

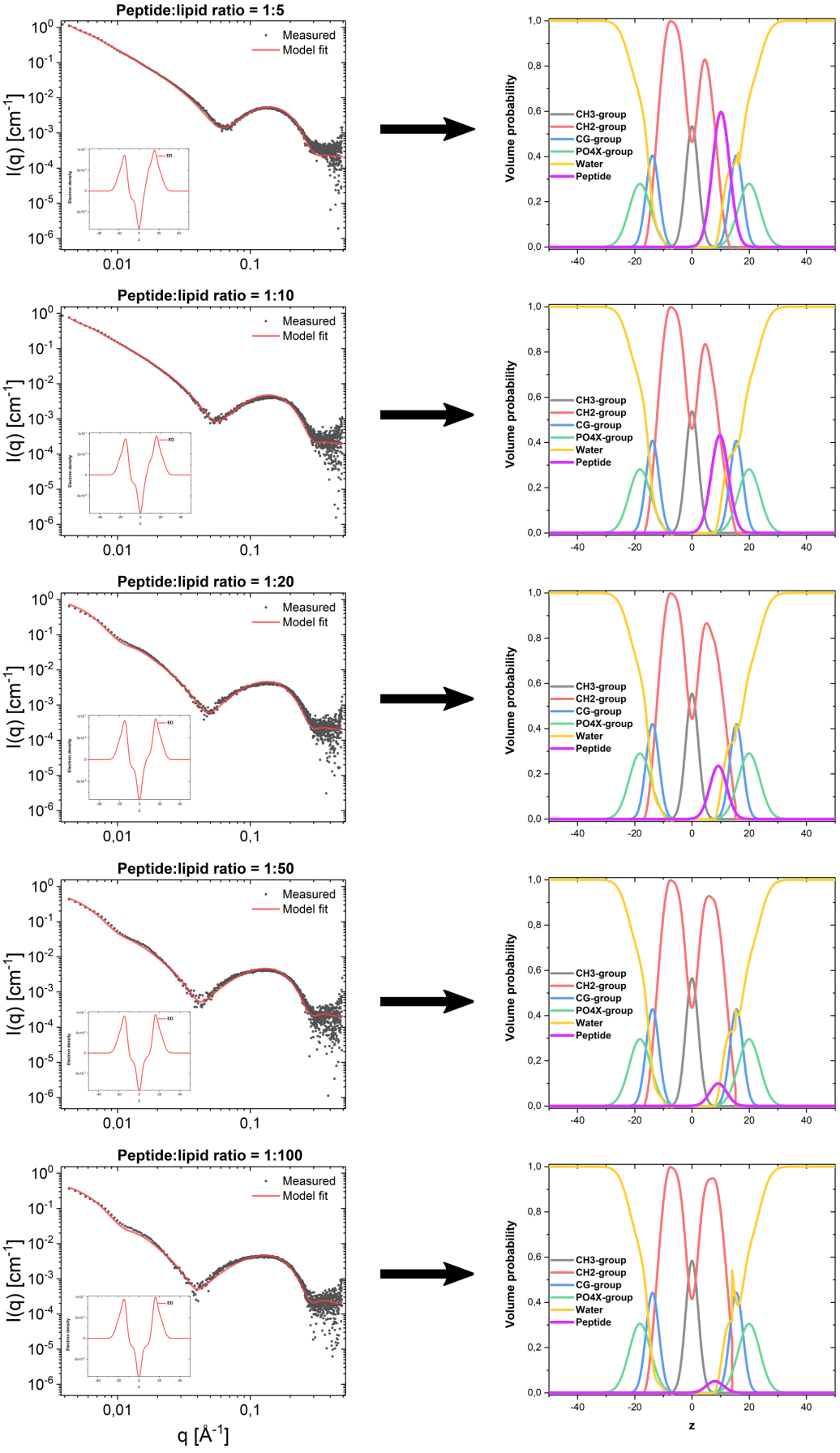

Figure 54: Fits of the model of Section 2.6.3 and 2.6.2 with the modifications as described in this section to SAXS measurements of the PEGylated liposomes with added Indolicidin. Fit parameters are listed the appendix (Section 6.6).

giving small deviations from the pure liposome values. No variation in their position was observed for the different peptide ratios from our fits. The radius, polydispersity and peptide location (z_P) constitutes the great changes between the liposomes with different fractions of peptide bound. The model fits confirm the qualitative observations - the radius increases more with increasing added peptide concentration as does the polydispersity. For the highest ratios (1:5 and 1:10), the radius is too large to be observed in this q-range. These values can therefore only be determined as having a radius above 400 Å. The polydispersity also increases, consistent with the idea that the peptide induces increased lipid exchange that increases both the average size and the distribution of sizes. The headgroup area is increased from that of the pure liposomes, which can be explained by the peptide insertion increasing the distance between the head groups some places in the membrane. From the volume probability distributions we see that the peptide is located mainly in the hydrocarbon region of the outer leaflet. The location shows a trend where it is found further out in the leaflet with higher peptide concentrations (see Table 13).

Both the DLS and the SAXS results support the hypothesis that the Indolicidin breaks up some of the liposome structure thereby inducing accelerated lipid exchange between liposomes, where the larger intact liposomes grows at the expense of the smaller ones due to their inherent larger stability. The proposed model is an excellent description of the data, and the fits confirm the observations from the DLS measurements. While the model does not account for any complex structures or the peptide to penetrate the inner leaflet, it still can fully account for interaction of the peptide with the bilayer in this case. The fits suggest that Indolicidin simply inserts into the hydrocarbon region and does not form any complex structure in the membrane. This insertion seems to be independent of concentration, although there is a slight variation of the average position in the bilayer. This might be explained by the bilayer becoming more distorted at higher fractions of peptide, which disallows the Indolicidin to penetrate as far in as at low concentrations. The simple insertion was expected from Indolicidin, which has a random coil formation in solution, but it goes against previous suggestions that the peptide forms distinct channels in the membrane [33]. No change in the curvature of the membrane is observed either; together this excludes most of the pore forming mechanisms suggested in the literature as illustrated in Figure 1 of the introduction. Although this is popularly suggested due to apparent increase in leakage across the membrane in presence of AMPs, this leakage could be an artefact of increased lipid fusion [111]. The growth in size found by DLS suggests that fusion of liposomes also happens in our case. Nor do the fits suggest that the peptide exert any effect such as membrane thinning and thickening, as has been suggested by molecular dynamics studies as well as atomic force microscopy measurements before [112]. Since the insertion into the hydrocarbon region of the bilayer is clear from the analysis, the antimicrobial activity is unlikely to stem from interactions with the phospholipid head groups. The results of the analysis in Figure 54 might suggests that the main effect of the peptide is something similar to that suggested in by Bechinger [13], where the peptide inserts in a wedge-like manner and disorders the packing of the hydrocarbon chains in the bilayer. Wimley [113] suggested a phenomenon they call "interfacial activity", where the peptide can partition into the bilayer thereby changing the packing of the lipids. This partitioning depends more on the physical chemical properties of the amino acids in the peptide rather than any specific structure the peptide takes up. The idea is that many of the other suggested mechanisms might fall under such a phenomenon. The results from the interaction of Indolicidin certainly fit within this perspective, with our analysis revealing the position of the Indolicidin partitioning in the bilayer.

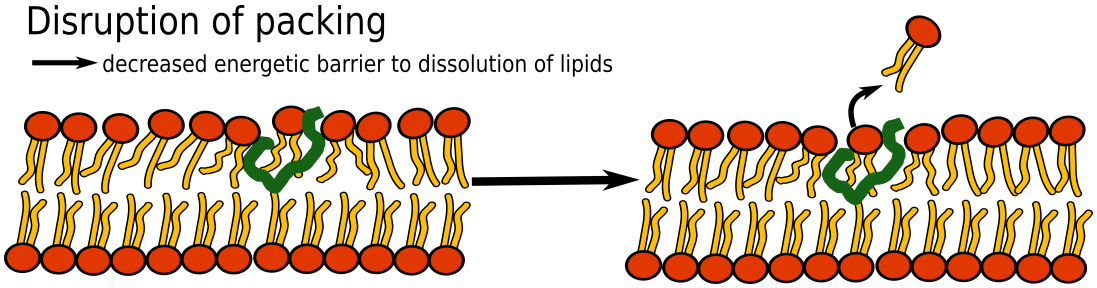

Figure 55: Illustration of the proposed interaction of Indolicidin in the membrane.

A common remark is that all the peptide ratios used in these experiments are quite high, and so does not represent viable *in vivo* ratios. Although one might think that such results therefore have no physiological meaning, it is of minor concern considering that we are interested in the basic mechanism of action of the peptides. In living organisms there are a number of complicating factors that are of much more significance for the antimicrobial activity than that of the peptide concentration. Any insight into how AMPs act, regardless of active concentration, is useful in the design of similar compounds. Melo et al. discusses the validity of the argument of the unphysiological character of using high peptide-to-lipid ratios in reference [114]. Their investigation shows that the actual peptide:lipid ratios in most minimum inhibitory concentration (MIC) assays, where the bacterial growth is monitored with addition of AMPs, are usually on the order of 2:1. The ratios used in this thesis are well below this, and so the argument of invalid ratios in itself is not of any concern.

The above modifications only allow the peptide to insert into the outer leaflet of the bilayer. The fact that the data were so well described by this simple model also shows a certain strength in both the validity of the original model as well as for the modification of it. The next step will of course be to implement the same logic as above for the inner leaflet, requiring tests for checking whether the inner or outer intersect should be found. One might also think that the peptide Gaussian could have a width that actually extended across the entire bilayer. As this was not found necessary for Indolicidin, however, it has not yet been implemented in the model.

Together, the SAXS and DLS measurements results suggest that Indolicidin disrupts the membrane by inserting and disrupting the packing of lipids in the bilayer, causing a destabilisation that allows the lipids to overcome the kinetic barrier of dissolution. This causes increased exchange between liposomes making them increase in size over time. For other peptides, further development of the model is probably necessary. Indolicidin illustrates that this simple implementation of the peptide in the model manages to account for the measurements and so provides a good basis for including further characteristics in the future.

4.5 Water transport across the lipid bilayer of the vesicle

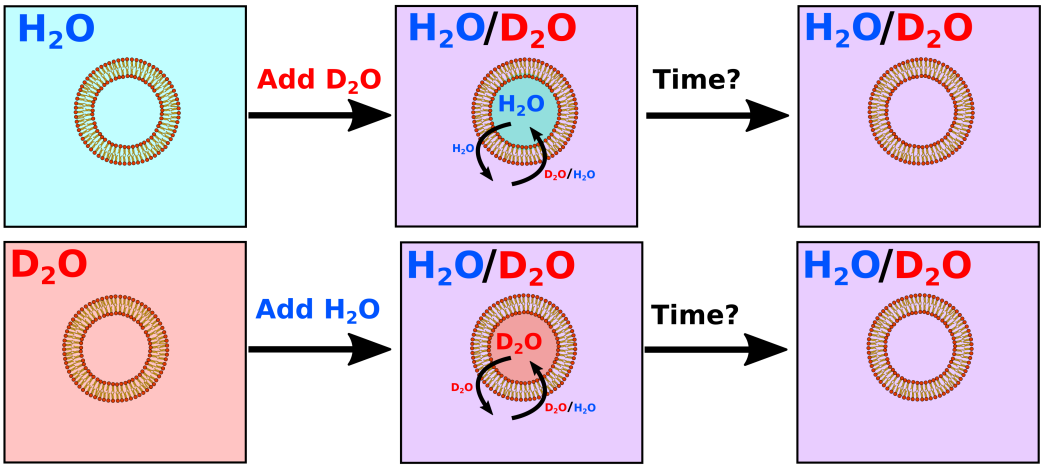

Figure 56: Illustration of the method for measuring the water transport with SANS.

If the antimicrobial peptides disrupt the membrane of liposomes the contents will to leak out of the interior, thus affecting the water transport across the membrane. Neutron scattering can be used to track such dynamic processes by contrast variation experiments. The appeal of using SANS to study the transport rather than other more established techniques measuring the diffusion is that it yields structural information about the bilayer at the same time. As discussed in Section 2.5, solutions of D_2O and H_2O scatter differently due to the different scattering lengths of deuterium and hydrogen, giving rise to different contrast with any solute such as our liposomes. The idea was to use this difference in contrast to study the time of water transport across the lipid bilayer. The approach used in this thesis is illustrated in Figure 56. Two liposome samples of the same lipid compositions were prepared separately in D_2O and H_2O. Right before measurement, the liposomes were mixed with equal volumes of H_2O and D_2O, respectively, so that the solvent on the outside of the liposomes was a 1:1 mix of the two. We have then created contrast between the interior and exterior of the lipsomes. This contrast is expected to disappear due to the water exchange leading to an equilibrium H_2O/D_2O composition that is equal on the inside and outside. By monitoring the scattering intensity over time we can monitor the loss of contrast in both samples. Each preparation was measured by SAXS as well to account for any structural differences that could cause the two scattering curves to differ even after they had reached the equilibrium water composition.

The measurements of water transport were performed on a number of different liposomes, listed in Table 8. Not only were liposomes of different compositions tested, but the size was also varied in case the curvature of the bilayer affects the permeability. The results from the measurements of the

Composition in mole fraction					**Diameter size (nm)**
DMPC	**DMPG**	**DMPE-PEG**	**Cholesterol**	**POPC**	
0.9	0.075	0.025	0	0	100
0	0	0.025	0.3	0.675	100
0	0	0.025	0.5	0.475	100
0	0	0.025	0.3	0.675	400

Table 8: Overview of the liposomes that were measured for the water transport experiment

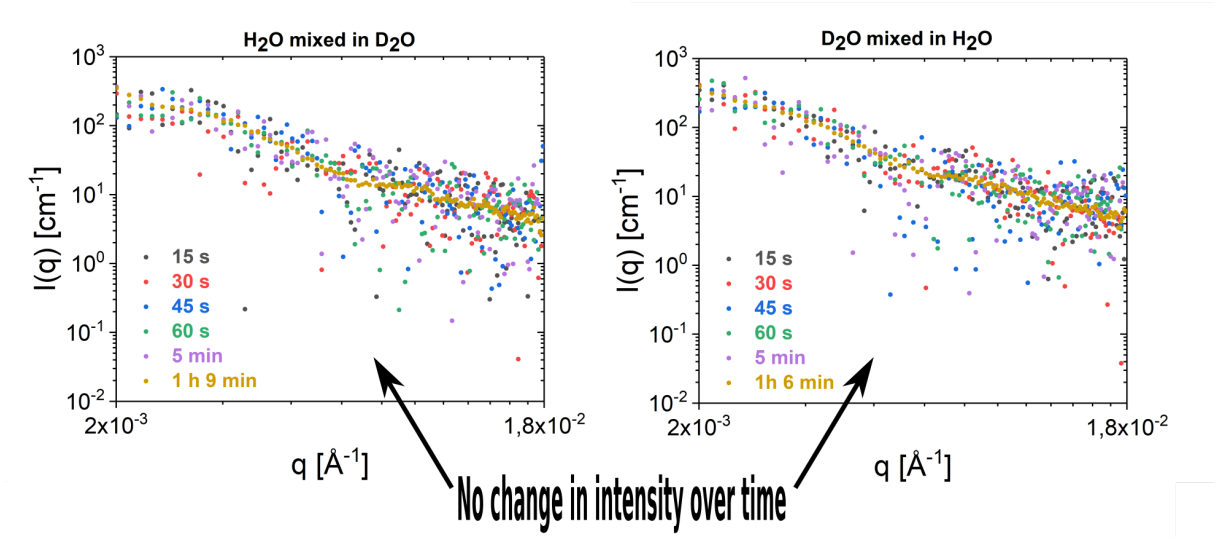

Figure 57: Figure shows measurement of liposomes prepared in D_2O and H_2O and then mixed with equal volumes of H_2O and D_2O, respectively, measured for 10 s at a time for 20 min and then again after 1 h. Since there was no change over this timescale, all measurements have not been included in the Figures. As we see in Figure 58 the scattering overlaps, so water transport has occurred faster than the timescale of the measurement. Note that the measurement after 1 h is taken over 20 minutes, while the first measurements are only for 15 s each, giving the large difference in statistics for these measurements.

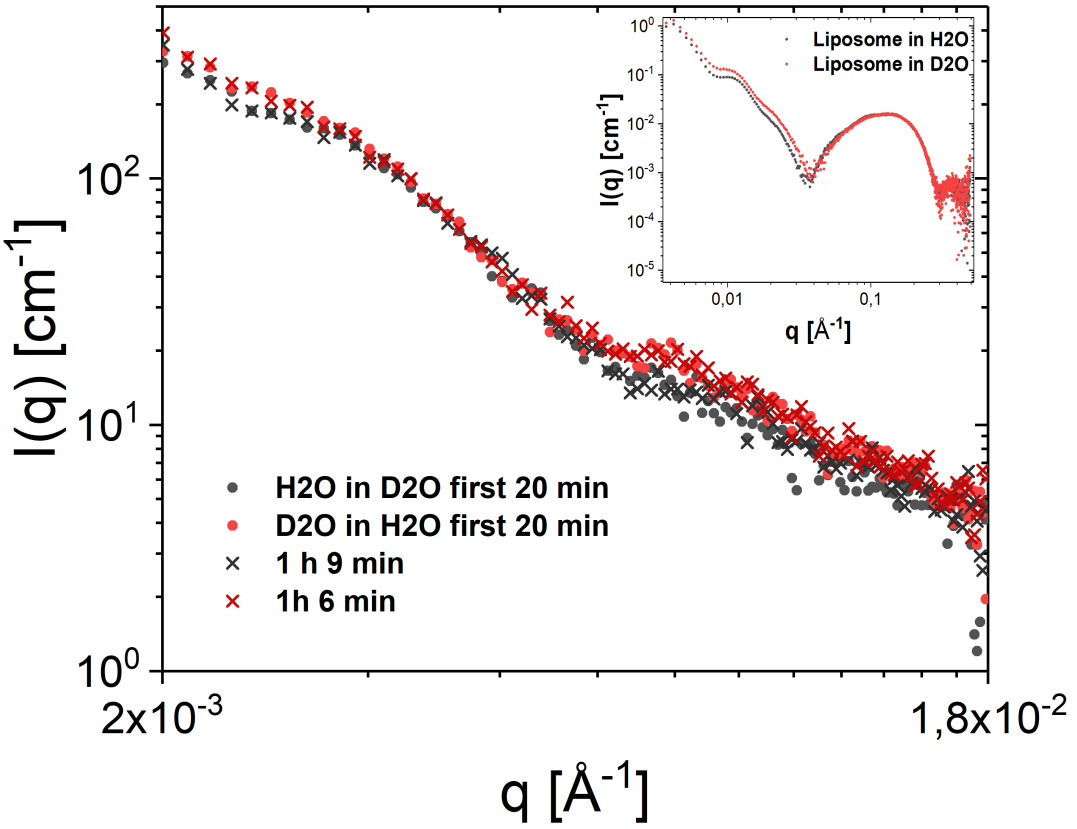

Figure 58: SANS measurements of the liposomes prepared in D_2O and H_2O and then mixed with equal volumes of H_2O and D_2O, respectively, do not completely overlap, but as the SAXS measurements in the inset shows, this is due to structural difference in the liposomes and not due to differences in the D_2O/H_2O content.

PEGylated DMPC-DMPG liposomes can be seen in Figure 57. These graphs display the scattering at different time points from the time of mixing for the sample prepared in H_2O mixed with D_2O and vice versa. There is no observable difference in the two scattering curves. The result is more clear in Figure 58 where the data from the first 20 minutes for both samples are merged to give better statistics. This shows that the two scattering curves do not completely overlap. The SAXS measurements performed on the same samples show that this is due to structural differences and not due to the different contrast of the liposome exterior and interior. One of the samples seems to have liposomes of slightly greater radius. The scattering does not evolve over time either; the scattering curves obtained 1 hour after mixing completely overlap with the original measurement on the sample.

Previous results from measurements on DPPC-DPPG liposomes performed at Institute for Energy Technology (IFE; see appendix) suggested that the PC/PG-based liposomes were anyway completely permeable to water. The same conclusion is reached from the measurements of our PEGylated DMPC-DMPG liposomes. This means that complete water exchange between the inside and outside of the liposomes has already occurred before the first measurement was finished. This confirms previous results measuring the diffusion of tritiated water across thin lipid bilayers reporting water diffuses quite fast, although measurably, across this semi-permeable membrane [115].

Although the PEGylated DMPC-DMPG liposomes were the ones that have been the main focus in this thesis, POPC-Cholesterol liposomes were of interest for future work, being a mimick of the mammalian cell membrane. These lipids can be seen in Figure 59**d)**. It was interesting to investigate if any transport was observable with the liposomes containing cholesterol, as cholesterol is known to make the membrane more mechanically stable, thicker, and less leaky while still maintaining its fluidity [116][117]. This due to the stabilisation by cholesterol of the so called liquid-ordered phase of the bilayer. The low water permeability of lipid bilayers with a cholesterol level exceeding 20 % has been reported by other sources [118][119]. It was therefore interesting that all the various compositions and sizes gave the same results as with the DMPC-DMPG-liposomes. As seen in 59 **a)** and **b)** there is again no change in the scattering over time. In **c)** we see that there is a difference in the scattering pattern of the different preparations of liposomes, but this is again due to structural differences as seen in the inset. The same results were obtained for all the different tested liposomes, and therefore the rest of the data are not presented in this thesis.

Overall, studying the water transport using neutron scattering does not seem feasible for any ULVs as the time scale of these measurements are much to long compared to the timescale of the transport. The water is almost free to move across the membrane, so even if the peptides were to permeate the membrane are not be able to see this by increased water transport. Our results confirm previous studies using diffusion of tritiated water and osmotic measurement that have also found that the passive transport of water is very quick [115] [119]. It is worth noting that since the liposomes have the exact same composition of solute on the inside as outside, there is no osmotic pressure across the membrane. Therefore a mere increase in water transport is not expected to rupture the liposome in itself. This is in stark contrast to living cells, that have an exceedingly different environment inside and outside the plasma membrane. Although this method of measuring water transport is not feasible with a reactor as a neutron source due to the long collection time, similar experiments can possibly succeed using the high peak flux of spallation sources in the future.

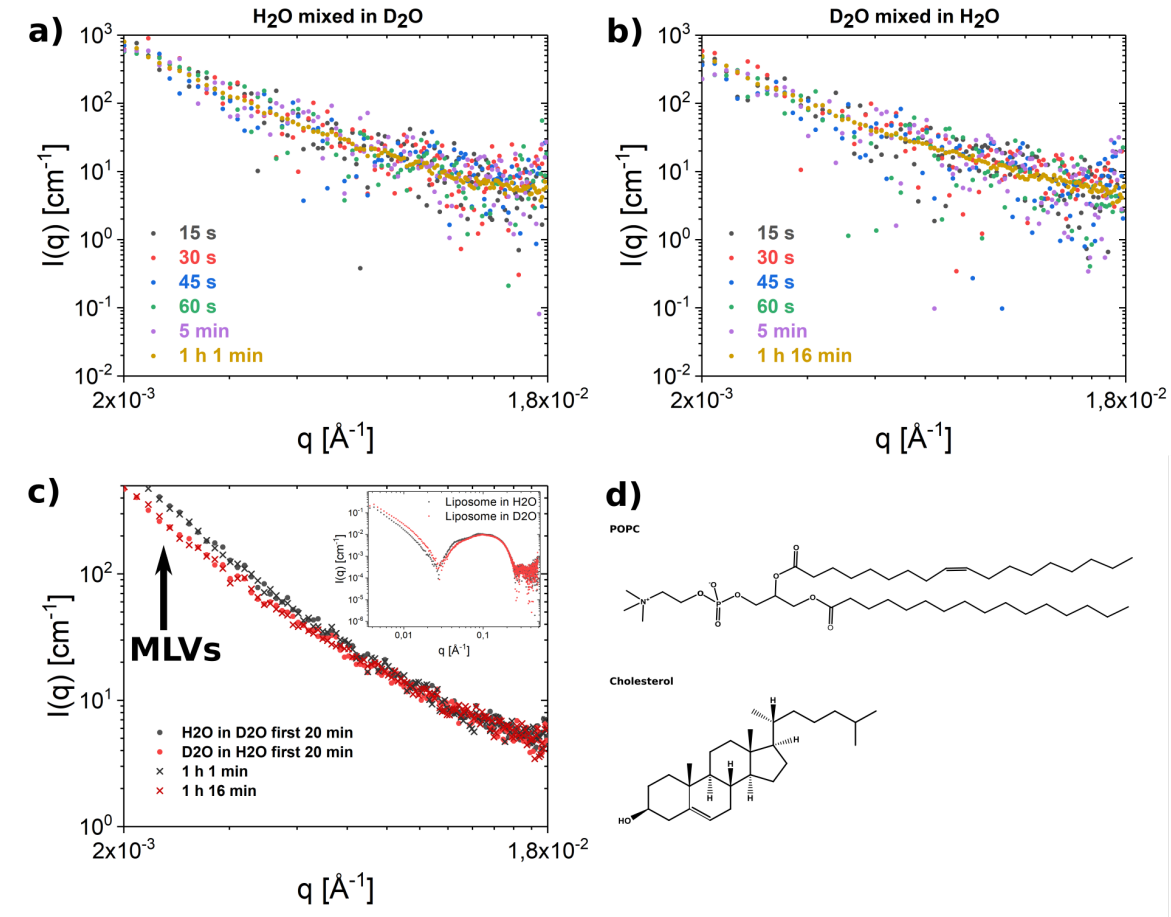

Figure 59: SANS measurements of cholesterol-POPC liposomes (400 nm diameter) prepared in D_2O and H_2O and then mixed with equal volumes of H_2O and D_2O, respectively, do not completely overlap, but as the SAXS measurements in the inset show, this is due to structural difference in the liposomes and not due to differences in the D_2O/H_2O content. The scattering pattern from both the SANS and SAXS measurements shows a clear presence of multilamellar vesicles in the H_2O sample.

5 Conclusion and outlook

The goal of this thesis was to develop a liposomal system that can be used to investigate the mechanisms of action for AMPs using small angle scattering techniques. Both liposomes stabilised with C_n-PEO and PEGylation was tested in terms of their effect on the kinetic stability of the liposomes as well as their effect on the structure of the bilayer. Analytical models were developed and tested for their capability of describing the small angle scattering data from the system. From these results the PEGylated liposomes was shown to be the better of the two options for studying the interaction of the tested AMP, Indolicidin. The analytical models fully accounts for the insertion of the peptide in the bilayer. Finally, the water transport across the bilayer was measured using SANS. This proved that the transport is too fast to be observed with the current measuring times.

The two types of steric stabilisation tested in this project turned out to be quite different in their effect on the system. The C_{14}-PEO was found to clearly insert into the bilayer and thereby probably provide a steric barrier against peptide-induced aggregation. For low concentrations the C_{14}-PEO insertion was very well explained by the analytical model developed in this thesis. The systems with concentrations above the critical micellar concentration of the block co-polymer could not be explained fully by the model and the C_{14}-PEO was found to have further interactions in the system as well. It was found by dynamic light scattering and differential scanning calorimetry measurements that C_{14}-PEO was possibly forming mixed micelles with the lipids and thereby partially dissolving the bilayer, giving a kinetically unstable system. The C_{14}-PEO also seemed to interact with the AMPs themselves, yielding results that were not easily predicted or modelled.

In contrast, the PEGylated liposomes provide a system that is even more stable over time than the unmodified liposomes. The PEGylation stabilises the liposomes against aggregation without modifying the internal bilayer structure significantly and the attached polymer chains do not seem to prevent the AMPs' interaction with the membrane either. The proposed analytical model accounted for the presence of the PEO-chains on the liposomes. The polymer chains were found to be in a collapsed form on the bilayer, and possibly having further interactions with the bilayer surface. These effect should be further explored as they have implications for other applications of PEGylated liposomes as well. With the successful stabilisation using PEGylation, it might be relevant to try other more biologically relevant stabiliser, such as lipopolysaccharides (LPS) which are found in Gram negative bacteria. This could yield information on possible effects the LPS has on the mechanism of AMP through comparison with the PEGylated liposomes.

PEI was found to not interact with either C_{14}-PEO liposomes nor PEGylated liposomes, suggesting that its interaction with the membrane is quite different from that of Indolicidin, which shows a clear effect in the membrane from SAXS measurements. Indolicidin insertion was accounted for by the developed analytical model, where it was found to insert into the hydrocarbon region of the outer leaflet. This suggests that the mechanism of action of Indolicidin in the membrane is simpler than what has been suggested before, with its insertion disturbing the lipid packing and thereby destabilising the kinetics of the liposomes. The successful description of this interaction does open the possibly of further development of this model that could give more insight into mechanism of different peptides. Testing with several antimicrobial peptides that have different chemical properties could both give insight into possible differences in the mechanisms, and thereby give clues to how the model might be further improved.

It is worth noting that the fact that both the insertion of C_{14}-PEO and Indolicidin into the membrane could be accounted for by the scattering model for PEGylated liposomes with only relatively simple modifications also strengthens the validity of the original model. Although the exact determined values of the bilayer may differ slightly across replicates, the ability of the model to predict changes in the bilayer is quite apparent from this study. The model is therefore very successful in achieving one of the main goals of this thesis which was to develop a system where the effect of AMPs in the membrane can be described quantitatively from the scattering data.

While SANS would have provided an excellent method for yielding information on the transport of water across the bilayer alongside structural changes, the experiment showed that water transport is fast well beyond the time-resolution of the SANS measurements. It could therefore not be observed for any of the liposomal systems tested. These results were particularly interesting for liposomes containing cholesterol as it has been assumed that this molecule makes the membrane much more impermeable when it is present in higher amounts. Other methods are therefore required for studying any permeation effects of antimicrobial peptides. This can for example be to use the transport of ions or small organic molecules. One might consider that with the new spallation sources SANS can still turn out to be a useful technique in studying the transport of small molecules simultaneously as it yield structural information.

SANS can also provide important insight into the lipid dynamics caused by AMPs that was observed in this thesis. Using deuterated and hydrogenated lipids, one can visualise the lipid exchange between liposomes, and therefore the effect of Indolicidin on the lipid dynamics. This could further support the DLS and SAXS results showing an increase in the size of the liposomes upon Indolicidin addition and confirm that this is due to increased lipid exchange. Such experiments are already being performed to confirm the observations and proposed mechanisms presented in this thesis. New advances within molecular dynamics simulations can give predictions about the dynamics of the liposomal system both alone and with peptide, giving even better models to test the experimental data up against in the future.

6 Appendix

6.1 Materials and Equipment

Ethanol (99.96 %) from VWR.

Methanol (99.9 %) from VWR.

Chloroform (99.3 %) from VWR.

Trizma base from Sigma Aldrich.

Trizma HCl from Sigma Aldrich.

1,2-dimyristoyl-sn-glycero-3-phosphocholine (14:0 PC (DMPC)—850345) from Avanti Polar Lipids, Inc. 1,2-dimyristoyl-sn-glycero-3-phospho-(1'-rac-glycerol) (sodium salt) (14:0 PG—840445) from Avanti Polar Lipids, Inc.

1,2-dimyristoyl-sn-glycero-3-phosphoethanolamine-N-[methoxy(polyethylene glycol)-2000] (ammonium salt) (14:0 PEG2000 PE—880150) from Avanti Polar Lipids, Inc.

1-palmitoyl-2-oleoyl-sn-glycero-3-phosphocholine (16:0-18:1 PC—850457) from Avanti Polar Lipids, Inc.

1,2-dipalmitoyl-sn-glycero-3-phosphocholine (16:0 PC (DPPC)—850355) from Avanti Polar Lipids, Inc.

1,2-dipalmitoyl-sn-glycero-3-phospho-(1'-rac-glycerol) (sodium salt) (16:0 PG—840455) from Avanti Polar Lipids, Inc.

Mini Extruder from Avanti Polar Lipids, Inc.

PC Membranes $0.1\,\mu m$ and $0.4\,\mu m$ (610005 and 610007) from Avanti Polar Lipids, Inc.

Filter Support (610014) from Avanti Polar Lipids, Inc.

C_{14}-PEO synthesised by Lutz Willner, Forschungszentrum Jülich GmbH.

C_{12}-PEO synthesised by Lutz Willner, Forschungszentrum Jülich GmbH.

Polyethylenimine, linear (average Mn 2,500, PDI ¡1.2) from Sigma Aldrich.

Indolicidin synthesised by Isca Biochemicals.

Some figures have been created with a basis in different images from the gallery of Mariana Ruiz Villarreal on Wikimedia Commons.

All illustrations that don't specifically say differently were made using the open source Inkscape software package.

Plotting of all graphs and analysis of DLS data was done using the Origin software (OriginLab, Northampton, MA).

Analytical scattering models were programmed and fitted using the QtiKWS software developed by Vitaliy Pipich [95].

DSC data were analysed using the NanoAnalyze software from TA instruments.

6.2 Effect of radius and polydispersity on scattering of liposomes

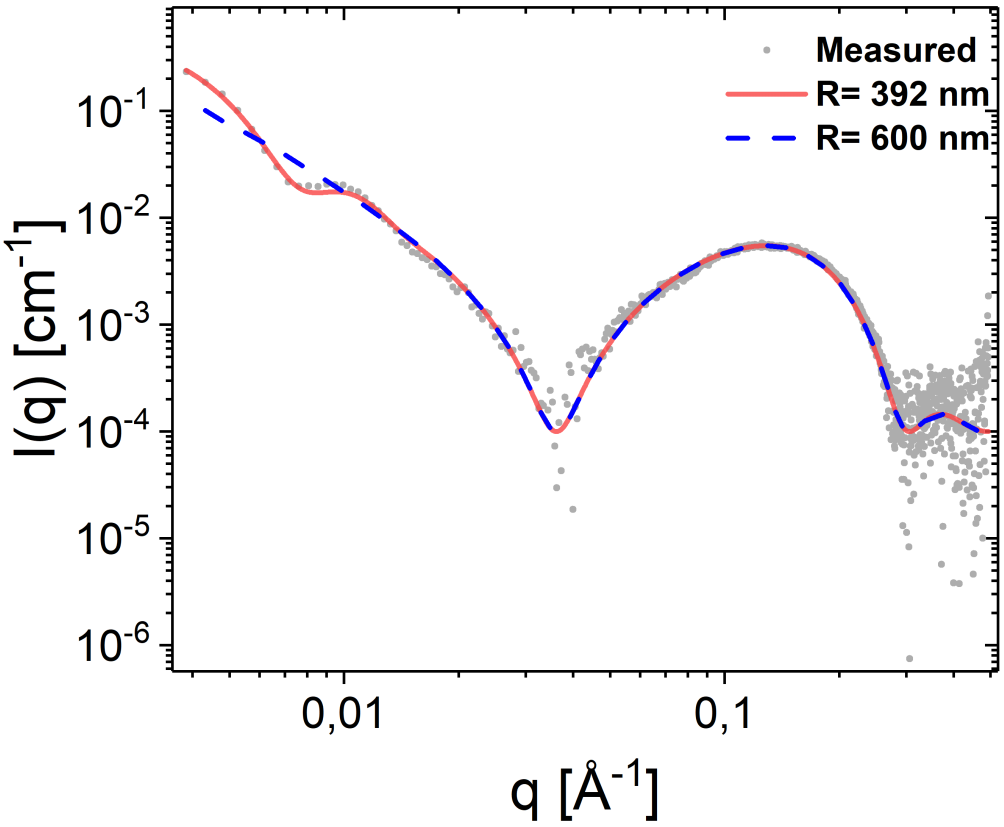

Figure 60: The Figure shows the effect of increasing the radius (from 392 nm to 600 nm) and polydispersity on the model scattering curve. The two curves overlap at high and intermediate q-values and only differ at low q. This confirms the validity of the method of separated form factors as discussed in Section 21.

6.3 Determination of highest possible concentration for usage in DLS

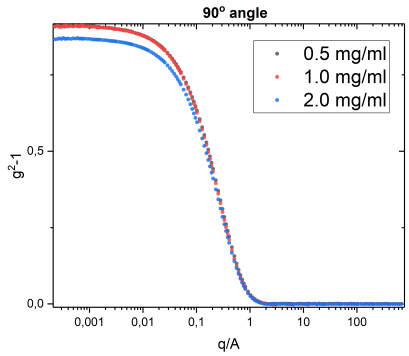

Figure 61: The scattering at the 90 °angle for 3 different concentrations shows that multiple scattering occurs at concentrations above 1mg/ml. The 90 °angle was used because it is the least sensitive to the presence of dust in the sample.

The concentration in DLS cannot be too high due to multiple scattering at the higher concentration. The small angle scattering techniques, however, generally require higher concentrations for good data collection. Since we wanted to use similar conditions for the two techniques, different concentrations were tested for the occurrence of multiple scattering with DLS. It was found that a concentration of 1 mg/ml was the highest possible. Figure 61 shows that the scattering for 1 mg/ml overlaps with the 0.5 mg/ml concentration which is known to not have multiple scattering, while the concentration above did not. The 1 mg/ml concentration was therefore picked, although this concentration is too low to be used for collecting data on the local SAXS instrument, and therefore simultaneous measurements with DLS and SAXS on the same samples were not possible.

6.4 Full list of fit model parameters

Parameter	Values	Fitted?
P	13	Yes
R_m	77 Å	Yes
ρ_{solvent}	9.43E10 cm^{-2}	No
σ	0.1	No
R_g	32 Å	No
$\hat{\nu}$	7	Yes
d_f	1.7	No
ρ_{coreN}	9.436E10 cm^{-2}	No
ρ_{shellN}	1.11E11 cm^{-2}	No
x	1.33333	No
f_{core}	1	No
V_{cpN}	285.5 cm^3/mol	No
V_{spN}	1377 cm^3/mol	No
A_2	0,0057473	Yes
σ_{int}	5	No
Concentrations	0.1/0.2/0.3/0.6/1.1/2.2/4.5 mg/ml	No
d_{sp}	1.2 g/cm^3	No
d_{cp}	0.8 g/cm^3	No
M_{sp}	4965 g/mol	No
M_{cp}	228.4 g/mol	No
d_{solvent}	1 g/cm^3	No
$R_{G_{\text{chain}}}$	35 Å	No
f_{uni}	1	No
CMC	0.47 mg/ml	Yes

Table 10: Fitting parameter from model fit to C_{14}-PEO at 37 °C

Parameter	**Values batch 1**	**Values batch 2**	**Fitted?**
Concentration	1.6 mg/ml	1.4 mg/ml	Yes
Background	1E-4	2E-4	No
R	392 Å	420 Å	Yes
area	60.4 Å	60.4 Å	Yes
$z_{\mathrm{CH_3}}$	0	0	No
$z_{\mathrm{CH_2}}$	12.3 Å	12.0 Å	Yes
z_{CG}	13.8 Å	13.4 Å	Derived
$\delta_{z_{\mathrm{CG}}}$	1.5 Å	1.4 Å	Yes
$z_{\mathrm{PO_4X}}$	18.3 Å	18.4 Å	Derived
$\delta_{z_{\mathrm{PO_4X}}}$	4.4 Å	5.0 Å	Yes
$\sigma_{\mathrm{CH_3}}$	2.23 Å	2.23 Å	No
$\sigma_{\mathrm{CH_2}}$	4.8 Å	4.6 Å	Yes
σ_{CG}	2.3 Å	2.2 Å	Yes
$\sigma_{\mathrm{PO_4X}}$	3.8 Å	3.8 Å	Yes
$\rho_{\mathrm{CH_3}}$	5.10378E10 $\mathrm{cm^{-2}}$	5.10378E10 $\mathrm{cm^{-2}}$	No
$\rho_{\mathrm{CH_2}}$	8.80119E10 $\mathrm{cm^{-2}}$	8.80119E10 $\mathrm{cm^{-2}}$	No
ρ_{CG}	1.38235E11 $\mathrm{cm^{-2}}$	1.38235E11 $\mathrm{cm^{-2}}$	No
$\rho_{\mathrm{PO_4X}}$	1.51193E11 $\mathrm{cm^{-2}}$	1.51193E11 $\mathrm{cm^{-2}}$	No
ρ_0	9.43E10 $\mathrm{cm^{-2}}$	9.43E10 $\mathrm{cm^{-2}}$	No
D_B	34.2 Å	34.8 Å	Derived
D_C	11.8 Å	12.0 Å	Derived
V_L	1033.65 $\mathrm{Å^3}$	1033.65 $\mathrm{Å^3}$	No
V_C	714.645 $\mathrm{Å^3}$	714.645 $\mathrm{Å^3}$	No
V_{HL}	319 $\mathrm{Å^3}$	319 $\mathrm{Å^3}$	No
$V_{\mathrm{CH_2}}$	25.6329 $\mathrm{Å^3}$	25.6329 $\mathrm{Å^3}$	Yes
r32	1.94	1.94	No
r12	0.29	0.29	No
V_{CG}	153 $\mathrm{Å^3}$	153 $\mathrm{Å^3}$	No
V_{PO4X}	166 $\mathrm{Å^3}$	166 $\mathrm{Å^3}$	No
n{CH2}	24	24	No
n{CH3}	2	2	No
M_{lipid}	677 g/mol	677 g/mol	No
d_{lipid}	1.1 $\mathrm{g/cm^3}$	1.1 $\mathrm{g/cm^3}$	No
σ_{SD}(Polydisperisty)	0.22	0.25	Yes

Table 11: Fitting parameter from model fit to DMPC-DMPG liposomes at 37 °C

Parameter	**Values**	**Fitted?**
Concentration	1.4 mg/ml	Yes
Background	1E-4	No
R	249 Å	Yes
area	60.4 Å	Yes
$z_{\mathrm{CH_3}}$	0	No
$z_{\mathrm{CH_2,\ outer}}$	12.3 Å	Yes
$z_{\mathrm{CH_2,\ inner}}$	-12.3 Å	Yes
$z_{\mathrm{CG,\ outer}}$	15.5 Å	Derived
$\delta_{z_{\mathrm{CG,\ outer}}}$	3.2 Å	Yes
$z_{\mathrm{CG,\ inner}}$	-13.8 Å	Derived
$\delta_{z_{\mathrm{CG,\ inner}}}$	1.5 Å	Yes
$z_{\mathrm{PO_4X}}$	19.9.0 Å	Derived
$\delta_{z_{\mathrm{PO_4X,\ outer}}}$	4.4 Å	Yes
$z_{\mathrm{PO_4X,\ inner}}$	-18.2 Å	Derived
$\delta_{z_{\mathrm{PO_4X,\ inner}}}$	4.4 Å	Yes
$\sigma_{\mathrm{CH_3}}$	2.2 Å	No
$\sigma_{\mathrm{CH_2,\ outer}}$	4.8 Å	Yes
$\sigma_{\mathrm{CH_2,\ inner}}$	4.8 Å	Yes
$\sigma_{\mathrm{CG,\ outer}}$	2.3 Å	Yes
$\sigma_{\mathrm{CG,\ inner}}$	2.3 Å	Yes
$\sigma_{\mathrm{PO_4X,\ outer}}$	3.8 Å	Yes
$\sigma_{\mathrm{PO_4X,\ inner}}$	3.8 Å	Yes
ρ_{CH3}	5.11204E10 $\mathrm{cm^{-2}}$	No
ρ_{CH2}	8.81543E10 $\mathrm{cm^{-2}}$	No
ρ_{CG}	1.38235E11 $\mathrm{cm^{-2}}$	No
ρ_{PO4X}	1.51193E11 $\mathrm{cm^{-2}}$	No
ρ_0	9.43E10 $\mathrm{cm^{-2}}$	No
D_B	36.9 Å	Derived
D_C	11.8 Å	Derived
$V_{\mathrm{CH_2}}$	25.59 $\mathrm{Å^3}$	Yes
M_{PEO}	2000g/ml	No
f_{PEO}	0.025	No
f_{inner}	0.5	Yes
R_g	15	Yes
d_{disp}	-11.8 Å	Yes
σ_{SD}(Polydisperisty)	0.3	Yes

Table 12: Obtained fit parameter from model fit to PEGylated DMPC-DMPG liposomes at 37 °C

6.5 Calculation of the distance between the tethered PEO-chains

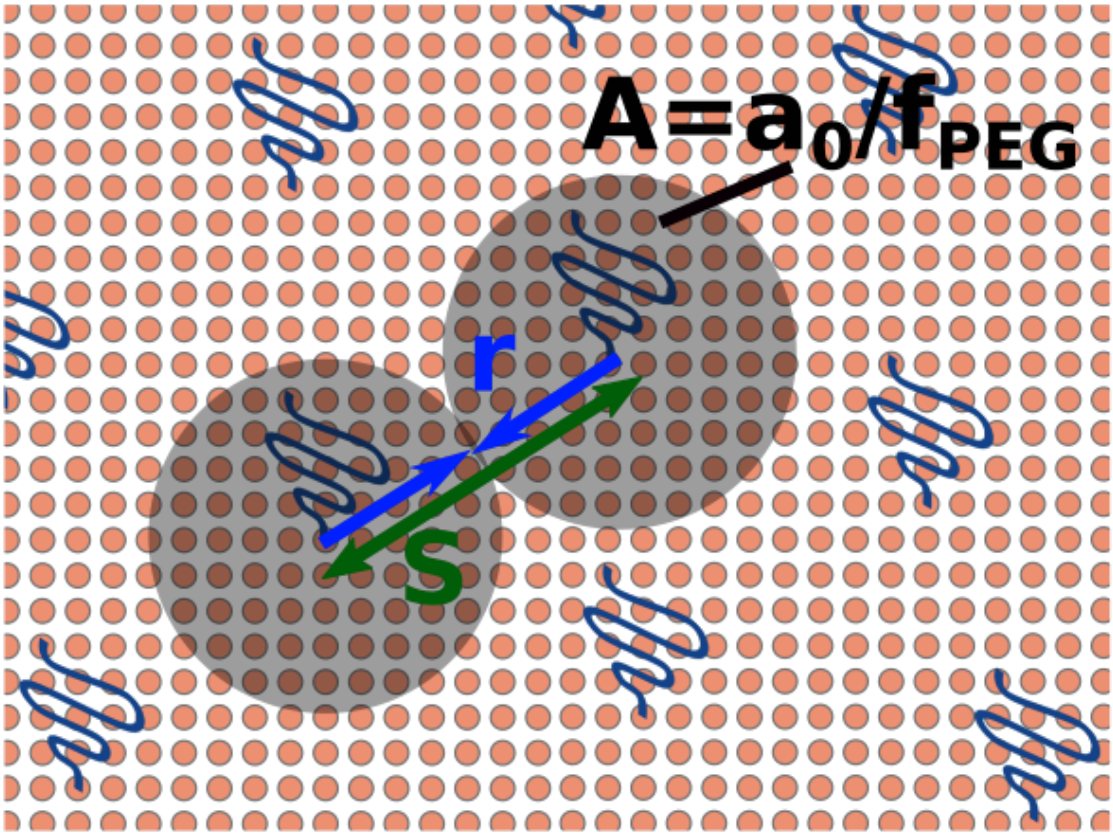

Figure 62: An illustration of the argument for calculation of the spacing between surface-grafted polymer chains.

The estimation of the inter-chain distances of the PEO-chains on the liposomes from their fraction was derived using the following arguments and illustrated in Figure. The number of lipids per PEO-chain is equal to $1/f_{PEO}$. Approximating with the flat surface, the area of this number of lipids is $a_0 \times (1/f_{PEO})$, where a_0 is the lateral area of each lipid. The distance s between the chains if they were evenly spread out would then be twice the radius of the circle of this area ($A = \pi r^2$), giving us equation 89:

$$s = 2\sqrt{\frac{a_0}{\pi \times f_P EO}} \tag{89}$$

which is taken as the average distance. The argument is illustrated in Figure 62

6.6 Addition of Indolicidin - list of relevant model parameters

Parameter	Values 1:5 ratio	Values 1:10 ratio	Values 1:20 ratio	Values 1:50 ratio	Values 1:100 ratio	Fitted?
Concentration	2.5 mg/ml	2.2 mg/ml	1.8 mg/ml	1.7 mg/ml	1.6 mg/ml	Yes
R	>400 Å	>400 Å	267 Å	265 Å	261 Å	Yes
Area	66.1 Å	65.6 Å	63.6 Å	62.5 Å	60.5 Å	Yes
$z_{\mathrm{CH_3}}$	0	0	0	0	0	No
$z_{\mathrm{CH_2,\ outer}}$	12.3	12.3 Å	12.3 Å	12.3 Å	12.3 Å	Yes
$z_{\mathrm{CH_2,\ inner}}$	-12.3	-12.3 Å	-12.3 Å	-12.3 Å	-12.3 Å	Yes
$z_{\mathrm{CG,\ outer}}$	15.5 Å	15.5 Å	15.5 Å	15.5 Å	15.5 Å	Yes
$z_{\mathrm{CG,\ inner}}$	-13.8 Å	-13.8 Å	-13.8 Å	-13.8 Å	-13.8 Å	Yes
$z_{\mathrm{PO_4Xouter}}$	19.9 Å	19.9 Å	19.9 Å	19.9 Å	19.9 Å	Yes
$z_{\mathrm{PO_4X,\ inner}}$	-18.2 Å	-18.2 Å	-18.2 Å	-18.2 Å	-18.2 Å	Yes
$\sigma_{\mathrm{CH_3}}$	2.23 Å	2.23 Å	2.23 Å	2.23 Å	2.23 Å	No
$\sigma_{\mathrm{CH_2,\ outer}}$	4.8 Å	4.8 Å	4.8 Å	4.8 Å	4.8 Å	Yes
$\sigma_{\mathrm{CH_2,\ inner}}$	4.8 Å	4.8 Å	4.8 Å	4.8 Å	4.8 Å	Yes
$\sigma_{\mathrm{CG,\ outer}}$	2.3 Å	2.3 Å	2.3 Å	2.3 Å	2.3 Å	Yes
$\sigma_{\mathrm{CG,\ inner}}$	2.3 Å	2.3 Å	2.3 Å	2.3 Å	2.3 Å	Yes
$\sigma_{\mathrm{PO_4X,\ outer}}$	3.8 Å	3.8 Å	3.8 Å	3.8 Å	3.8 Å	Yes
$\sigma_{\mathrm{PO_4X,\ inner}}$	3.8 Å	3.8 Å	3.8 Å	3.8 Å	3.8 Å	Yes
D_B	40.4 Å	40.2 Å	38.3 Å	36.9 Å	37.4 Å	Derived
D_C	10.7 Å	10.8 Å	11.2 Å	11.4 Å	11.7 Å	Derived
$V_{\mathrm{CH_2}}$	25.4 Å^3	25.4 Å^3	25.4 Å^3	25.4 Å^3	25.4 Å^3	Yes
f_{PEO}	0.025	0.025 Å	0.025 Å	0.025 Å	0.025 Å	Yes
f_{inner}	0.5	0.5	0.5	0.5	0.5	Yes
R_g (for PEO)	15 Å	15 Å	15 Å	15 Å	15 Å	No
d_{disp}	-12.0 Å	-12.0 Å	-12.0 Å	-12.0 Å	-12.0 Å	Yes
f_b	0.17	0.09	0.05	0.02	0.01	Yes
σ_p	3.0 Å	3.0 Å	3.0 Å	3.0 Å	3.0 Å	Yes
z_p	10.1 Å	9.7 Å	9.2 Å	9.2 Å	8.1 Å	Yes
σ_{SD} (Polydispersity)	0.35	0.35	0.31	0.34	0.29	Yes

Table 13: Obtained fit parameters of PEGylated DMPC-DMPG liposomes with different ratios peptide:lipid.

6.7 Estimation of error in measurements and fits

The error in the achieved fit parameters of the small angle scattering model were estimated by testing how much the relevant parameter could be varied without dropping the goodness of fit (R^2) by more than 10%. For co-dependent variables, one of the variables were manually shifted to obtain this maximum error and a new fit was attempted for the dependent variable. If a good fit was not obtained, the manually adjusted value was again shifted towards the original value, and the procedure was continued until a good fit was again obtained. The difference in the value obtained for the dependent variable in this fit from the value in the original fit was then taken as the error for this parameter. The error should therefore be taken in the last significant digit of the given fit values.

For the error in the CMC-values, the relative experimental error was calculated from the absolute error of 0.1 mg/ml in the weight and the weighted amount of m as

$$\sigma_r = \frac{0.1\text{mg}}{m\text{mg}} \times CMC \tag{97}$$

This was then added on to the fit error estimated as described above to give the final relative error given in the Figures and Table.

For the dynamic light scattering measurements, 3 replicates were taken for each measurements. The standard deviation of these were found to be much greater than any error that arises from the fits themselves, so the error was taken from the deviations of the replicates alone.

6.8 Determination of the critical micellar concentration of C_{12}-PEO

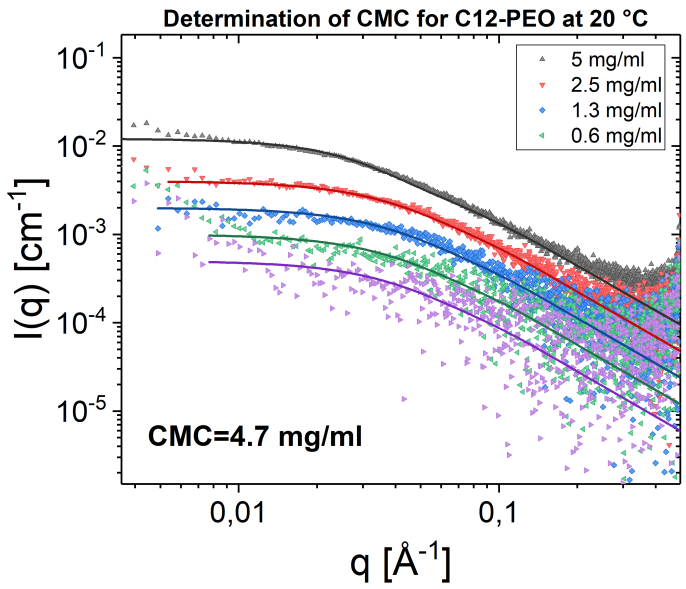

Figure 63: The scattering curves from different concentrations of C_{12}-PEO at 20 °C with fits for the determination of the critical micellar concentration (CMC) using the model described in Section 2.6.1.

The CMC of C_{12}-PEO was determined by SAXS measurements and fitting the model in Section 2.6.1. As Figure 63 shows the highest measured concentration is only 0.3 mg/ml above the CMC determined by the fit. This makes the other parameters fitted in the model unreliable since they are based on fitting to data from very little micelle scattering, and they are therefore not included in this appendix. The CMC should even by visual inspection lie somewhere right below 5 mg/ml, and so the fitted value of 4.7 mg/ml seems reasonable.

6.9 Effect of C_{12}-PEO on the transition temperature of liposomes

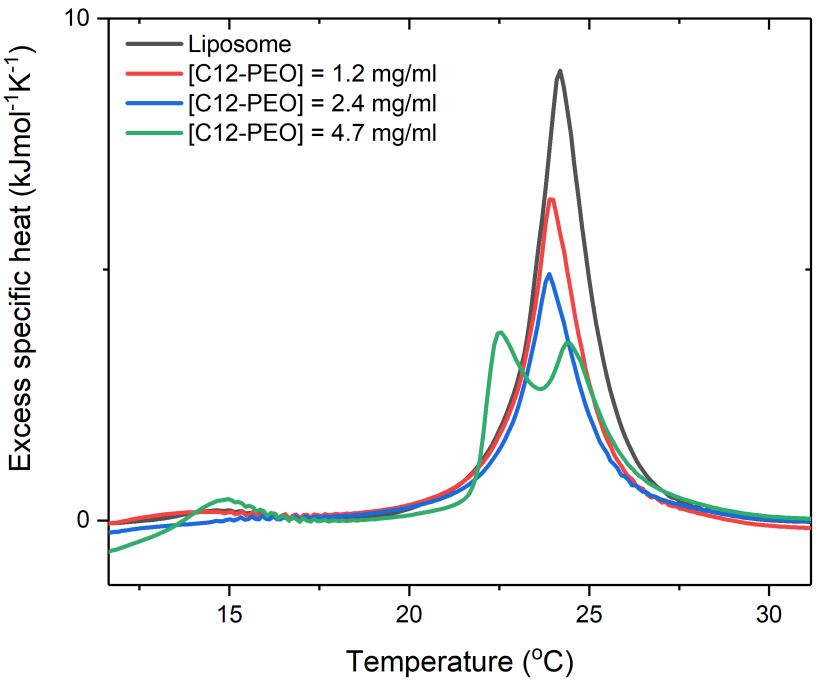

Figure 64: Calorimetric measurements of liposomes with different amounts of C_{12}-PEO added; two concentrations below and one approximately at the CMC determined in Section 6.8, compared with the pure liposome measurement. The bimodality of the main transition peak of the liposome observed for the C_{14}-PEO is also apparent at the CMC of C_{12}-PEO.

Figure 64 shows the calorimetric measurements of DMPC-DMPG liposomes mixed with C_{12}-PEO. Similarly to the DSC measurments of the mixture with C_{14}-PEO (Figure 34, Section 4.3.1), a bimodal peak is observed at the CMC of C_{12}-PEO, suggesting that the C_{12}-PEO has the same mode of action as that of C_{14}-PEO described in Section 4.3.1.

6.10 Water transport across DPPC-DPPG liposomes

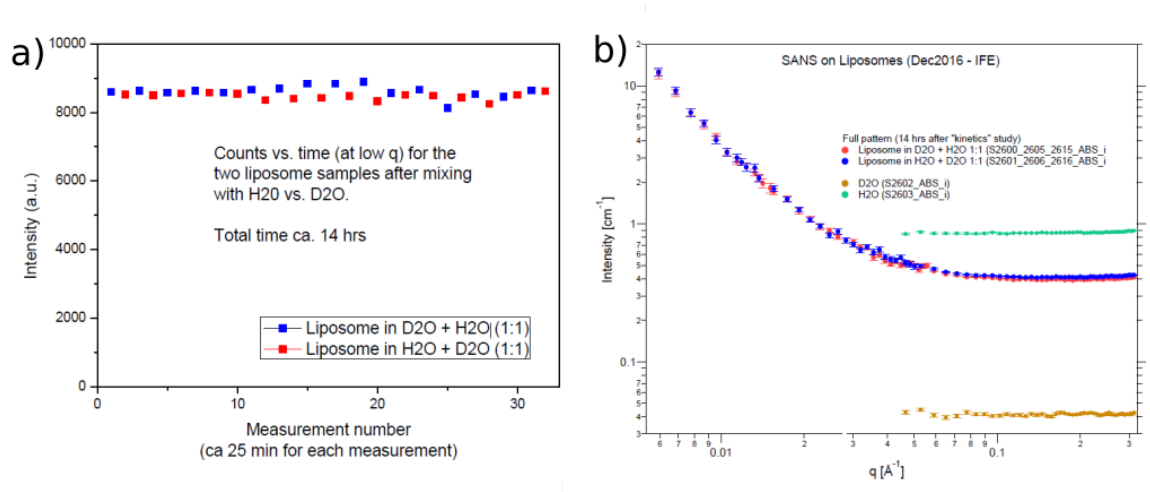

Figure 65: a) shows a comparison of the complete detected intensity of time for the sample prepared in D_2O mixed with H_2O and the sample prepared H_2O mixed with D_2O. There is no systematic difference in scattered intensity over time, suggesting that the water transport occurred before the 20 min of the first measurement. b) shows the full scattering pattern of the two samples as well as the D_2O and H_2O references collected after 14 h. The two sample measurements overlap completely.

Two liposomes batches consisting of 90 % 1,2-dipalmitoyl-sn-glycero-3-phosphocholine (DPPC) and 10 % 1,2-dipalmitoyl-sn-glycero-3-phospho-(1'-rac-glycerol) (DPPG) were prepared according to the protocol in Section 3.1 in D_2O and H_2O respectively. The same experiment as described in Section 4.5 was performed at Institute for Energy Technology (IFE, Kjeller) by doctor Kenneth D. Knudsen. The results showed no difference between the two samples, nor any change of the individual samples over time (Figure 65), so the liposomes exchanged water faster than what could be observed on the timescale of the experiment. Together with the results in Section 4.5 this suggests that the length of the hydrocarbon chain does not affect the water transport to any great extent.

7 Bibliography

[1]S. B. Levy, *The antibiotic paradox* (Springer US, 1992), pp. XIV, 279.

[2]I. GIDEON Informatics and D. S. Berger, *Gideon guide to antimicrobial agents: 2018 edition* (GIDEON Informatics Inc, 27. jan. 2018), p. 993.

[3]H. Jenssen, P. Hamill, and R. E. Hancock, "Peptide antimicrobial agents", Clinical Microbiology Reviews **19**, 491–511 (2006).

[4]C. D. Fjell, J. A. Hiss, R. E. Hancock, and G. Schneider, "Designing antimicrobial peptides: form follows function", Nature Reviews Drug Discovery **11**, 37–51 (2011).

[5]M. Zasloff, "Antimicrobial peptides of multicellular organisms", Nature **415**, 389 (2002).

[6]F. D. Lowy, "Antimicrobial resistance: the example of *Staphylococcus aureus*", Journal of Clinical Investigation **111**, 1265–1273 (2003).

[7]L. T. Nguyen, E. F. Haney, and H. J. Vogel, "The expanding scope of antimicrobial peptide structures and their modes of action", Trends in Biotechnology **29**, 464–472 (2011).

[8]E. J. Prenner, R. N. A. H. Lewis, K. C. Neuman, S. M. Gruner, L. H. Kondejewski, R. S. Hodges, and R. N. McElhaney, "Nonlamellar phases induced by the interaction of Gramicidin S with lipid bilayers. a possible relationship to membrane-disrupting activity", Biochemistry **36**, 7906–7916 (1997).

[9]F. Heitz, F. Kaddari, N. Van Mau, J. Verducci, H. Raniri Seheno, and R. Lazaro, "Ionic pores formed by cyclic peptides", Biochimie **71**, 71–76 (1989).

[10]K. Matsuzaki, "Magainins as paradigm for the mode of action of pore forming polypeptides", Biochimica et Biophysica Acta **1376**, 391–400 (1998).

[11]S. J. Ludtke, K. He, W. T. Heller, T. A. Harroun, L. Yang, and H. W. Huang, "Membrane pores induced by magainin", Biochemistry **35**, 13723–13728 (1996).

[12]Y. Shai and Z. Oren, "From "carpet" mechanism to de-novo designed diastereomeric cell-selective antimicrobial peptides", Peptides **22**, 1629–41 (2001).

[13]B. Bechinger, "Rationalizing the membrane interactions of cationic amphipathic antimicrobial peptides by their molecular shape", Current Opinion in Colloid & Interface Science **14**, 349–355 (2009).

[14]R. F. Epand, W. L. Maloy, A. Ramamoorthy, and R. M. Epand, "Probing the "charge cluster mechanism" in amphipathic helical cationic antimicrobial peptides", Biochemistry **49**, 4076–4084 (2010).

[15]R. M. Epand and R. F. Epand, "Lipid domains in bacterial membranes and the action of antimicrobial agents", Biochimica et Biophysica Acta - Biomembranes **1788**, 289–94 (2009).

[16]R. M. Epand and H. J. Vogel, "Diversity of antimicrobial peptides and their mechanisms of action", Biochimica et Biophysica Acta - Biomembranes **1462**, 11–28 (1999).

[17]W. C. Wimley and K. Hristova, "Antimicrobial peptides: successes, challenges and unanswered questions", The Journal of Membrane Biology **239**, 27–34 (2011).

[18]N. Kucerka, J. F. Nagle, S. E. Feller, and P. Balgavy, "Models to analyze small-angle neutron scattering from unilamellar lipid vesicles", Physical Review E **69**, 051903 (2004).

[19]G. Pabst, N. Kučerka, M. P. Nieh, M. C. Rheinstädter, and J. Katsaras, "Applications of neutron and X-ray scattering to the study of biologically relevant model membranes", Chemistry and Physics of Lipids **163**, 460–479 (2010).

[20]M. A. Kiselev, P. Lesieur, A. M. Kisselev, D. Lombardo, and V. L. Aksenov, "Model of separated form factors for unilamellar vesicles", Applied Physics A **74**, s1654–s1656 (2002).

[21]N. Kučerka, Y. Liu, N. Chu, H. I. Petrache, S. Tristram-Nagle, and J. F. Nagle, "Structure of fully hydrated fluid phase DMPC and DLPC lipid bilayers using X-ray scattering from oriented multilamellar arrays and from unilamellar vesicles", Biophysical Journal **88**, 2626–2637 (2005).

[22]B. Eicher, F. A. Heberle, D. Marquardt, G. N. Rechberger, J. Katsaras, and G. Pabst, "Joint small-angle X-ray and neutron scattering data analysis of asymmetric lipid vesicles", Journal of Applied Crystallography **50**, 419–429 (2017).

[23]G. van Meer, D. R. Voelker, and G. W. Feigenson, "Membrane lipids: where they are and how they behave", Nature reviews Molecular cell biology **9**, 112–124 (2008).

[24]N. Papo and Y. Shai, "Can we predict biological activity of antimicrobial peptides from their interactions with model phospholipid membranes?", Peptides **24**, 1693–1703 (2003).

[25]W. Dowhan, "A retrospective: use of *Escherichia coli* as a vehicle to study phospholipid synthesis and function", Biochimica et Biophysica Acta **1831**, 471–494 (2013).

[26]S. M. Moghimi, P. Symonds, J. C. Murray, A. C. Hunter, G. Debska, and A. Szewczyk, "A two-stage poly(ethylenimine)-mediated cytotoxicity: implications for gene transfer/therapy", Molecular Therapy **11**, 990–995 (2005).

[27]M. L. Immordino, F. Dosio, and L. Cattel, "Stealth liposomes: review of the basic science, rationale, and clinical applications, existing and potential", International Journal of Nanomedicine **1**, 297–315 (2006).

[28]C. Allen, N. Dos Santos, R. Gallagher, G. Chiu, Y. Shu, W. Li, S. Johnstone, A. Janoff, L. Mayer, M. Webb, and M. Bally, "Controlling the physical behavior and biological performance of liposome formulations through use of surface grafted poly(ethylene glycol)", Bioscience Reports **22**, 225–250 (2002).

[29]T. M. Allen, C. Hansen, F. Martin, C. Redemann, and A. Yau-Young, "Liposomes containing synthetic lipid derivatives of poly(ethylene glycol) show prolonged circulation half-lives *in vivo*", Biochimica et Biophysica Acta - Biomembranes **1066**, 29–36 (1991).

[30]W. Zhao, T. Róg, A. A. Gurtovenko, I. Vattulainen, and M. Karttunen, "Role of phosphatidylglycerols in the stability of bacterial membranes", Biochimie **90**, 930–938 (2008).

[31]M. E. Selsted, M. J. Novotny, W. L. Morris, Y. Q. Tang, W. Smith, and J. S. Cullor, "Indolicidin, a novel bactericidal tridecapeptide amide from neutrophils", Journal of Biological Chemistry **267**, 4292–5 (1992).

[32]V. V. Andrushchenko, H. J. Vogel, and E. J. Prenner, "Solvent-dependent structure of two tryptophan-rich antimicrobial peptides and their analogs studied by FTIR and CD spectroscopy", Biochimica et Biophysica Acta - Biomembranes **1758**, 1596–1608 (2006).

[33]T. J. Falla, D. N. Karunaratne, and R. E. Hancock, "Mode of action of the antimicrobial peptide indolicidin", Journal of Biological Chemistry **271**, 19298–303 (1996).

[34]J. N. Israelachvili, “Special interactions: hydrogen-bonding and hydrophobic and hydrophilic interactions”, in *Intermolecular and surface forces (third edition)* (Academic Press, San Diego, 2011), pp. 151–167.

[35]J. N. Israelachvili, “Soft and biological structures”, in *Intermolecular and surface forces (third edition)* (Academic Press, San Diego, 2011), pp. 535–576.

[36]J. N. Israelachvili, D. J. Mitchell, and B. W. Ninham, “Theory of self-assembly of hydrocarbon amphiphiles into micelles and bilayers”, Journal of the Chemical Society, Faraday Transactions 2: Molecular and Chemical Physics **72**, 1525–1568 (1976).

[37]T. Engel and P. Reid, “Ideal and real solutions”, in *Physical chemistry* (Pearson Benjamin Cummings, 2006), p. 193.

[38]J. N. Israelachvili, “Thermodynamic principles of self-assembly”, in *Intermolecular and surface forces (third edition)* (Academic Press, San Diego, 2011), pp. 503–534.

[39]P. Mukerjee and K. J. Mysels, *Critical micelle concentrations of aqueous surfactant systems*, Report (National Standard reference data system, 1971).

[40]D. D. Lasic, “Novel applications of liposomes”, Trends in Biotechnology **16**, 307–21 (1998).

[41]A. Sharma and U. S. Sharma, “Liposomes in drug delivery: progress and limitations”, International Journal of Pharmaceutics **154**, 123–140 (1997).

[42]B. Alberts, A. Johnson, J. Lewis, M. Raff, and P. W. K. Roberts, “Chapter 9: visualizing cells”, in *Molecular biology of the cell*, 5th edition (Garland Science, New York, 2008).

[43]D. D. Lasic, “The mechanism of vesicle formation”, Biochemical Journal **256**, 1–11 (1988).

[44]A. D. Bangham and R. W. Horne, “Negative staining of phospholipids and their structural modification by surface-active agents as observed in the electron microscope”, Journal of Molecular Biology **8**, 660–IN10 (1964).

[45]D. D. Lasic, “On the thermodynamic stability of liposomes”, Journal of Colloid and Interface Science **140**, 302–304 (1990).

[46]J. F. Nagle, “Theory of the main lipid bilayer phase transition”, Annual Review of Physical Chemistry **31**, 157–196 (1980).

[47]R. N. McElhaney, “The biological significance of alterations in the fatty acid composition of microbial membrane lipids in response to changes in environmental temperature”, in *Extreme environments: mechanisms of microbial adaptation*, edited by M. R. Heinrich (Academic Press, New York, 1976), pp. 255–281.

[48]D. L. Melchior and J. M. Steim, “Thermotropic transitions in biomembranes”, Annual Review of Biophysics and Bioengineering **5**, 205–38 (1976).

[49]R. N. McElhaney, “The use of differential scanning calorimetry and differential thermal analysis in studies of model and biological membranes”, Chemistry and Physics of Lipids **30**, 229–59 (1982).

[50]T. Heimburg, “A model for the lipid pretransition: coupling of ripple formation with the chain-melting transition”, Biophysical Journal **78**, 1154–65 (2000).

[51]R. Koynova and B. Tenchov, “Phase transitions and phase behavior of lipids”, in *Encyclopedia of biophysics*, edited by G. C. K. Roberts (Springer Berlin Heidelberg, Berlin, Heidelberg, 2013), pp. 1841–1854.

[52]R. Lund, L. Willner, and D. Richter, "Kinetics of block copolymer micelles studied by small-angle scattering methods", in *Controlled polymerization and polymeric structures: flow microreactor polymerization, micelles kinetics, polypeptide ordering, light emitting nanostructures*, edited by A. Abe, K.-S. Lee, L. Leibler, and S. Kobayashi (Springer International Publishing, Cham, 2013), pp. 51–158.

[53]J. N. Israelachvili, "Interactions of biological membranes and structures", in *Intermolecular and surface forces (third edition)* (Academic Press, San Diego, 2011), pp. 577–616.

[54]D. Lasic, "Sterically stabilized vesicles", Angewandte Chemie International Edition in English **33**, 1685–1698 (1994).

[55]J. Sabin, G. Prieto, J. M. Ruso, R. Hidalgo-Alvarez, and F. Sarmiento, "Size and stability of liposomes: a possible role of hydration and osmotic forces", European Physical Journal E **20**, 401–8 (2006).

[56]R. Rajagopalan and P. C. Hiemenz, *Principles of colloid and surface chemistry, third edition, revised and expanded* (Marcel Dekker, Inc., 1997).

[57]R. Evans and D. H. Napper, "Steric stabilization I", Kolloid-Zeitschrift und Zeitschrift für Polymere **251**, 409–414 (1973).

[58]R. Evans and D. H. Napper, "Steric stabilization II", Kolloid-Zeitschrift und Zeitschrift für Polymere **251**, 329–336 (1973).

[59]J. N. Israelachvili, "Steric (polymer-mediated) and thermal fluctuation forces", in *Intermolecular and surface forces (third edition)* (Academic Press, San Diego, 2011), pp. 381–413.

[60]R. Bhat, M. Tomlinson, T. Wu, and J. Genzer, "Surface-grafted polymer gradients: formation, characterization, and applications", in *Surface-initiated polymerization ii.* Vol. 198, edited by R. Jordan, Advances in Polymer Science. (Springer, Berlin, Heidelberg, 1970), pp. 51–124.

[61]A. Halperin, M. Tirrell, and T. P. Lodge, "Tethered chains in polymer microstructures", in *Macromolecules: synthesis, order and advanced properties* (Springer, Berlin, Heidelberg, 1992), pp. 31–71.

[62]S. Alexander, "Polymer adsorption on small spheres. a scaling approach", Journal de Physique **38**, 977–981 (1977).

[63]J. Als-Nielsen, *Elements of modern X-ray physics*, 2nd ed. (Wiley, Chichester, 2011).

[64]T. Brückel, G. Heger, D. Richter, G. Roth, and R. Zorn, *Neutron scattering: lectures of the JCNS laboratory course held at Forschungszentrum Jülich and at the Heinz Maier-Leibnitz Zentrum Garching. in cooperation with RWTH Aachen and University of Münster.* (Forschungszentrum Jülich, 2017).

[65]T. Zemb and P. Lindner, *Neutron, X-rays and light. Scattering methods applied to soft condensed matter.* (North Holland, 2002).

[66]D. Sivia, *Elementary scattering theory: for X-ray and neutron users* (OUP Oxford, 2011).

[67]B. Willis and C. Carlile, *Experimental neutron scattering* (OUP Oxford, 2009).

[68]H. Brumberger, *Modern aspects of small-angle scattering*, Nato Science Series C (Springer Netherlands, 1995), pp. XV, 463.

[69]D. Svergun, M. Koch, P. Timmins, and R. May, *Small angle X-Ray and neutron scattering from solutions of biological macromolecules* (OUP Oxford, 2013).

[70]A. Guinier, *Small-angle scattering of X-rays*, Structure of matter series (Wiley, New York, 1955).

[71]J. S. Pedersen, "Analysis of small-angle scattering data from colloids and polymer solutions: modeling and least-squares fitting", Advances in Colloid and Interface Science **70**, 171–210 (1997).

[72]J. S. Pedersen, "Small-angle scattering from surfactants and block copolymer micelles", in *Soft matter characterization*, edited by R. Borsali and R. Pecora (Springer Netherlands, Dordrecht, 2008), pp. 191–233.

[73]J. S. Pedersen, C. Svaneborg, K. Almdal, I. W. Hamley, and R. N. Young, "A small-angle neutron and X-ray contrast variation scattering study of the structure of block copolymer micelles: corona shape and excluded volume interactions", Macromolecules **36**, 416–433 (2003).

[74]M. Daoud and J. Cotton, "Star shaped polymers: a model for the conformation and its concentration dependence", Journal de Physique **43**, 531–538 (1982).

[75]R. Lund, V. Pipich, L. Willner, A. Radulescu, J. Colmenero, and D. Richter, "Structural and thermodynamic aspects of the cylinder-to-sphere transition in amphiphilic diblock copolymer micelles", Soft Matter **7**, 1491–1500 (2011).

[76]C. Svaneborg and J. S. Pedersen, "Block copolymer micelle coronas as quasi-two-dimensional dilute or semidilute polymer solutions", Physical Review E **64**, 010802 (2001).

[77]G. Beaucage, "Small-angle scattering from polymeric mass fractals of arbitrary mass-fractal dimension", Journal of Applied Crystallography **29**, 134–146 (1996).

[78]T. Zinn, "Molecular exchange kinetics and structure of n-alkyl-PEO polymeric micelles studied by SANS", Thesis (2013).

[79]N. Kučerka, J. F. Nagle, J. N. Sachs, S. E. Feller, J. Pencer, A. Jackson, and J. Katsaras, "Lipid bilayer structure determined by the simultaneous analysis of neutron and X-ray scattering data", Biophysical Journal **95**, 2356–2367 (2008).

[80]D. Marquardt, F. A. Heberle, J. D. Nickels, G. Pabst, and J. Katsaras, "On scattered waves and lipid domains: detecting membrane rafts with X-rays and neutrons", Soft Matter **11**, 9055–9072 (2015).

[81]N. Kučerka, J. Pencer, J. N. Sachs, J. F. Nagle, and J. Katsaras, "Curvature effect on the structure of phospholipid bilayers", Langmuir **23**, 1292–1299 (2007).

[82]J. Pencer, S. Krueger, P. Adams Carl, and J. Katsaras, "Method of separated form factors for polydisperse vesicles", Journal of Applied Crystallography **39**, 293–303 (2006).

[83]L. Arleth and C. Vermehren, "An analytical model for the small-angle scattering of polyethylene glycol-modified liposomes", Journal of Applied Crystallography **43**, 1084–1091 (2010).

[84]W. I. Goldburg, "Dynamic light scattering", American Journal of Physics **67**, 1152 (1999).

[85]A. Einstein, "Zur theorie der brownschen bewegung", Annalen der Physik **324**, 371–381 (1906).

[86]A. J. F. Siegert, *On the fluctuations in signals returned by many independently moving scatterers* (Radiation Laboratory, Massachusetts Institute of Technology, Cambridge, Mass., 1943).

[87]J. Stetefeld, S. A. McKenna, and T. R. Patel, "Dynamic light scattering: a practical guide and applications in biomedical sciences", Biophysical Reviews **8**, 409–427 (2016).

[88]Avanti polar lipids, Inc., *Liposome preparation.* Retrieved 21. April 2018 from https://avantilipids.com/tech-support/liposome-preparation/, Web Page.

[89]AntonPaar, *Viscosity of water.* Retrieved 26. April, 2018 from https://wiki.anton-paar.com/en/water/, Web Page.

[90]R. N. A. H. Lewis and R. N. McElhaney, "Differential scanning calorimetry (DSC), pressure perturbation calorimetry (PPC), and isothermal titration calorimetry (ITC) of lipid bilayers", in *Encyclopedia of biophysics*, edited by G. C. K. Roberts (Springer Berlin Heidelberg, Berlin, Heidelberg, 2013), pp. 452–459.

[91]TAinstruments, *Microcalorimetry: ITS & DSC.* Retrieved 19. April 2018 from http://www.tainstruments.com/wp-content/uploads/broch-micro-en.pdf, Web Page.

[92]*BM29 experimental hutch.* Retrived 6. April 2018 from http://www.esrf.eu/home/usersandscience/experiments/mx/about˙our˙beamlines/bm29/beamline-setup/beam-delivery.html, Web Page.

[93]P. Pernot, A. Round, R. Barrett, A. De Maria Antolinos, A. Gobbo, E. Gordon, J. Huet, J. Kieffer, M. Lentini, M. Mattenet, C. Morawe, C. Mueller-Dieckmann, S. Ohlsson, W. Schmid, J. Surr, P. Theveneau, L. Zerrad, and S. McSweeney, "Upgraded ESRF BM29 beamline for SAXS on macromolecules in solution", Journal of Synchrotron Radiation **20**, 660–664 (2013).

[94]F. Lixin, D. Mike, B. Scott, G. Nick, and I. Jan, "The absolute calibration of a small-angle scattering instrument with a laboratory X-ray source", Journal of Physics: Conference Series **247**, 012005 (2010).

[95]V. Pipich, "Qtikws: user-friendly program for reduction, visualization, analysis and fit of SA(N)S data", http://www.qtikws.de (2012).

[96]S. Singer and S. Singer, "Efficient implementation of the Nelder–Mead search algorithm", Applied Numerical Analysis & Computational Mathematics **1**, 524–534 (2004).

[97]H. M.-L. Z. e. al., "Kws-3: very small angle scattering diffractometer with focusing mirror.", Journal of large-scale research facilities **1** (2015).

[98]J. F. Nagle and S. Tristram-Nagle, "Structure of lipid bilayers", Biochim Biophys Acta **1469**, 159–95 (2000).

[99]N. Kučerka, M.-P. Nieh, and J. Katsaras, "Fluid phase lipid areas and bilayer thicknesses of commonly used phosphatidylcholines as a function of temperature", Biochimica et Biophysica Acta - Biomembranes **1808**, 2761–2771 (2011).

[100]J. Pan, F. A. Heberle, S. Tristram-Nagle, M. Szymanski, M. Koepfinger, J. Katsaras, and N. Kučerka, "Molecular structures of fluid phase phosphatidylglycerol bilayers as determined by small angle neutron and X-ray scattering", Biochimica et Biophysica Acta - Biomembranes **1818**, 2135–2148 (2012).

[101]T. Zinn, L. Willner, R. Lund, V. Pipich, M.-S. Appavou, and D. Richter, "Surfactant or block copolymer micelles? Structural properties of a series of well-defined n-alkyl-PEO micelles in water studied by SANS", Soft Matter **10**, 5212–5220 (2014).

[102]T. Zinn, L. Willner, K. D. Knudsen, and R. Lund, "Self-assembly of mixtures of telechelic and monofunctional amphiphilic polymers in water: from clusters to flowerlike micelles", Macromolecules **50**, 7321–7332 (2017).

[103]J. M. Sturtevant, "A scanning calorimetric study of small molecule-lipid bilayer mixtures", Proceedings of the National Academy of Sciences of the United States of America **79**, 3963–7 (1982).

[104]W. Haynes, *CRC handbook of chemistry and physics, 93rd edition* (CRC Press, 2016).

[105]T. M. Bayerl, T. Köchy, and S. Brückner, "On the modulation of a high-enthalpy pretransition in binary mixtures of DMPC and DMPG by polar headgroup interaction", Biophysical Journal **57**, 675–680 (1990).

[106]J. S. Pedersen and M. C. Gerstenberg, "Scattering form factor of block copolymer micelles", Macromolecules **29**, 1363–1365 (1996).

[107]J. S. Pedersen, I. W. Hamley, C. Y. Ryu, and T. P. Lodge, "Contrast variation small-angle neutron scattering study of the structure of block copolymer micelles in a slightly selective solvent at semidilute concentrations", Macromolecules **33**, 542–550 (2000).

[108]J. Nielsen, V. Bjørnestad, and R. Lund, "Resolving the interactions between antimicrobial peptides and lipid membranes using small-angle scattering methods: the case of indolicidin", Unpublished manuscript (2018).

[109]R. P. Brent, "An algorithm with guaranteed convergence for finding a zero of a function", The Computer Journal **14**, 422–425 (1971).

[110]*One dimensional root-finding*. Retrieved 20. April 2018 from https://www.gnu.org/software/gsl/doc/html/roots.html, Web Page.

[111]J. M. Rausch, J. R. Marks, R. Rathinakumar, and W. C. Wimley, "B-sheet pore-forming peptides selected from a rational combinatorial library: mechanism of pore formation in lipid vesicles and activity in biological membranes", Biochemistry **46**, 12124–12139 (2007).

[112]C. Neale, J. C. Hsu, C. M. Yip, and R. Pomès, "Indolicidin binding induces thinning of a lipid bilayer", Biophysical Journal **106**, L29–L31 (2014).

[113]W. C. Wimley, "Describing the mechanism of antimicrobial peptide action with the interfacial activity model", ACS Chemical Biology **5**, 905–917 (2010).

[114]M. N. Melo and M. A. R. B. Castanho, "The mechanism of action of antimicrobial peptides: lipid vesicles vs. bacteria", Frontiers in Immunology **3**, 236 (2012).

[115]A. Cass and A. Finkelstein, "Water permeability of thin lipid membranes", The Journal of General Physiology **50**, 1765–1784 (1967).

[116]J. Lemmich, K. Mortensen, J. H. Ipsen, T. Hønger, R. Bauer, and O. G. Mouritsen, "The effect of cholesterol in small amounts on lipid-bilayer softness in the region of the main phase transition", European Biophysics Journal **25**, 293–304 (1997).

[117]T. Róg, M. Pasenkiewicz-Gierula, I. Vattulainen, and M. Karttunen, "Ordering effects of cholesterol and its analogues", Biochimica et Biophysica Acta - Biomembranes **1788**, 97–121 (2009).

[118]M. Bloom, E. Evans, and O. G. Mouritsen, "Physical properties of the fluid lipid-bilayer component of cell membranes: a perspective", Quarterly Reviews of Biophysics **24**, 293–397 (1991).

[119]A. Finkelstein and A. Cass, "Effect of cholesterol on the water permeability of thin lipid membranes", Nature **216**, 717 (1967).